UPC　　　　**CTTC**

Simulation of heat and mass transfer phenomena in the critical elements of H$_2$O-LiBr absorption cooling machines. Experimental validation and application to design.

Centre Tecnològic de Transferència de Calor
Departament de Màquines i Motors Tèrmics
Universitat Politècnica de Catalunya
Jesús Castro Gonzàlez

Doctoral Thesis

Simulation of heat and mass transfer phenomena in the critical elements of H$_2$O-LiBr absorption cooling machines. Experimental validation and application to design.

Jesús Castro Gonzàlez

TESI DOCTORAL

presentada al

Departament de Màquines i Motors Tèrmics
E.T.S.E.I.T.
Universitat Politècnica de Catalunya

per a l'obtenció del grau de

Doctor Enginyer Industrial

Terrassa, April 2005

Simulation of heat and mass transfer phenomena in the critical elements of H_2O-LiBr absorption cooling machines. Experimental validation and application to design.

Jesús Castro Gonzàlez

Directors de la Tesi

Dr. Assensi Oliva Llena

Dr. Carlos David Pérez Segarra

Tribunal Qualificador

Dr. Valeriano Ruiz Hernández
Universidad de Sevilla

Dr. José Manuel Pinazo Ojer
Universidad Politécnica de Valencia

Dr. Manuel Vázquez Vázquez
Universidad de Vigo

Dr. Antonio Lecuona Neumann
Universidad Carlos III de Madrid

Dr. Joaquim Rigola Serrano
Universitat Politècnica de Catalunya

Contents

Acknowledgements

Gràcies als meus pares, Mª Dolores i Juvencio per la seva estimació i comprensió incondicionals. En tot moment heu respectat les meves decisions relatives a la meva trajectòria professional, tot i les dificultats que sempre hem tingut.

Agraeixo també als meus germans, Santiago i Alejandro per aquests anys de convivència junts en els que han sigut també els meus amics.

Gràcies a en Carles Oliet per la seva amistat que tant m'ha ajudat en els moments més difícils. Les xerrades que hem mantigut, m'han estimulat sempre a fer millores personals i professionals.

Vull fer també especial esment a en Manolo. Sense les seves idees, el seu entusiasme i la seva implicació, els muntatges experimentals d'aquesta tesi no s'haguèssin pogut dur a terme.

Gràcies a en Marcos per la seva ajuda abnegada en els tasques més desagraïdes en el treball experimental.

Gràcies també a en Ramiro Alba per la seva ajuda que ha anat més enllà de la estrictament professional.

Vull agrair també a en Manel Soria per les seves observacions sobre aquest treball.

Vull fer també un agraïment a en Joaquim Rigola per les seves observacions i comentaris constructius amb els que he pogut pul·lir molts detalls d'aquesta tesi.

Gràcies a en Carles David Pèrez, per la seva ajuda en la finalització d'aquesta tesi. Amb els seus comentaris, m'ha ajudat a millorar en molts aspectes aquest treball. És un autèntic luxe i privilegi poder treballar amb ell.

Gràcies finalment a en Assensi Oliva, pel seu consell i orientació, que m'ha permés sempre treure el millor de mi mateix i arribar on mai hagués cregut. Sense ell probablement mai hagués treballat en aquests temes i probablement mai hagués conegut un Grup humanament tant bo i tant competent com és el Centre Tecnològic de Transferència de Calor.

Gràcies a tots ja que sense vosaltres això no haguès estat possible.

Abstract

Due to the increasing trend of the price of the energy, mainly obtained from fossil combustibles, and its also increasing use for air-conditioning in developed countries, solar cooling has been becoming more attractive from the point of view of economics and environment conservation. The final aim of this thesis is the development of numerical simulation tools for the design of absorption machines with the possibility of being driven by solar energy. Although there are available in the market absorption chillers of such characteristics for years, there is a lack in development of small capacity systems. Small capacity systems imply additional problems of design (air-cooled systems, compactness ...) that only can be afford with adequate design tools for system and components. Moreover, there is also a lack in the specialised literature in the development of adequate mathematical models for the description of the heat and mass transfer processes in absorption machines: wetted area of the heat and mass transfer surfaces, role of additives, complex geometries etc.

For these reasons this work has been focused on the following detailed objectives:

- Study of basic heat and mass transfer processes together with the fluid-dynamic phenomena implied in absorbers of absorption chillers. This study has been carried out by means of detailed simulations solving the Navier-Stokes equations under certain hypotheses.

- Development of numerical simulation tools for design and prediction of absorption systems, taking advantage of information given by more detailed models.

- Development of numerical simulation tools for design of the heat and mass exchange components of absorption systems keeping the calculation in a reasonable CPU time. This model provides of the necessary information for the model mentioned in the previous point.

- Development of a prototype of an air-cooled absorption machine based on the numerical results obtained from the models.

- Validation of the models developed by means of comparison of numerical results and experimental data obtained from the prototypes developed.

- Study of the performance of the above mentioned absorption system.

- Evaluation of the results in order to improve the design criteria for a second generation of prototypes.

After the development of these numerical simulation tools and their application in specific problems, a framework has been created for the study of other type of absorption systems.

Chapter 1

Introduction

Abstract. In this first chapter a general overview of the work carried out is presented. After a brief description of the structure of this thesis, the technological objectives are briefly situated in the context of heat powered cooling systems. The basic principle of absorption technology is explained, and the most used absorption fluids (H_2O-LiBr and NH_3-H_2O) are compared according to their thermodynamic properties. An overview of the current absorption technology state of the art is also shown, where some research projects are also referred. Next part of the chapter explains the need of a prototype development for a small capacity air-cooled, hot water driven absorption cooling machine according to the market context (object of design in this work in the context of a European funded project [1]). Some antecedents of related works are also mentioned. The prototype developed is briefly introduced. Finally, an introduction of absorption chillers design models is also explained.

1.1   Structure of this thesis

This thesis is structured in several chapters as thematic units. Each point of the following relation gives a general overview of each chapter:

1. Introduction to heat powered cooling techniques, with special emphasis to absorption technology. In the last part, the prototype developed in this work is referred together with the models used in its design.

2. Description of the models usually used to study the phenomena involved in absorption machines, specifically the partial differential equations systems to be solved, the calculation hypotheses applied and the boundary conditions at the liquid-vapour interface considered, where absorption and desorption processes are produced.

3. Explanation of the numerical implementation of the different models used.

4. Presentation of some results of detailed simulations of absorption processes with and without additives. These results have been object of publication [2].

5. Comparison between some experimental results obtained from two small-sized, air-cooled absorber prototypes with the numerical ones of the model implemented for designing this element.

6. Presentation of the whole air-cooled absorption machine. Design criteria have also been described. Procedure of starting up.

7. Experimental results obtained from the whole absorption chiller and comparisons with simulations of the whole system and each element. These results have been also submitted to publication.

8. Summary of the conclusions of all the results reported in the previous chapters. Future actions are also described in the different research lines opened during the development of this work.

1.2   Heat powered cooling systems

A cooling system is an inverse thermal machine that uses mechanical work to extract heat from a cold medium and reject it to a warmer one, according to the limitations of the Thermodynamic laws. If the available energy is heat instead of mechanical work, a direct thermal machine can be used to transform it into mechanical work, and then this work can be used for cooling production. The two thermal machines (inverse and direct) working together in an integrated device are a heat powered cooling system.

There are many direct techniques for cooling production from a heat source. Each one could be more suitable in different applications according to the working conditions, size of installation, etc. The following techniques are the most studied [**?**]:

- Absorption. It is the most used technique. The mechanical compressor of the typical vapour compression systems is substituted by a thermochemical compressor, a whole of heat exchangers: absorber, generator and solution heat exchanger (Fig. 1.1). In this case, the refrigerant is "absorbed" by an absorbent substance normally in liquid phase. Therefore, the substance compressed is a liquid (absorbent-refrigerant solution). Consequently the mechanical work required is much lower. This thesis is focused on the absorption refrigeration. More details of its performance are given in the next section.
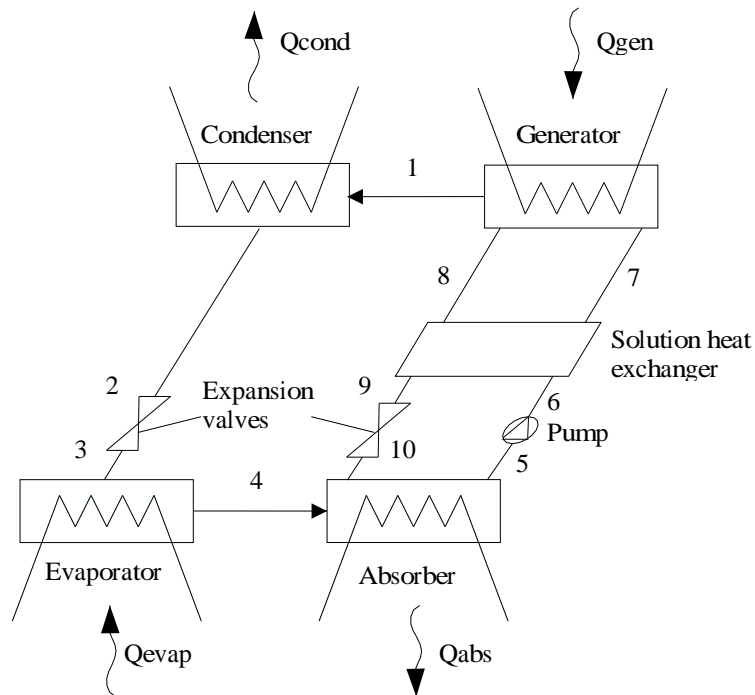
Figure 1.1: Single cycle absorption machine

- Dessicant cooling. This technique is based on pre-drying the air that will be introduced in the room to be conditioned by means of a dessicant substance.

After this operation, this air is humidified and the air temperature decreases by evaporative cooling. Therefore, the air is conditioned in temperature and humidity. The dessicant substance is "regenerated" (the excess of humidity is removed) by a thermal heat source (see Fig. 1.2).
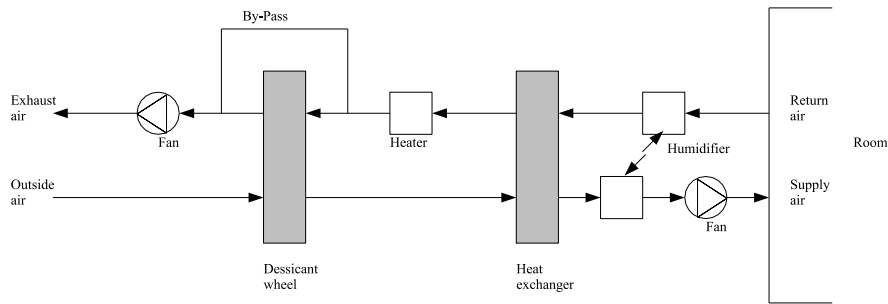
Figure 1.2: Dessicant cooling system

- Adsorption. The basic operation is quite similar to the absorption technique. The main difference is that the substance capable of "assimilate" the refrigerant is not a liquid solution that changes its physical properties, it is a substance that "assimilates" the refrigerant in a superficial process, without changing its physical properties. Normally, this substance is in solid state, therefore it is not possible to circulate it in a continuous way and, consequently, the cooling effect is performed in a intermittent cycle (see Fig. 1.3). In regeneration mode, gate V1 and the expansion valve are closed, and the reactor-adsorber (where the adsorbent substance is placed) is "regenerated": the refrigerant is evaporated because the reactor is heated by the hot source and then is condensed in the condenser. Finally, the condensed refrigerant is stored in a reservoir. In cooling mode, the pressure goes down because the reactor-adsorber works in adsorption mode (it is now continuously cooled). While gate V2 is closed, the gate V1 and the expansion valve are opened. At that moment the refrigerant is evaporated at low temperature and pressure and its vapour adsorbed in the reactor until its saturation. When the saturation is achieved, the regeneration mode starts again.

- Rankine cycle. Basically is a combination of a vapour power cycle where the mechanical work produced in the turbine is used in a compressor of a vapour compression cycle (Fig. 1.4).

- Ejector cooling (Fig. 1.5). This cycle combines the action of two ejectors (device
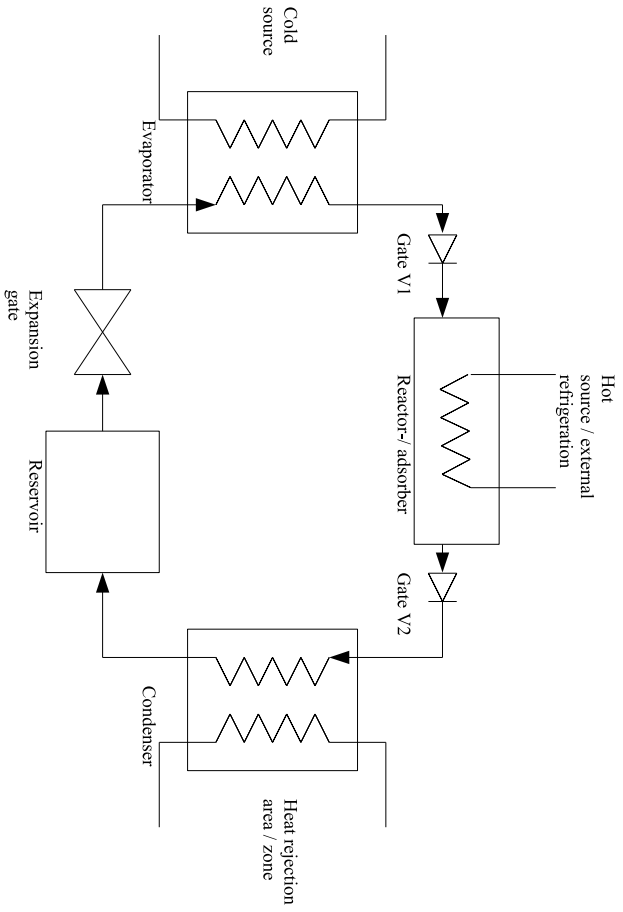
Figure 1.3: Basic adsorption cooling cycle
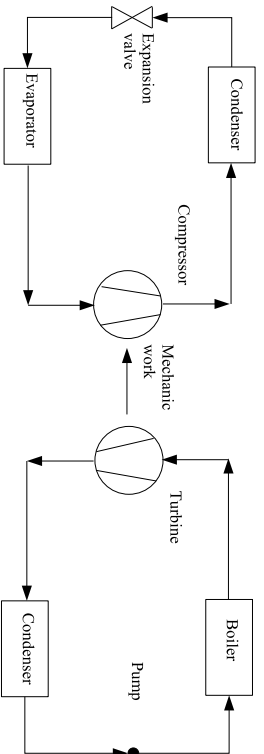
Figure 1.4: Rankine cycle
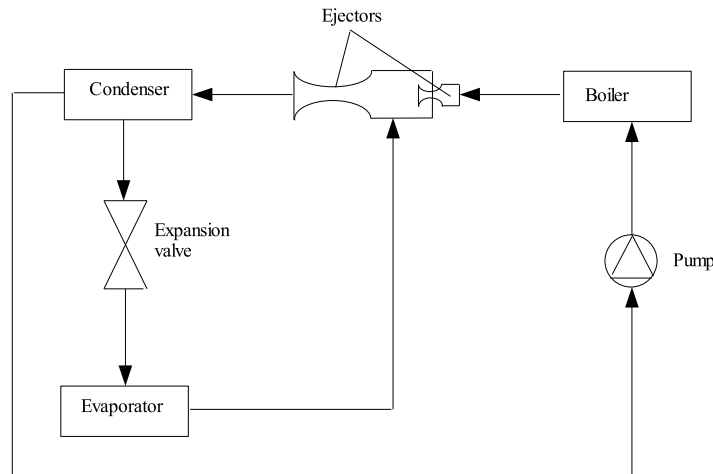
Figure 1.5: Ejector cooling cycle

where the kinetic energy of a fluid is transformed in pressure energy) that perform in serial operation: a small ejector expands the vapour of refrigerant that comes from a boiler; this expanded vapour goes to the second ejector that converts the kinetic energy of the vapour in pressure energy. After this operation, some of the refrigerant goes to the cooling cycle (condenser, expansion valve and evaporator) and the rest returns to the boiler. The two streams are remixed in the second ejector.

1.3   Introduction to absorption refrigeration

The most widely system used in refrigeration technology is based on vapour compression.   These systems need mechanical energy normally provided by an electrical drive.   However, electrical energy is not always available or it is too expensive, or there is available thermal energy that can be used for cooling purposes. In these situations, a heat powered system, such as absorption refrigeration, could be an interesting alternative. Thermal energy is normally cheaper than the electrical one and in some situations could be for free, e.g. waste heat or solar energy.

Moreover, there are other additional reasons to develop absorption refrigeration systems. On the one hand, the use of technologies capable of using renewable energies is very interesting due to the increasing demand of fossil combustibles that contribute

to increase the "greenhouse effect". On the other hand, further development of refrigeration systems that use natural refrigerants, like water or ammonia that does not affect the ozone layer and does not also increase the "greenhouse effect" is also very interesting. These two refrigerants are most widely used in absorption systems.

1.3.1 Brief approach to the history of absorption technology

Absorption in one of the earliest methods used for refrigeration [3]. The scientific fundamentals of absorption refrigeration were already proposed by Faraday in 1823. The first patent of absorption refrigeration was developed by Ferdinand Carre in 1850. It was an intermittent cycle. Some years later, the first machine of continuum cycle was built by Mignon and Rouard in 1862. That machine used ammonia-water as working fluid.

In the beginning of the refrigeration technology, absorption refrigeration was the most widely used due to its capacity of using low quality energy (e.g. waste heat of industrial processes), but at the end of the XIXth century vapour compression systems substituted the absorption systems due to their better performance.

Nowadays, there is an renewed interest in the development of absorption systems in Europe, due to the energy policy of decreasing the dependence of non-renewable energies in order to achieve Kyoto's protocol objectives of CO$_2$ emissions reduction [4].

1.3.2 Physical principle

The absorption principle is based on the difference of the liquid-vapour equilibrium conditions between a substance (refrigerant) in pure state and the same substance dissolved with another one (absorbent). At the same temperature, when the refrigerant is pure, its equilibrium pressure is higher than when it is mixed with the absorbent. At constant pressure, the equilibrium temperature of the pure refrigerant is lower than when it is dissolved with the absorbent substance. In order to fulfill these conditions, the absorbent substance has to be less volatile than the refrigerant.

For a better understanding of the basic principle, a description of an open cycle absorption machine performance (see Fig. 1.6) in the pressure / temperature diagram of a well-known refrigerant-absorbent pair, H$_2$O-LiBr (Fig. 1.7), is presented. In this diagram the equilibrium conditions for the pure water and for the H$_2$O-LiBr solution in different weight concentrations are depicted.

Container 1 is filled with a solution of refrigerant (R) and absorbent (A), and container 2 is filled with pure refrigerant. An important hypothesis is to consider that the concentration of absorbent in the container 1 remains almost constant. Under these conditions, when valve between them is closed and the two containers are at the same temperature. Therefore, the vapour pressure in container 2, point 2 of the
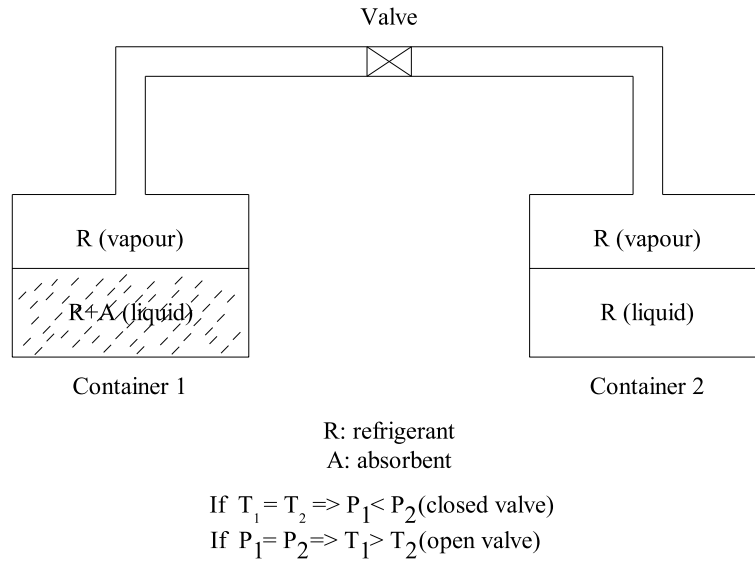
Figure 1.6: Open cycle absorption machine

diagram, is higher than in container 1, point 1" of the diagram ($T_{1''} = T_2$ and $P_{1''} < P_2$). When the valve is opened, the vapour of refrigerant goes from container 2 to container 1, due to pressure difference. The vapour pressure in container 1 exceeds the equilibrium pressure and the vapour is absorbed by the refrigerant-absorbent solution. Due to heat of absorption, the temperature in container 1 increases (point 1' of the diagram). The inverse process occurs in container 2, where the temperature decreases due to the heat of evaporation (point 2' of the diagram). Finally, the vapour pressure is the same in the two containers, as a result of the mass transfer between them ($P_{1'} = P_{2'}$ and $T_{1'} > T_{2'}$).

   If heat is introduced into container 2, a new equilibrium pressure will be reached. The vapour pressure in container 2 will exceed the equilibrium pressure of container 1 and a new mass transport will be generated from container 2 to 1. In such way, the heat is "pumped" from the place of lower temperature to the place of higher temperature. The absorption process could be used for refrigeration, when the container takes heat from the surroundings or for heating purposes, when the heat produced in the warmer container is used for heating the surroundings. This is the principle of the open cycle absorption machine, where, in the absorption mode, the mass transport goes from container 2 to 1 and the refrigeration is produced. In
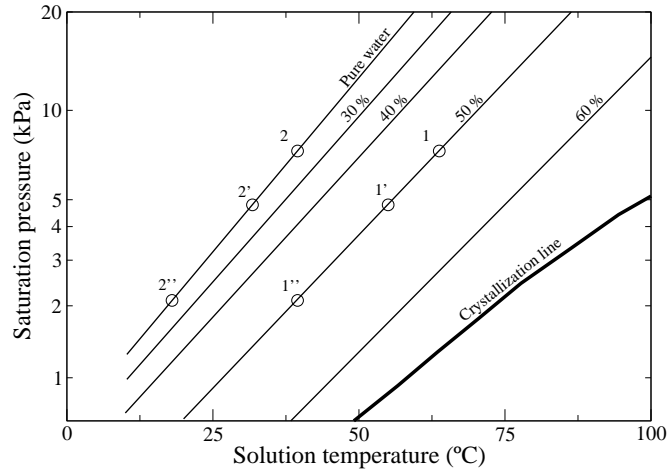
Figure 1.7: Open cycle absorption / desorption processes in the pressure / temperature diagram

regeneration mode, the process is inverse: heat is introduced in container 1, therefore the vapour of refrigerant goes to container 2 because the valve is opened. In the container 2 the refrigerant is condensed (heat must be removed). Then, the valve is closed and the initial conditions are reestablished.

1.3.3 Single effect cycle

In a closed cycle, the refrigeration effect is produced in a continuous way (see Fig. 1.1). The single effect cycle is composed by five heat exchangers (generator, absorber, solution heat exchanger, condenser and evaporator), a pump and two expansion valves. Starting in the generator, the heat introduced warms the refrigerant-absorbent solution. When the solution enters to the generator, it is rich in refrigerant (poor in absorbent), but due to the heat introduced, part of the refrigerant evaporates (1) and its concentration in the solution decreases. The vapour of refrigerant produced condenses in the condenser, then the condensed liquid (2) is expanded in the expansion valve (3) and finally, the liquid-vapour mixture totally evaporates in the evaporator (4). After evaporating part of the refrigerant, the solution leaves the generator (8) and

it is precooled in the solution heat exchanger (9). Then, it is expanded (10) and enters in the absorber. The vapour of refrigerant is absorbed in the absorber by solution rich in absorbent (poor in refrigerant). When the solution leaves the absorber, it has high concentration in refrigerant (5), it is preheated in the solution heat exchanger and reaches again the generator (7). In the solution loop the pressure difference is achieved by means of a pump, that needs much less electrical power than a vapour compressor. This basic closed cycle is called also single effect cycle, because the heat introduced in the absorption system is used once to produce refrigerant vapour.

There are more complicated cycle configurations generally focused on taking advantage of high temperature heat sources (double effect cycles) or for achieving lower evaporator temperatures than the ones achieved in a single effect cycle. Alefeld and Radermacher [**?**] give a description of many advanced cycle configurations suitable for such situations. The description of these configurations is not the objective of this work because our research has been focused on absorption systems which are adequate to be used with low temperature heat sources (e.g. solar energy).

1.4 H_2O-LiBr and NH_3-H_2O as working fluids

The basic conditions for the choice of a pair refrigerant-absorbent are: i) total miscibility at absorber conditions of pressure and temperature and, ii) total unmiscibility at generator conditions. The pressure conditions both the absorber and generator are fixed by the mass transfer balance with the evaporator and condenser, respectively. The temperature at the absorber is fixed by the cooling medium (air or water), and by the heat source in the generator. Moreover, the refrigerant has to be much more volatile than absorbent, therefore the boiling points have to be separated.

There are many refrigerant-absorbent pairs that fulfill these conditions in useful applications. However, only two fluid pairs have been widely used in the market: H_2O-LiBr and NH_3-H_2O. These two fluid pairs have their advantages and disadvantages, but their use is complementary. Other options with other working fluids have been discarded for many different reasons, such corrosion, chemical stability at high temperatures, etc.

The working fluid NH_3-H_2O allows its application in a wide range of conditions. It can be used for air-conditioning, refrigeration [5], etc. However, H_2O-LiBr machines have a higher efficiency and lower driving temperatures than NH_3-H_2O machines, therefore H_2O-LiBr systems are more adequate for solar assisted air-conditioning systems. There are machines with single- effect configuration commercially available. Their use fits adequately for air conditioning applications. As a subfamily, there are hot water driven single-effect water-LiBr absorption chillers on the market. All these machines are water-cooled. However, the use of H_2O as refrigerant is not possible to reach evaporation temperatures under 0 °C, because of the triple point of this

substance. For these cases (lower evaporation temperature), the use of NH_3 is clearly preferred.

1.5 State of the art

Absorption cooling equipment has been available for decades on an industrial scale. Most commercial equipment is directly gas-fired. However, hot water and steam driven equipment are also available.

According to our knowledge, the two types of commercial available machines that uses H_2O-LiBr as working fluid are (all of them water-cooled):

- Single-effect cycle machines. They can be gas-fired or hot water driven, COP about 0.7-0.8, manufacturers: Trane, Carrier, York, Sanyo, LG, Entropie, Mitshubishi, Hitachi, Toshiba, etc.

- Double effect cycle machines. Gas-fired or steam driven, COP about 1.0-1.2, manufacturers: Trane, Carrier, York, Sanyo, LG, Broad, Mitshubishi, Hitachi, Toshiba, etc.

On the other hand, NH_3-H_2O machines are available on the market with the following cycle configurations:

- Single effect cycles. Typical one stage cycle, with relatively low performance, COP about 0.6-0.7, manufacturers: Robur, Colibri-Stork, Hans Güntner Gmbh AbsorptionKälte KG, etc.

- Cycles with internal heat exchange between components (e.g. generator and absorber, GAX-cycle), COP about 0.7-1.0, manufacturers: Colibri-Stork, etc.

This relation of suppliers does not pretend to be exhaustive and complete. However, most of the more important manufacturer or suppliers have been reported.

Currently, most air-cooled absorption machines on the market use the fluid pair NH_3-H_2O. Robur commercialises an absorption chiller with these characteristics with a COP near 0.7. The minimum cooling capacity offered is 10 kW. However, this machine is gas-fired and therefore needs high driving temperatures in comparison to the typical solar driven systems.

There is also other air-cooled machines (Electrolux, Taver) based on the NH_3-H_2O-H_2 cycle that does not need any pump and both absorber and condenser are cooled by natural convection. Apart from the high driving temperatures needed, these machines give a quite low COP values (about 0.3).

The hot water driven chiller available on the market with the lowest cooling capacity (35 kW) are water cooled single-effect H_2O-LiBr cycle configuration.

Typically, it requires hot water temperature at 88°C and gives a COP about 0.7 [6]. This machine has the particularity that it does not require any internal mechanical pump, therefore it is totally heat powered (bubble pump).

On the other hand, double effect water-LiBr absorption chillers are available driven with steam, with a cooling capacity from 110 kW upwards. In general, small commercial absorption machines have a power range from 70 to 100 kW.

Research and development on H_2O-LiBr systems are focused on the following points: performance improvement, enhancement of heat and mass transfer in the constituent elements in order to reduce the size of the machines, and systems without cooling tower for low capacity units. There are in Europe several efforts in order to develop competitive small capacity units. In a previous European funded project [7] a prototype of a hot water driven, water-LiBr single effect absorption chiller water-cooled suitable for solar cooling installations or waste heat recovery was developed. This machine was tested obtaining a cooling capacity of 10 kW, with a COP of 0.78, and delivering chilled water at 18°C. The hot water input temperature was 95°C and cooling water one was 27°C. Moreover, it has been developed another similar water-cooled chiller [8]. In this case, this machine gave a capacity of 15 kW with a COP of 0.70, delivering chilled water at 15°C. The hot water input temperature was at 90°C and cooling water one at 32°C. Finally, a different concept of machine is presented in [9]. In this case, the mass transfer process at the absorber is enhanced by means of a rotary movement, decreasing the temperature difference between the absorber and the water cooling stream. Under such conditions the machine can perform without cooling tower. Even though the machine is gas-fired, it is projected to design a hot-water driven one.

Air cooling of water-LiBr machines is feasible, although it requires an adequate design in order to avoid crystallization and may increase the costs of the main heat exchangers. There has been research in those air-cooled systems [10, 11, 12, 13, 14], although these cycles were double effect and need high driving temperatures (about 140-160°C). Single effect, hot water driven cycles, have an additional problem that is to achieve the desired temperature lifts. It requires an accurate design of all the elements to take the maximum advantage of the cycle and to achieve a balanced interaction between them.

With regards to ammonia-water systems, research and development is focused on systems with lower input temperature requirements [15] and reduction of the size of the machine by means of the use of compact heat exchangers [16].

1.6 Motivation: low cost, low capacity air-cooled machines

In the last decades a significant increase in electricity consumption has been produced due to the growth in cooling demand. In order to save energy in cooling systems it is necessary to develop new technologies to take advantage of alternative energies e.g. the solar energy or waste heat in order to satisfy the new energy demand.

Absorption cooling is one of the most widely used systems in heat powered cooling installations. In the case of solar cooling installations, the main obstacle that prevents its extended use is the large initial investment necessary for both solar collectors and absorption machine. For low capacity installations (less than 15 kW), the price of the chiller is the most limiting factor. Therefore, it is necessary innovative designs of both solar collectors and absorption chillers [17] to reduce prices. Moreover, a higher simplicity of the absorption cooling installation would reduce the cost of the investment significantly. For this reason, air-cooling for the absorber and condenser to avoid the cooling tower results an important issue for reducing the final price of the installation. Using the pair H_2O-LiBr it is possible to take advantage of a higher performance with respect to NH_3-H_2O system, but the use of LiBr as absorbent implies the risk of crystallisation, more important in air-cooled systems. In those systems the heat transfer coefficients are lower and it is not possible to use the evaporative cooling for the absorber and condenser.

Different prototypes of air-cooled H_2O-LiBr machines have been developed in the past decade [10, 11, 12, 13, 14], for air-conditioning in buildings. However, those machines were gas-fired. Therefore, the type of cycle used in those cases was double effect in order to get the maximum advantage of the input energy. LiBr is used as absorbent together with LiI to overcome the problem of crystallisation in references [10, 12]. The main problem for all those machines relies on the high electrical consumption of the fans to create adequate cooling effect on both the absorber and the condenser, because a reduced and compact design were the main premises. In reference [18], an air-cooled system suitable for being used in public transport, and taking advantage of the waste heat of the engine, is presented.

1.7 Prototype developed

In this thesis, a prototype of a low power absorption cooling machine with air-cooled condenser and absorber has been developed. Its input energy is hot water below 100°C. Therefore a single effect cycle is suitable for this situation (Fig. 1.1). Although the final performance of the system is slightly reduced due to the air-cooling in both the absorber and the condenser the main premise of design has been to keep the electrical fan consumption within these elements in moderate limits maintaining a

reasonable COP. The prototype has a mechanic solution pump, which leads to a different behaviour of the machine with respect to the temperature driven pumps used in the commercial chillers WFC of Yazaki (these chillers experiment a drastic decrease of the COP due to the decrease of the circulated mass flow at low driving temperatures [6, 19, 20]. Different temperature, pressure and mass flow sensors have been located in the most significant points of the machine. This unit has been conceived as an experimental laboratory test device with removable components to facilitate modifications with respect to the initial design.

Due to heat transfer and pressure drop requirements of the H_2O-LiBr absorption cycle, all the heat exchangers are of falling film type (except the solution heat exchanger -SHX- which is standard plate heat exchanger). Falling film heat exchangers have two main advantages: i) the fluid is driven by gravity, not by pressure gradients, i.e. there is no pressure losses, ii) it provides good heat transfer coefficients at low temperature differences.

The machine studied in this thesis must be suitable for using thermal energy below 100 °C (solar energy), therefore the generator and evaporator are made of horizontal tubes, where the falling liquid film goes outside the tubes. Falling film generators are common in single effect water-LiBr machines driven by hot water or steam. They take better advantage of the input energy than pool boiling generators. Concerning to falling film evaporators, they are especially adequate for water-LiBr machines, because the evaporation temperature cannot be too low due to the freezing point of the water. Therefore, it is also interesting to take the maximum advantage of this temperature.

The absorber and condenser are air-cooled, and they consist on batteries of vertical finned tubes, where the falling film goes inside the tubes. Air-cooled falling film condensers are not common in water-LiBr machines (all the commercial are water-cooled). However, its design is not as problematic as air-cooled absorbers, because they deal with higher heat transfer coefficients. In the case of direct air-cooled falling film absorbers, there is moreover very little experience. They have been used in several prototypes in the past decade [10, 11, 12, 13, 14]. These absorbers perform the heat and mass transfer simultaneously, as the water-cooled ones. Moreover, there is a patent [21] of an air-cooled absorber with separate processes of heat and mass transfer. This type of absorber reduces the size of the finned heat exchangers, but needs an adiabatic chamber for doing the mass transfer and a solution pump with higher flow capability than for the one required in a classical absorber configuration.

1.8 Modeling of absorption systems

The development of numerical simulation tools based on adequate mathematical models is a key aspect for an accurate design and prediction of the thermal behaviour

of absorption chillers. Therefore, their price is reduced and the performance of the installation can be optimised.

An absorption chiller is constituted by different heat exchangers working together and under complex geometries and physical phenomena. The complete detailed simulation of the whole system is not feasible due, in part, to the high CPU time required. Thus, it is necessary to develop simplified models in order to obtain the necessary information of different aspects of the system. According to the level of design and the aspects to be studied, each type of simulation plays its proper role. Three levels of modeling have been developed and employed in this thesis:

- Global modeling of the whole absorption chiller cycle. This model is based in overall heat and mass balances between elements complemented with certain calculation hypotheses in order to close the system of equations generated. It is useful at the first stage of design, because it is capable of showing trends in the performance of the system with a reasonable accuracy if the external conditions are changed. This model needs of certain information (e.g. overall heat transfer coefficients) provided by more detailed simulations.

- Detailed modeling of the heat exchangers of the absorption chiller. In a second stage of design, this type of modeling is useful for the optimisation of the size of the elements under the working conditions indicated in the first stage. The values obtained of temperature, pressure, absorbent concentration, and mass flow in the most significant points of the system are used as input values for these more detailed models. In this way, the size of the heat and mass exchange components is determined. It calculates the overall heat transfer coefficients multiplied by the heat transfer area (UA) and other additional information about the conditions of the working fluids in significant points of the system (e.g. subcoolings).

- Detailed modeling of the heat and mass transfer phenomena in absorption processes. This simulation can be used to obtain heat and mass transfer coefficients for the previous type of simulation. It is useful in case there is not empirical information available or the semi-empirical models employed (of reduced CPU consumption) does not describe completely the phenomenology involved.

References

[1] A. Oliva, J. Castro, C. D. Pérez-Segarra, M. Lucena, J. C. Martínez, J. Simonin, G. Brachthäuser, M. J. Arrarás, and J. C. Lavandeira. Craft-Joule Project: Air-Cooled Water LiBr Cooling Machine of Low Capacity for Air Conditioning

(ACABMA). In *Proceedings of the Millenium Solar Forum 2000*, pages 835–841, 2000.

[2] J. Castro, L. Leal, C.D. Pérez-Segarra, and P. Pozo. Numerical study of the enhancement produced in absorption processes using surfactants. *International Journal of Heat and Mass Transfer*, 47(14-16):3463–3476, 2004.

[3] N. K. Bansal, P. K. Bansal, M. S. Sodha, G. N. Tiwari, S. N. Shukla, S. C. Kaushik, and M. A. S. Malik. *Reviews of Renewable Energy Resources*. Sejwal, M. S., 1983.

[4] United Nations. United Nations Framework Convention on Climate Change, 1992.

[5] M. Bogart. *Ammonia Absorption Refrigeration in Industrial Processes*. Gulf Publishing Company, 1981.

[6] Yazaki Ltd. *Manual de instalación de grupos refrigerantes por absorción de agua caliente WFC 10*, 1996.

[7] C. Schweigler, A. Costa, M. Harm, M. Högenauer-Lego, and F. Ziegler. Small Capacity LiBr-Absorption Chiller for Solar Cooling and Waste Heat Utilization. In *Proceedings of the International Sorption Heat Pump Conference*, pages 1–9, 2002.

[8] M. Safarik, L. Richter, C. Heinrich, and M. Otto. Small capacity water/lithium bromide absorption chiller for solar cooling applications. In *Proceedings of the 5th ISES Europe Solar Conference (EUROSUN 2004)*, 2004.

[9] K. Gilchrist, R. Lorton, and R. J. Green. Process Intensification Applied to an Aqueous LiBr Rotating Absorption Chiller with Dry Heat Rejection. *Applied Thermal Engineering*, 22(7):847–854, 2002.

[10] S. Tongu, Y. Makino, K. Ohnishi, and S. Nakatsugawa. Practical operating of small-sized air-cooled double-effect absorption chiller-heater by using Lithium Bromide and aqueous. In *Proceedings of the International Absorption Heat Pump Conference*, pages 125–132, 1993.

[11] T. Ohuchi, M. Aizawa, R. Kawakami, A. Nishiguchi, T. Hatada, and Y. Kunugi. A Study on a Hot-Water Driven Air-Cooled Absorption Refrigerating Machine. In *Proceedings of the 1994 International Refrigeration Engineering Conference at Purdue*, pages 275–280, 1994.

[12] H. Ishino and S. Kawasaki. Development of air-cooled type absorption chiller/heater using a new working fluid (LiBr+LiI/H$_2$O). In *Proceedings of the International Gas Research Conference*, pages 687–698, 1998.

[13] R. Kawakami, N. Nishiyama, M. Aimi, and S. Tongu. Development of small-sized air-cooled absorption air-conditioner. In *Proceedings of the International Gas Research Conference*, pages 699–707, 1998.

[14] K. Enjoji. Development of a direct gas-fired absorption duct-type air-conditioner with an air-cooled absorber and condenser. In *Proceedings of the International Gas Research Conference*, pages 708–718, 1998.

[15] G. Kunze. The principle of the bypass, state of the art, 2003. Workshop: Absorption cooling research and development, Vienna, Austria.

[16] J. Bassols, R. Langreck, B. Schneider, H. Kuckelkorn, and H. Veelken. Absorption Cooling Machine Based on Compact Plate-Fin Heat Exchangers. In *Proceedings of the 19th International Congress of Refrigeration*, pages 240–245, 1995.

[17] F. Ziegler. State of the Art in Sorption Heat Pumping and Cooling Technologies. *International Journal of Refrigeration*, 25(4):450–459, 2002.

[18] M. Izquierdo, M. Aróstegui, and E. Martín. Sistema móvil de refrigeración por absorción de bromuro de litio condensado por aire, Patent nº 2103162, Oficina Española de Patentes y Marcas, 1997.

[19] M. Pfaff, R. Saravanan, M. Prakash Maiya, and S. Srinivasa Murthy. Studies of bubble pump for a water-lithium bromide vapour absorption refrigerator. *International Journal of Refrigeration*, 21(6):452–462, 1998.

[20] R. Saravanan and M. Prakash Maiya. Experimental Analysis of a Bubble Pump Operated H$_2$O-LiBr Vapour Absorption Cooler. *Applied Thermal Engineering*, 23(18):2383–2397, 2003.

[21] M. Izquierdo, E. Martín, A. Lecuona, and P.A. Rodríguez. Absorbedor de gotas iguales de flujos paralelos, Patent nº 2161119, Oficina Española de Patentes y Marcas, 2001.

Jesús Castro Gonzàlez, *Simulation of heat and mass transfer phenomena in the critical elements of H_2O-LiBr absorption cooling machines. Experimental validation and application to design.*, Doctoral Thesis, Universitat Politècnica de Catalunya, April 2005.

Chapter 2

Numerical models used for the design and optimisation of absorption chillers

Abstract. The numerical simulation models implemented for the design and optimisation of absorption chillers are herein described. The modeling is basically divided in three levels, depending on the level of detail: i) whole absorption cycle, ii) heat and mass exchange components, iii) heat and mass transfer processes. The utility of each model is explained, and the different calculation hypotheses for each one are also presented. The first level, used in the study of the absorption cycle, is described by means of the applied equations that constitute a non-linear system. With regards to detailed modeling of the components, two types of heat exchangers are considered, fin and tube (absorber and condenser) and serpentine (generator and evaporator). Therefore, two types of software have been developed. In each case, the empirical information used is indicated, and the semi-empirical model based in the boundary layer hypotheses in the conservation equations for absorption/ desorption processes is described. Finally, the most detailed model, used for a more complete simulation of absorption processes is also described. This model is based on the resolution of the Navier-Stokes equations under certain hypotheses.

2.1   Simulation of the whole absorption system
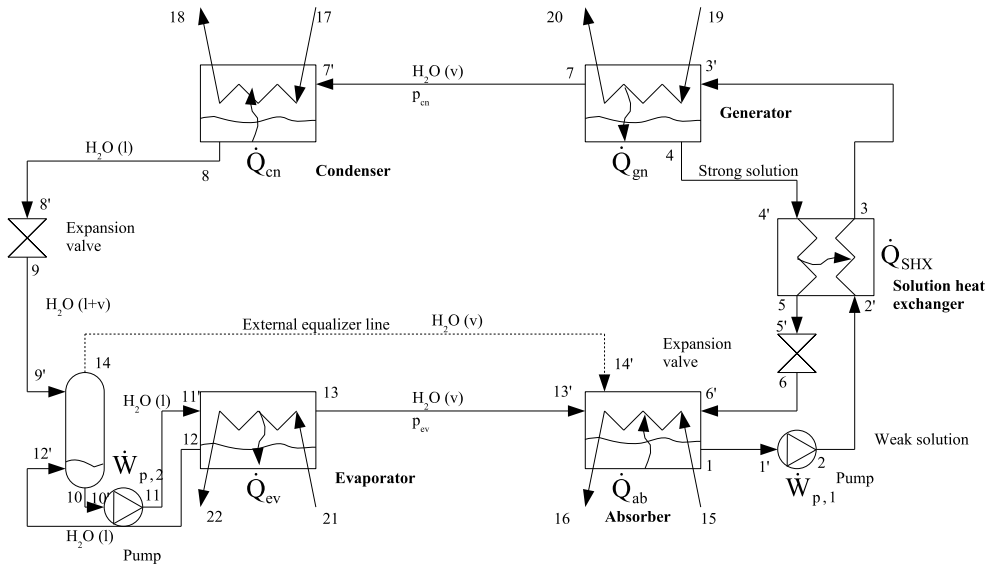
Figure 2.1: Scheme of the installation

In order to study the kind of air-cooled absorption system described in the previous chapter, a mathematical model to simulate the whole system (see Fig. 2.1) has been developed. For each element, overall mass and energy balances are imposed. In design mode, the nominal capacity (heat power removed at the evaporator) and the heat transfer efficiencies of the other heat exchangers are given to obtain the overall heat transfer coefficient multiplied by the area of each heat exchanger (UA), the heat power exchanged in each element, and the main data of the absorption cycle (enthalpies, temperatures, pressures, LiBr mass fractions and mass flows). In rating mode, the area and overall heat transfer coefficients of the heat exchangers are given, while the effectiveness and heat exchanged in each element are obtained in addition to the main data of the absorption cycle. Negligible heat losses and pressure drops in the connections between elements are assumed. These conditions, together with mass conservation, produce for each i-connection: $\dot{m}_i = \dot{m}_{i'}$, $c_i = c_{i'}$, $h_i = h_{i'}$, $p_i = p_{i'}$. Under steady-state conditions, and neglecting both kinetic and potential energy, the equations considered in the analysis are the following:

Absorber:

$$\dot{m}_1 - \dot{m}_{6'} - \dot{m}_{13'} - \dot{m}_{14'} = 0 \tag{2.1}$$

$$\dot{m}_1 c_1 - \dot{m}_{6'} c_{6'} = 0 \tag{2.2}$$

$$\dot{m}_1 h_1 - \dot{m}_{6'} h_{6'} - \dot{m}_{13'} h_{13'} - \dot{m}_{14'} h_{14'} = -\dot{Q}_{ab} \tag{2.3}$$

$$\dot{m}_{15}(h_{16} - h_{15}) = \dot{Q}_{ab} \tag{2.4}$$

$$T_1 = T_{sat,sol}(p_1, c_1) \tag{2.5}$$

$$Q_{ab} = UA_{ab} \frac{(T_{6'} - T_{15}) - (T_1 - T_{16})}{ln \frac{(T_{6'} - T_{15})}{(T_1 - T_{16})}} \tag{2.6}$$

Solution pump (positive displacement pump):

$$c_2 = c_{1'} \tag{2.7}$$

$$\dot{m}_{1'}(h_2 - h_{1'}) = \dot{W}_{p,1} \tag{2.8}$$

$$\dot{m}_{1'} = constant \tag{2.9}$$

Solution heat exchanger:

$$c_3 = c_{2'} \tag{2.10}$$

$$c_5 = c_{4'} \tag{2.11}$$

$$\dot{m}_{2'}(h_3 - h_{2'}) = \dot{Q}_{SHX} \tag{2.12}$$

$$\dot{m}_{4'}(h_5 - h_{4'}) = -\dot{Q}_{SHX} \tag{2.13}$$

$$Q_{SHX} = UA_{SHX} \frac{(T_{2'} - T_5) - (T_3 - T_{4'})}{ln \frac{(T_{2'} - T_5)}{(T_3 - T_{4'})}} \tag{2.14}$$

Generator:

$$\dot{m}_7 + \dot{m}_4 - \dot{m}_{3'} = 0 \tag{2.15}$$

$$\dot{m}_4 c_4 - \dot{m}_{3'} c_{3'} = 0 \tag{2.16}$$

$$\dot{m}_7 h_7 + \dot{m}_4 h_4 - \dot{m}_{3'} h_{3'} = \dot{Q}_{gn} \tag{2.17}$$

$$\dot{m}_{20} h_{20} - \dot{m}_{19'} h_{19'} = -\dot{Q}_{gn} \tag{2.18}$$

$$T_4 = T_{sat,sol}(p_4, c_4) \tag{2.19}$$

$$T_4 = T_7 \tag{2.20}$$

$$Q_{gn} = UA_{gn} \frac{(T_{3'} - T_{20}) - (T_4 - T_{19})}{ln \frac{(T_{3'} - T_{20})}{(T_4 - T_{19})}} \tag{2.21}$$

Solution valve:

$$c_6 = c_{5'} \qquad (2.22)$$

$$h_6 = h_{5'} \qquad (2.23)$$

Condenser:

$$\dot{m}_{7'}(h_8 - h_{7'}) = -\dot{Q}_{cn} \qquad (2.24)$$

$$\dot{m}_{17}(h_{18} - h_{17}) = \dot{Q}_{cn} \qquad (2.25)$$

$$T_8 = T_{sat,w}(p_8) \qquad (2.26)$$

$$Q_{cn} = UA_{cn} \frac{(T_8 - T_{17}) - (T_8 - T_{18})}{ln\frac{(T_8 - T_{17})}{(T_8 - T_{18})}} \qquad (2.27)$$

Refrigerant valve:

$$h_9 = h_{8'} \qquad (2.28)$$

Evaporator:

$$\dot{m}_{13} + \dot{m}_{12} - \dot{m}_{11'} = 0 \qquad (2.29)$$

$$\dot{m}_{13}h_{13} + \dot{m}_{12}h_{12} - \dot{m}_{11'}h_{11'} = \dot{Q}_{ev} \qquad (2.30)$$

$$\dot{m}_{21}(h_{22} - h_{21}) = -\dot{Q}_{ev} \qquad (2.31)$$

$$T_{12} = T_{sat,w}(p_{12}) \qquad (2.32)$$

$$T_{13} = T_{sat,w}(p_{13}) \qquad (2.33)$$

$$Q_{ev} = UA_{ev} \frac{(T_{13} - T_{21}) - (T_{11'} - T_{22})}{ln\frac{(T_{13} - T_{21})}{(T_{11'} - T_{22})}} \qquad (2.34)$$

Vessel:

$$\dot{m}_{10} + \dot{m}_{14} - \dot{m}_{9'} - \dot{m}_{12'} = 0 \qquad (2.35)$$

$$\dot{m}_{10}h_{10} + \dot{m}_{14}h_{14} - \dot{m}_{9'}h_{9'} - \dot{m}_{12'}h_{12'} = 0 \qquad (2.36)$$

Refrigerant pump (positive displacement pump):

$$\dot{m}_{10'}(h_{11} - h_{10'}) = \dot{W}_{p,2} \qquad (2.37)$$

$$\dot{m}_{10'} = constant \qquad (2.38)$$

Other additional hypotheses are assumed in order to close the non linear system of equations generated:

- The degree of subcooling of the solution at the absorber outlet is fixed as a parameter of the cycle (point 1).

- It is assumed equilibrium of the LiBr solution in the generator outlet (point 4).

- The superheated vapour in the generator outlet is at the same temperature as the outlet solution (points 7 and 4).

- Outlet of H_2O at condenser is saturated liquid (point 8).

- Outlet of H_2O from vessel to refrigerant pump as saturated liquid (point 10).

- Outlet of H_2O from evaporator to vessel is saturated liquid (point 12).

- Outlet of H_2O from evaporator to the absorber is saturated vapour (point 13).

- Outlet of H_2O from the vessel to the equalizer line is saturated vapour (point 14).

- Pressure losses are only considered in the expansion valves (points 8'-9 and 5'-6).

- Adiabatic expansion in the valves are conditioned (points 8'-9 and 5'-6).

- Adiabatic pumps are modeled (points 1'-2 and 10'-11).

All the UAs are defined according to $UA = \dot{Q}/LMTD$ where LMTD is the logarithmic mean temperature difference. The UA values are calculated in an accurate way by means of the detailed models presented in next section.

It is assumed that the enthalpy and entropy of compressed liquid (for LiBr solution and pure water) and water vapour only depends on the temperature. The equilibrium relations and functions for enthalpy calculations for the H_2O-LiBr pair have been extracted from ASHRAE [1], and the entropy expressions for the T-s diagrams from Kaita [2]. For the case of pure H_2O, the thermophysical data have been extracted from [3], except the entropy expressions (for T-s diagrams), which has been extracted from NIST [4].

2.2 Simulation of the heat and mass exchange components.

For the design of the air-cooled absorption chiller prototype, numerical detailed codes have been developed to calculate each specific element. These codes are also used for prediction purposes. They are able to simulate the heat and mass transfer processes implied under certain hypotheses or using the appropriate empirical information if necessary. The solution heat exchanger has been calculated using standard methods calculations methodology.

The thermophysical properties of the H_2O-LiBr pair have been extracted from different sources. Density, viscosity and thermal conductivity from [5, **?**], heat capacity from [1], mass diffusivity from [6] and surface tension from [7]. In the case of pure H_2O, the source for the thermophysical properties has been reference [3].

2.2.1 Air-cooled heat exchangers (absorber, condenser): air-side

For the simulation of the air side of the air-cooled elements (absorber and condenser), a code developed for simulating the thermal and fluid dynamic behaviour of fin and tube heat exchangers [8, 9] has been used. This code adopt a strategy of resolution based on discretization of the heat exchanger into macro control volumes around the tubes (see Fig. 2.2). Over these macro volumes, conservation of mass, momentum and energy are applied for the air, and the energy conservation for the solid elements. The inner flow is a specific subroutine, in this case falling film absorption or pure fluid condensation, which provides the necessary boundary conditions for the calculation of the solid elements. In order to keep the CPU time consumption within reasonable limits, the mathematical formulation requires the knowledge of some empirical information e.g. local heat transfer coefficients and local friction factors. This basic empirical information does not depend on a specific heat exchanger but on the kind of heat transfer surfaces and local flow structure (i.e. the code needs a fundamental or elementary empirical information). This information is obtained from the literature (e.g. [10]).

In this modeling a multidimensional simulation of the fins can be performed, and the longitudinal and transversal conduction heat transfer is also calculated. In this way, heat transfer through the solids (tubes and fins) is accurately evaluated, without using approximate fin efficiency. The code integrates for the zones corresponding to the macro control volumes the heat fluxes and tube-fin and fin-air and calculates real fin efficiency for each of the macro control volumes. This model has an advantage in cases where great temperature differences within the fin exist and in cases where conductivity of the fin is directionally dependent. In these cases the hypothesis of adiabatic boundary condition for the calculation of the fin efficiency that is normally used might not be adequate.

2.2.2 Serpentine heat exchangers (generator, evaporator): water side

In the case of the generator and the evaporator, the type of heat exchanger to be solved consists of a serpentine of horizontal tubes wetted by LiBr aqueous solution in the case of the generator, and pure water in the case of the evaporator. The strategy
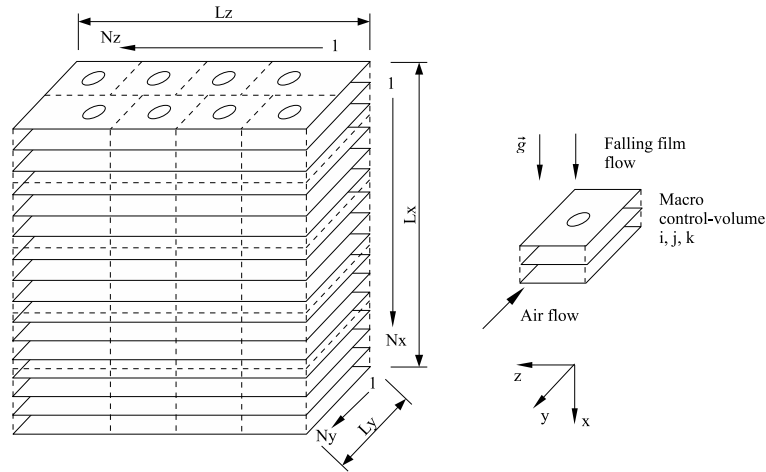
Figure 2.2: Scheme of discretisation of the air-liquid compact heat exchangers (absorber and condenser)

of resolution has a similar philosophy, as in the case of air-cooled heat exchangers [11]. The heat exchanger is divided in control volumes along the tubes (see Fig. 2.3). In these control volumes the equation of conservation of mass, momentum and energy are applied for the inner flow (water stream in this case) and the energy equation for the solid elements (tubes). The outer flow is a specific subroutine, in this case falling film desorption or pure fluid falling film evaporation. This subroutine provides the necessary boundary conditions for the calculation of the solid elements. The model needs empirical information about heat transfer and pressure drop coefficients of forced convection inside tubes [12]. This inner flow is solved in a step by step procedure (see Chapter 3).

In the solid elements, the energy equation is solved, applying the additional hypothesis that the heat transfer outside the wetted area (elbows, manifolds ...) is neglected.

2.2.3 Resolution of absorption/desorption processes (absorber, generator)

In the outer part of the generator, the same subroutine is applied as in the solution side of the air-cooled absorber. In that case, the formulation is adapted to the change in the gravity direction with respect to the tube surface. For this calculation, the
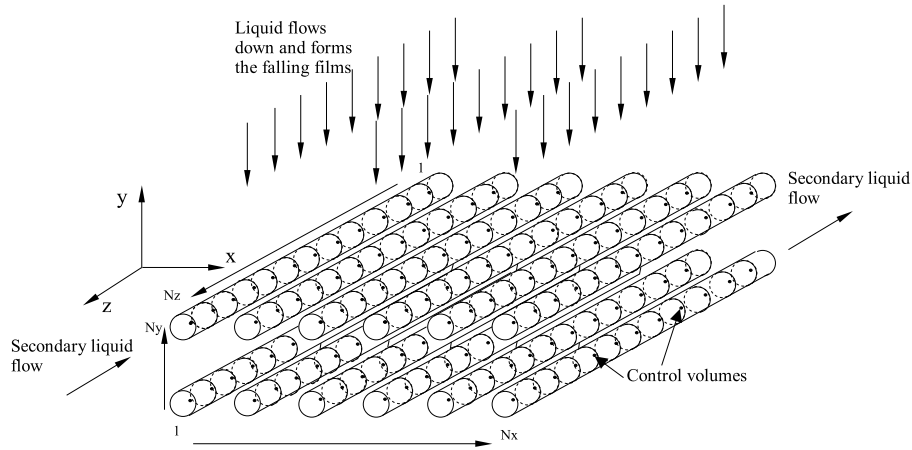
Figure 2.3: Scheme of discretisation of serpentine heat exchangers (generator and evaporator)

following hypotheses are assumed:

- Steady state flow.

- Newtonian fluid.

- Liquid film in laminar incompressible flow.

- Radius of the tube is much greater than the falling film thickness, therefore curvature effects are neglected.

- Constant physical properties, at the conditions of the beginning of the tube.

- Neglected diffusion in flow direction.

- Negligible convection terms in the direction orthogonal to the flow.

- No resistance to mass transfer in the interface, therefore, it is assumed thermodynamic equilibrium at the interface.

- No resistance to heat transfer at the vapour phase.

- No interfacial shear stress between liquid and vapour phases.

- Pressure gradients are negligible.

- For falling film flowing down inside vertical tubes, initial velocity considered as fully developed laminar regime.

- For falling film flowing down outside horizontal tubes, initial velocity considered as uniform and parallel to tube surface with the same value as the one reached for free drop between tubes.

- Dufour or Soret effects not been considered.

- Calculation of the fraction of wetted area without taking into account any particular velocity profile of the falling rivulets. The mass flow per unit length is readapted to the new area.

According the above mentioned hypotheses, the conservation equation of mass, momentum, energy and LiBr concentration can be written as:

$$\frac{\partial u}{\partial x} + \frac{\partial v}{\partial y} = 0 \tag{2.39}$$

$$u\frac{\partial u}{\partial x} + v\frac{\partial u}{\partial y} = gcos(\theta) + \nu\frac{\partial^2 u}{\partial y^2} \tag{2.40}$$

$$u\frac{\partial T}{\partial x} + v\frac{\partial T}{\partial y} = \alpha\frac{\partial^2 T}{\partial y^2} \tag{2.41}$$

$$u\frac{\partial c}{\partial x} + v\frac{\partial c}{\partial y} = D\frac{\partial^2 c}{\partial y^2} \tag{2.42}$$

The boundary conditions are the following (see Fig. 2.4):

$$x = 0, T = T_0, c = c_0, u = u_0, v = 0 \tag{2.43}$$

$$y = 0, T = T_w, \frac{\partial c}{\partial y} = 0, u = 0, v = 0 \tag{2.44}$$

$$y = \delta, T = f(p,c), \lambda\frac{\partial T}{\partial n} = -H_a\rho\frac{D}{c}\frac{\partial c}{\partial n}, \frac{\partial u}{\partial n} = 0 \tag{2.45}$$

The partial differential equations system and its boundary conditions are solved by means of a change of coordinates taking into account the variation of the falling film thickness [13]. The flow is solved in a step-by-step procedure due to the parabolic nature of the system of equations (see chapter 3). The boundary condition expressed in equation (2.45) relates the temperature and LiBr concentration by means of the equilibrium condition [1] and the relation between the heat of conduction at the liquid phase and the phase change heat. In this equation it is also indicated the absence of interfacial shear stress between liquid and vapour phases.
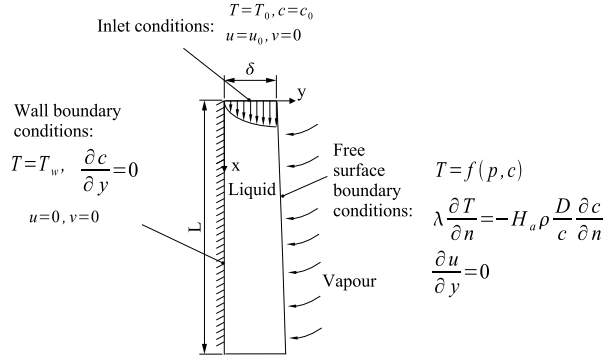
Figure 2.4: Falling film boundary conditions

This model reasonably predicts absorption and desorption phenomena over smooth surfaces under laminar flow [13, 14, 15, 16], if a complete wetted area is achieved. However, very few researchers considers the effect of an uncomplete wetted area [17, 18]. In order to consider this effect, the model of Mikielewicz et al. [19] has been implemented. This model assumes a circular profile of the rivulets and proposes a formula for calculating the fraction of wetted area (X), as function of the contact angle and mass flow per unit length, with the criteria of minimum energy. This wetted area is then introduced as a factor that reduces the heat and mass transfer with respect to the case of a complete wetted area, without taking into account any particular profile. Consequently, the mass flow rate per unit length is corrected to the new wetted area.

$$X = \frac{A'}{A} = f(\Gamma, \zeta) \tag{2.46}$$

The criterion considered for calculating the minimum flow rate to achieve a complete area wetted, is the one given by Hobler et al., also reported in [19] (see equation 2.47). This criterion has been considered due to the fact presents better agreement with the experimental data than the criterion proposed by Mikielewicz as was reported at [19]. For the case of the generator, a correction coefficient for horizontal tubes has been applied[20].

$$\delta^+ >= (\frac{3}{2})^{\frac{1}{5}}(1 - cos(\zeta))^{\frac{1}{5}} \tag{2.47}$$

Where ζ is the contact angle and δ^+ is the dimensionless critical film thickness defined as:

$$\delta^+ = (\frac{\rho^3 g^2}{15\mu^2\sigma})^{\frac{1}{5}}\delta \qquad (2.48)$$

In order to obtain the comparison of the above equation (2.47), the value of the dimensionless falling film thickness is calculated as if a complete wetted area is achieved. Therefore, the value of the falling film thickness of equation (2.48) is also calculated for a complete wettability.

The influence of falling drops between tubes is considered in the desorption process at the generator. The models suggested by Kirby and Pérez-Blanco. [21] of forming droplet and falling droplet have been applied. The tested cases shown that the influence of this last regime has not been very significant, due to the compact design of the generator.

2.2.4 Falling film condensation

For falling film condensation, the correlation proposed by Graham [**?**] of dropwise condensation has been used. Additional effects such as subcooling or interfacial shear stress have been neglected, due to the conditions of the condenser: low temperature differences (low degree of subcooling) and low vapour velocity inside the tubes.

2.2.5 Falling film evaporation

Finally, for the calculation of evaporation processes of pure refrigerant, in the outer part of the horizontal-tube falling film evaporator, a semi-empirical model has been implemented [22]. In this model four regions of heat transfer are considered each one with its own expression of heat transfer coefficient, according to the falling film flow and the temperature field: i) stagnation flow region, ii) inpingement flow region, iii) thermal developing flow region, iv) fully developed flow region. The same expression of wetted area [19] with the correction for horizontal tubes [20] has been used.

2.3 Detailed simulation of heat and mass transfer in absorption processes.

The prediction of vapour absorption in falling liquid films processes results very important for the optimisation and reduction of the absorber, the most critical heat exchanger because of its low heat and mass transfer coefficients. Thus, the reduction of the absorber's size is an aspect of prime importance, especially for low power machines. The classical models based on the resolution of boundary layer equations are able to predict reasonably the vapour absorption in liquid falling films in smooth walls [13, 14, 15], but the working conditions in real absorption machines, where

different techniques of absorption enhancement are implemented, are quite different. These techniques introduce movements in the liquid and vapour phases perpendicular to interface that boundary layer equations cannot simulate.

A more complete description of the phenomena involved implies the resolution of the Navier-Stokes equations in two-phase flow [23]. The hypotheses considered in the cases simulated are the following:

- Laminar incompressible 2-D flow.

- Newtonian fluid.

- Physical properties variable only in the term of buoyancy forces (Boussinesq approximation).

- No resistance to mass transfer in the interface, therefore it is assumed thermodynamic equilibrium at the interface.

- Dufour or Soret effects not considered.

The governing equations of the model used are:

$$\frac{\partial \rho}{\partial \tau} + \frac{\partial \rho u}{\partial x} + \frac{\partial \rho v}{\partial y} = 0 \tag{2.49}$$

$$\frac{\partial \rho u}{\partial \tau} + \frac{\partial \rho u u}{\partial x} + \frac{\partial \rho v u}{\partial y} = -\frac{\partial p}{\partial x} + \frac{\partial}{\partial x}\left(2\mu\frac{\partial u}{\partial x}\right) + \frac{\partial}{\partial y}\left(\mu\frac{\partial v}{\partial x} + \mu\frac{\partial u}{\partial y}\right) + f_x \tag{2.50}$$

$$\frac{\partial \rho v}{\partial \tau} + \frac{\partial \rho u v}{\partial x} + \frac{\partial \rho v v}{\partial y} = -\frac{\partial p}{\partial y} + \frac{\partial}{\partial y}\left(2\mu\frac{\partial v}{\partial y}\right) + \frac{\partial}{\partial x}\left(\mu\frac{\partial u}{\partial y} + \mu\frac{\partial v}{\partial x}\right) + f_y \tag{2.51}$$

$$\frac{\partial \rho C_p T}{\partial \tau} + \frac{\partial \rho u C_p T}{\partial x} + \frac{\partial \rho v C_p T}{\partial y} = \frac{\partial}{\partial x}\left(\lambda\frac{\partial T}{\partial x}\right) + \frac{\partial}{\partial y}\left(\lambda\frac{\partial T}{\partial y}\right) + S_{en} \tag{2.52}$$

$$\frac{\partial c}{\partial \tau} + u\frac{\partial c}{\partial x} + v\frac{\partial c}{\partial y} = D\left(\frac{\partial^2 c}{\partial x^2} + \frac{\partial^2 c}{\partial y^2}\right) + S_{sp} \tag{2.53}$$

$$\frac{\partial F}{\partial \tau} + u\frac{\partial F}{\partial x} + v\frac{\partial F}{\partial y} = 0 \tag{2.54}$$

Where equation (2.49) is the mass conservation, equations (2.50) and (2.51) are the x and y components of momentum conservation, respectively, equation (2.52) is the energy conservation, equation (2.53) is the conservation of the non-volatile absorbent (in this case LiBr) and equation (2.54) is the volume of fluid conservation equation. It has to be indicated that in this equation the exchange of mass between phases due to the absorption processes is neglected in equation (2.54) due to the low mass transfer

rates. Another observation to be highlighted is that for the mass species equation only liquid phase is considered, with constant fluid properties including mass diffusivity.

The source term of equations (2.50) and (2.51) are divided in gravity forces and volumetric surface tension forces:

$$f_x = \rho g_x [1 + \beta(T - T_r) + \beta^+(c - c_r)] + F_{svx} \qquad (2.55)$$

$$f_y = \rho g_y [1 + \beta(T - T_r) + \beta^+(c - c_r)] + F_{svy} \qquad (2.56)$$

The normal and tangential stresses at the interface are incorporated to the momentum equations by the consideration of variable properties in function of F. However, the balance of forces at the free surface is presented here for easy understanding:

$$p_l - p_v + \sigma\kappa = 2\mu_l \left(\frac{\partial u}{\partial n} n_x + \frac{\partial v}{\partial n} n_y \right)_l - 2\mu_v \left(\frac{\partial u}{\partial n} n_x + \frac{\partial v}{\partial n} n_y \right)_v \qquad (2.57)$$

for the normal direction at the interface, where n_x and n_y are the x and y components of the unitary normal vector to the interface, and:

$$\mu_v \left(\frac{\partial u}{\partial n} s_x + \frac{\partial v}{\partial s} n_y + \frac{\partial u}{\partial s} n_x + \frac{\partial v}{\partial n} s_y \right)_v - \mu_l \left(\frac{\partial u}{\partial n} s_x + \frac{\partial v}{\partial s} n_y + \frac{\partial u}{\partial s} n_x + \frac{\partial v}{\partial n} s_y \right)_l = \frac{\partial \sigma}{\partial s} \qquad (2.58)$$

for the tangential direction, where s_x and s_y are the x and y components of the unitary tangential vector to the interface. The surface and normal derivatives are, respectively:

$$\frac{\partial}{\partial s} = \hat{s} \cdot \vec{\nabla}, \frac{\partial}{\partial n} = \hat{n} \cdot \vec{\nabla} \qquad (2.59)$$

Equation (2.57) is the balance of the superficial forces in the normal direction to the interface, and equation (2.58) shows the balance of the superficial forces in the tangential direction. In (2.58), the surface tension variation caused by temperature and LiBr concentrations gradients plays an important role. The boundary conditions at the interface for the conservation of energy and conservation of LiBr equations, due to the absorption process, are the following:

$$\lambda_l \frac{\partial T}{\partial n} - \lambda_v \frac{\partial T}{\partial n} = -H_a \frac{D\rho}{c_{it}} \frac{\partial c}{\partial n} \qquad (2.60)$$

$$T_{it} = f(c_{it}, p_{it}) \qquad (2.61)$$

Equation (2.60) expresses the interface heat balance where the heat due to the phase change is considered. Equation (2.61) relates the temperature and the LiBr
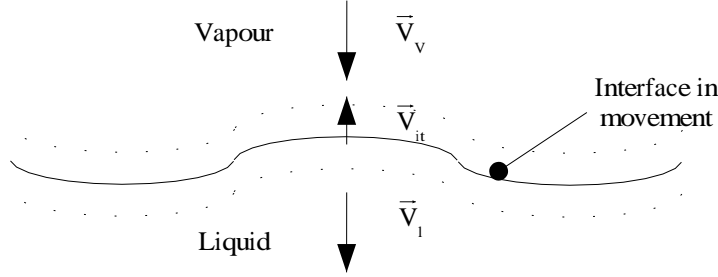
Figure 2.5: Absorption process at the interface

concentration under the hypothesis of equilibrium. This expression has been extracted from [1] for the calculations. The deduction of the mass absorbed in equation (2.60) for mobile interfaces (Fig. 2.5) proceeds as follows: the flow of mass absorbed as far as vapour and liquid is concerned can be expressed as the difference between the velocity of the fluid normal (vapour or liquid) to the interface and the velocity of the interface, multiplied by the density of the vapour or liquid (i.e., the water vapour or the water-LiBr solution):

$$\dot{m}_a = \rho_v(\vec{V}_v - \vec{V}_{it}) \cdot \hat{n} = \rho_l(\vec{V}_l - \vec{V}_{it}) \cdot \hat{n} \tag{2.62}$$

If the right side of expression (2.62) is developed, the whole flow of water-LiBr solution is divided between the flow of water and the flow of LiBr (2.63):

$$\rho_l(\vec{V}_l - \vec{V}_{it}) \cdot \hat{n} = \rho_{l,H_2O}(\vec{V}_{l,H_2O} - \vec{V}_{it}) \cdot \hat{n} + \rho_{l,LiBr}(\vec{V}_{l,LiBr} - \vec{V}_{it}) \cdot \hat{n} \tag{2.63}$$

The flow of LiBr towards the interface is zero (second term of the right hand side of the equation 2.63), because it is not volatile:

$$\rho_l(\vec{V}_l - \vec{V}_{it}) \cdot \hat{n} = \rho_{l,H_2O}(\vec{V}_{l,H_2O} - \vec{V}_{it}) \cdot \hat{n} = \rho_{l,H_2O}\vec{V}_{l,H_2O} \cdot \hat{n} - \rho_{l,H_2O}\vec{V}_{it} \cdot \hat{n} \tag{2.64}$$

For the water flow, developing the expression and applying Fick's Law, the following expression results (2.65):

$$\rho_l(\vec{V}_l - \vec{V}_{it}) \cdot \hat{n} = -\rho_l D \frac{\partial(1-c)}{\partial n} + \rho_l(1 - c_{it})\vec{V}_l \cdot \hat{n} - \rho_{l,H_2O}\vec{V}_{it} \cdot \hat{n} \tag{2.65}$$

Adding and subtracting $\rho_l(1 - c_{it})\vec{V}_{it}$ in equation (2.65) and rearranging the expression, it can be seen a term proportional to the concentration derivative, another term that is the mass flow absorbed multiplied by the water mass fraction, and a last term where the interface velocity is involved. This last term results zero, for the definition of partial density of substance:

$$\rho_l(\vec{V}_l, -\vec{V}_{it}) \cdot \hat{n} = -\rho_l D \frac{\partial(1-c)}{\partial n} + \rho_l(1 - c_{it})(\vec{V}_l - \vec{V}_{it}) \cdot \hat{n}$$
$$-\vec{V}_{it}(\rho_l(1 - c_{it}) - \rho_{l,H_2O}) \cdot \hat{n} \tag{2.66}$$

Thus, it can be operated the whole expression and find that the flow of mass absorbed is proportional to the mass flow due to molecular diffusivity in the LiBr solution (2.67):

$$\dot{m}_a = \rho_l(\vec{V}_l, -\vec{V}_{it}) \cdot \hat{n} = \frac{\rho_l D}{c_{it}} \frac{\partial c}{\partial n} \tag{2.67}$$

2.4   Nomenclature

A	heat exchange area
A'	wetted heat exchange area
c	LiBr concentration
D	mass diffusivity
e	energy
f	momentum source term
F	volume of fluid
$\vec{F}$	force integrated in a volume of control
F_{sv}	volumetric surface tension force
g	gravity
h	enthalpy
H	phase change heat
i	position of vc in x direction
j	position of vc in y direction
k	position of vc in z direction
L	falling film length
$\dot{m}$	mass flow
n	normal direction to interface
$\hat{n}$	unitary vector normal to interface
$\dot{Q}$	heat power
p	pressure

Re	Reynolds number
S	source term
$\vec{S}$	vector normal to surface
$\hat{s}$	unitary vector tangential to interface
T	temperature
U	overall heat transfer coefficient
u	velocity in x direction
v	velocity in y direction
$\vec{V}$	velocity vector
$\dot{W}$	mechanical work power
X	fraction of wetted area
x	coordinate
y	coordinate
z	coordinate

Greek symbols

α	thermal diffusivity
β	volumetric expansion coefficients due to change of temperature
β^+	volumetric expansion coefficient due to change of LiBr concentration
δ	film thickness
Γ	falling film mass flow per unit length
κ	interface curvature
λ	thermal conductivity
μ	dynamic viscosity
ν	kinematic viscosity
ρ	density
σ	surface tension
τ	time
θ	angle with respect to gravity
ζ	static contact angle

Subscripts and superscripts

0	initial value
a	absorption
abs	absorber
c	kinetic
con	condenser
en	energy
eva	evaporator

gen	generator
H_2O	water
i	internal
it	interface
LiBr	Lithium Bromide
l	liquid
m	mass
p	potential
pump	pump
r	reference
s	surface
sp	species
SHX	solution heat exchanger
v	vapour
vc	volume of control
w	wall
+	dimensionless

References

[1] ASHRAE. *ASHRAE HANDBOOK Fundamentals.* 1997.

[2] Y. Kaita. Thermodynamic Properties of Lithium Bromide-Water Solutions at High Temperatures. *International Journal of Refrigeration*, 24(5):374–390, 2001.

[3] M. Furukawa. Practical expressions for thermodynamic and transport properties of commonly used fluids. *Journal of Thermophysics and Heat Transfer*, 5(4):524–531, 1991.

[4] NIST. Thermodynamic properties of refrigerants and refrigerant mixtures database (REFPROP). Version 6.0, 1998.

[5] R. M. DiGuilio, R. J. Lee, S. M. Jeter, and A. S. Teja. Properties of Lithium Bromide-Water Solutions at High Temperatures and Concentrations. I. Thermal Conductivity. *ASHRAE Transactions*, 96(1):702–708, 1990.

[6] R. Reid, J. Prausnitz, and T. Sherwood. *The Properties of Gases and Liquids.* McGraw-Hill, 1977.

[7] K. J. Kim, N. S. Berman, and B. D. Wood. Surface Tension of Aqueous Lithium Bromide + 2-Ethyl-1-Hexanol. *Journal of Chemical and Engineering Data*, 39(-):122–124, 1994.

[8] C. Oliet, C. D. Pérez-Segarra, O. García-Valladares, and A. Oliva. Advanced numerical simulation of compact heat exchangers. Application to automotive, refrigeration and air conditioning industries. In *Proceedings of the Third European Congress on Computational Methods in Applied Sciences and Engineering (ECCOMAS)*, pages 1–19, 2000.

[9] C. Oliet, C. D. Pérez-Segarra, S. Danov, and A. Oliva. Numerical simulation of dehumidifying fin-and-tube heat exchangers. model strategies and experimental comparisons. In *Proceedings of the 2002 International Refrigeration Engineering Conference at Purdue*, 2002.

[10] N. H. Kim, J. H. Yun, and R. L. Webb. Heat transfer and friction correlations for wavy plate fin-and-tube heat exchangers. *Journal of Heat Transfer*, 119(3):560–567, 1997.

[11] J. Castro, L. Leal, P. Pozo, C.D. Pérez-Segarra, and C. Oliet. Development and performance of an air-cooled water-libr absorption cooling machine. In *Proceedings of the Forum International Sur les Energies Renouvelables*, pages 59–65, 2002.

[12] H. Y. Wong. *Handbook of Essential Formulae and Data on Heat Transfer for Engineers*. Longman, 1977.

[13] J.W. Andberg. *Absorption of Vapours into Liquid Films Flowing over Cooled Horizontal Tubes*. PhD thesis, University of Texas, 1986.

[14] G. Grossman. Simultaneous heat and mass transfer in film absorption under laminar flow. *International Journal of Heat and Mass Transfer*, 26(3):357–371, 1983.

[15] R. Yang and B.D. Wood. A numerical modelling of an absorption process on a liquid falling film. *Solar Energy*, 48(3):195–198, 1992.

[16] C. Q. Wang, Z. Lu, D. Q. Li, B. Yu-Chi, and Y. G. Sun. Heat and mass transfer in falling film generator of Lithium Bromide absorption refrigerating machine. In *Proceedings of the 19th International Congress of Refrigeration*, pages 209–214, 1995.

[17] J. K. Kim, C. W. Park, and Y. T. Kang. The effect of Micro-Scale Surface Treatment on Heat and Mass Transfer Performance for a Falling Film H_2O/LiBr Absorber. *International Journal of Refrigeration*, 26(5):575–585, 2003.

[18] V. M. Soto and J. M. Pinazo. Validation of a model for the absorption process of H_2O(vap) by a LiBr(aq) in a horizontal tube bundle, using a multi-factorial analysis. *International Journal of Heat and Mass Transfer*, 46(17):3299–3312, 2003.

[19] J. Mikielewicz and J. R. Moszynski. Minimum thickness of a liquid film flowing vertically down a solid surface. *International Journal of Heat and Mass Transfer*, 19(-):771–776, 1976.

[20] J. Tang, B. Yu-chi, and Z. Lu. Minimum wetting rate of film flow on solid surface. In *Proceedings of the XVIIIth International Congress of Refrigeration*, pages 519–523, 1991.

[21] M. J. Kirby and H. Pérez-Blanco. A design model for horizontal tube water/Lithium Bromide absorbers. In *Proceedings of the International Mechanical Engineering Congress and Exposition. AES-Vol. 32. Heat pump and refrigeration systems design, analysis, and applications*, pages 1–10, 1994.

[22] M. C. Chyu and A. E. Bergles. An Analytical and Experimental Study of Falling-Film Evaporation on a Horizontal Tube. *Journal of Heat Transfer*, 109(4):983–990, 1987.

[23] J. Castro, L. Leal, C.D. Pérez-Segarra, and P. Pozo. Numerical study of the enhancement produced in absorption processes using surfactants. *International Journal of Heat and Mass Transfer*, 47(14-16):3463–3476, 2004.

Jesús Castro Gonzàlez, *Simulation of heat and mass transfer phenomena in the critical elements of H_2O-LiBr absorption cooling machines. Experimental validation and application to design.,* Doctoral Thesis, Universitat Politècnica de Catalunya, April 2005.

Chapter 3

Numerical implementation

Abstract. The numerical implementation of the different models described in the previous chapter is presented. Concerning with the model based on overall balances between elements, the non-linear system of equations generated is solved by means of an iterative procedure, which it is herein explained. The subroutine developed for the resolution of absorption/desorption processes, under boundary layer hypotheses, used in the modeling of the heat exchangers is also described. In this case only the liquid phase is simulated, adapting the mesh to the free surface by means of a change of coordinates. The partial differential equation system is solved by means of a step-by-step procedure. Finally, the implementation of the most complete model that solves the Navier Stokes equations is also briefly presented. For solving the free surface location a surface tracking method is used, and for the calculation of surface tension forces, a continuum surface forces model is employed. The coupled equations are solved using a pressure based method of SIMPLE-like algorithm.

3.1 Overall balances based model

The model used for the simulation of the whole absorption system is based on overall balances of mass and energy, under state state conditions (see Chapter 2), together with the equations of state of LiBr aqueous solution, and water:

Total mass balance equations:

$$\sum \dot{m}_{out} - \sum \dot{m}_{in} = 0 \tag{3.1}$$

LiBr balance equations:

$$\sum \dot{m}x_{out} - \sum \dot{m}x_{in} = 0 \tag{3.2}$$

Energy equations:

$$\sum \dot{m}h_{out} - \sum \dot{m}h_{in} = \dot{Q} - \dot{W} \tag{3.3}$$

Equations of state of LiBr aqueous solution [1]:

$$h \approx h_{sol}(c, T) \tag{3.4}$$

$$T = T_{sat,sol}(p, c) \tag{3.5}$$

Equation of state of water [2]:

$$h \approx h_w(T, x) \tag{3.6}$$

$$T = T_{sat,w}(p) \tag{3.7}$$

The system of non-linear equations generated can be written in the following generic form:

$$\begin{aligned} \phi_1 &= f_1(\phi_1, \phi_2, ..., \phi_n) \\ \phi_2 &= f_2(\phi_1, \phi_2, ..., \phi_n) \\ &\qquad . \\ &\qquad . \\ &\qquad . \\ \phi_n &= f_n(\phi_1, \phi_2, ..., \phi_n) \end{aligned} \tag{3.8}$$

The system of equations is solved by an iterative procedure (Gauss-Seidel method), where the most updated variables values (ϕ_i) are used in each function according to a previously determined order. Another method of resolution has been tested and discarded [3] due to its behaviour results quite unpredictable, and, consequently, its use is difficult for the designer, although in some situations is more effective than Gauss-Seidel algorithm. This method is based in the combination of a Newton-Raphson method together with a method of minimisation of the residual of the equations (the set of equations are equalled to zero).

3.2 Boundary layer based model for absorption / desorption processes

As indicated in the previous chapter, a model where conservation equations are simplified under the boundary layer hypotheses [4, 5, 6, 7] can be enough for the calculation of absorption / desorption processes over smooth surfaces (with total wetted area). In this thesis the resolution procedure is quite similar to the one followed by Andberg at [4]. Therefore, only the differences related with the numerical resolution are reported.

In the case of absorption/desorption over horizontal tubes, three hydrodynamic regions are assumed (see Fig. 3.1) in 2-dimensional flow. The first region, called turning jet region, is characterised by a potential flux. The final velocity (parallel to surface) is assumed the same as the resulting from the free drop from one tube to the next one. A difference with respect to Andberg [4], is that this region is not calculated here. The second region is called turned jet region. In this region a viscous boundary layer zone is formed due the friction to the solid surface. This region ends when the boundary layer zone constitutes the whole falling film. Finally, in the third region (fully viscous film) there is only viscous regime.
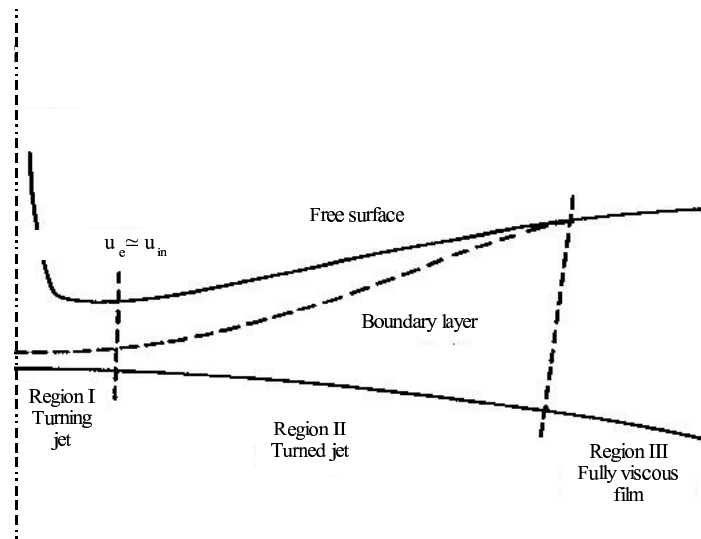
Figure 3.1: Different hydrodynamic regions (modified figure from [4])

The thickness of the falling film is variable, due to the boundary conditions of the problem and the change in the gravity direction as consequence of the curvature of the tube. In order to use in the calculations orthogonal coordinates with a structured mesh, a change of coordinates is performed.

3.2.1   Normalisation in the turned jet region

This region is only calculated for the case of serpentine heat exchangers of horizontal tubes (generator). In order to use orthogonal coordinates adapted to the falling film free surface, these are the new coordinates used (dimensionless):

$$\xi = \frac{x}{L} = \frac{x}{\pi R} \tag{3.9}$$

$$\eta = \sqrt{\frac{u_e}{\nu x}} y \tag{3.10}$$

Therefore, the partial derivatives are:

$$\frac{\partial}{\partial x} = \frac{1}{L}\frac{\partial}{\partial \xi} - \frac{1}{2}\left(\left(\frac{y}{\sqrt{\nu u_e x}}\right)\frac{\partial u_e}{\partial x} - \frac{y}{x}\sqrt{\frac{u_e}{\nu x}}\right)\frac{\partial}{\partial \eta} \tag{3.11}$$

$$\frac{\partial}{\partial y} = \sqrt{\frac{u_e}{\nu x}}\frac{\partial}{\partial \eta} \tag{3.12}$$

$$\frac{\partial^2}{\partial y^2} = \frac{u_e}{\nu x}\frac{\partial^2}{\partial^2 \eta} \tag{3.13}$$

The coordinate parallel to the solid surface is normalised using the maximum possible distance (half tube perimeter). The other coordinate is normalised by the thickness of the viscous boundary layer. Therefore, $\eta \geq 1$ potential zone, and $\eta < 1$ indicates boundary layer.

It has to be considered that the partial derivative of the entrance velocity (u_e) with respect to x-coordinate is neglected. This approximation is quite accurate in the turned jet region, because in this region u_e basically varies by variations of potential energy which are very small in this region, because this region represents a small part of the tube perimeter.

The velocities in such coordinates system are defined as:

$$f' = f'(\xi, \eta) = u/u_e \tag{3.14}$$

$$V = V(\xi, \eta) = \frac{u}{u_e}\sqrt{u_e x/\nu} \tag{3.15}$$

Thus, the mass conservation equation results:

$$\xi\frac{\partial f'}{\partial \xi} - \frac{\eta}{2}\frac{\partial f'}{\partial \eta} + \frac{\partial V}{\partial \eta} = 0 \tag{3.16}$$

and momentum conservation:

$$f'\xi\frac{\partial f'}{\partial \xi} + (V - \frac{1}{2}\eta f')\frac{\partial f'}{\partial \eta} = \gamma + \frac{\partial^2 f'}{\partial \eta^2} \tag{3.17}$$

where:

$$\gamma = \frac{g\xi L cos(\theta)}{u_e^2}$$

It has to be highlighted that neither the energy equation nor the LiBr conservation equation are solved. However, as it has been explained above, this region represents only a small part of the perimeter of the tube. This calculation provides of a good starting velocity value for the complete calculations in the next region.

3.2.2 Normalisation in the fully viscous film region

This region is calculated for both the horizontal tube, serpentine generator, and the vertical tubes absorber. For this region, the normalisation is:

$$\xi = \frac{x}{L} \tag{3.18}$$

$$\zeta = \frac{y}{\delta(x)} \tag{3.19}$$

L is the half perimeter of the tube in the case of the serpentine heat exchangers and the tube length in the case of the tube-fin ones. The partial derivatives are:

$$\frac{\partial}{\partial x} = \frac{1}{L}\frac{\partial}{\partial \xi} - \frac{y}{\delta^2}\frac{d\delta}{dx}\frac{\partial}{\partial \zeta} \tag{3.20}$$

$$\frac{\partial}{\partial y} = \frac{1}{\delta}\frac{\partial}{\partial \zeta} \tag{3.21}$$

$$\frac{\partial^2}{\partial y^2} = \frac{1}{\delta^2}\frac{\partial^2}{\partial^2 \zeta} \tag{3.22}$$

The mass conservation equation, under the transformed coordinates is:

$$\xi\frac{\partial \rho u}{\partial \xi} - \beta\zeta\frac{\partial \rho u}{\partial \zeta} + \varepsilon\frac{\partial \rho v}{\partial \zeta} = 0 \tag{3.23}$$

Momentum conservation equation is treated in terms of constant physical properties, As a difference with respect to Andberg calculations at [4]:

$$u\xi\frac{\partial u}{\partial \xi} - \beta\zeta u\frac{\partial u}{\partial \zeta} + v\varepsilon\frac{\partial u}{\partial \zeta} = \gamma + \kappa\nu\frac{\partial^2 u}{\partial \zeta^2} \qquad (3.24)$$

where:

$$\beta = \frac{x}{\delta}\frac{d\delta}{dx} = \frac{\xi}{\delta}\frac{d\delta}{d\xi}; \varepsilon = \frac{x}{\delta} = \frac{\xi L}{\delta}; \gamma' = xg(x) = g\xi L cos(\theta); \kappa = x/\delta^2 = \xi L/\delta^2$$

Energy equation. As a difference with respect to Andberg calculations at [4], the energy equation is treated in terms of constant physical properties:

$$\frac{\partial T}{\partial \xi} = \left(\frac{\zeta}{\delta}\frac{\partial \delta}{\partial \xi} - \frac{v}{u}\frac{L}{\delta}\right)\frac{\partial T}{\partial \zeta} + \frac{\alpha}{\delta^2}\frac{L}{u}\frac{\partial^2 T}{\partial \zeta^2} \qquad (3.25)$$

And finally, in the same way (constant physical properties) the LiBr conservation equation:

$$\frac{\partial c}{\partial \xi} = \left(\frac{\zeta}{\delta}\frac{\partial \delta}{\partial \xi} - \frac{v}{u}\frac{L}{\delta}\right)\frac{\partial c}{\partial \zeta} + \frac{D}{\delta^2}\frac{L}{u}\frac{\partial^2 c}{\partial \zeta^2} \qquad (3.26)$$

The reason why in the case of vertical tubes only the last region is calculated, is due to the fact that the Nusselt's profile of velocity of the falling film as a quite good starting value for the step-by-step calculation is considered.

3.2.3   Algorithms resolution

The discretization of the set of equations is quite similar to the one described by Andberg based on finite difference formulation at reference [4]. In this procedure, the same mesh is used for all the variables (collocated mesh) in the step-by-step calculation. Applying the corresponding boundary conditions (see chapter 2) the algorithm for the calculation of the turned jet region is:

1. Coupled resolution of momentum and mass equations, to obtain the values of the components of velocity in the next row of the domain. The equations are parabolic with respect to the coordinate parallel to the solid wall. Therefore each row is referred to a row of points with the same value of ξ coordinate..

2. Calculation of the boundary layer thickness: $\delta_b = \sqrt{(\nu x/u_e)}\eta_{99.9}$, thus, the point where the component of velocity parallel to solid wall reaches the 99.9% of its value in the potential region (it can be observed from the calculation that this component of velocity from that point onwards - following the η coordinate - does not vary).

3. Calculation of the mass flow in the boundary layer: $\dot{m}_b = \int_0^{\delta_b} \rho u \, dy$ and the mass flow in the potential zone: $\dot{m}_{pot} = \dot{m} - \dot{m}_b$

4. Calculation of the falling film thickness: $\delta = \delta_b + \dot{m}_{pot}/\rho u_e$

5. Check if $\dot{m}_b \leq \dot{m}$. If so, the calculation follows to the next row of points following the ξ coordinate (go to point 1). If not, go to fully viscous region.

And for the fully viscous film:

1. Take u, v, and $\delta = \delta_b$ of the end of the previous region.

2. Coupled resolution of momentum and mass equations, to obtain the values of the components of velocity in the next row of the domain. The equations are parabolic with respect to the coordinate parallel to the solid wall, therefore each row is referred to a whole of points with the same value of ξ coordinate.

3. Coupled resolution of the energy and LiBr conservation equations.

4. Calculation of the mass absorbed: $\dot{m}_{abs} = -\frac{\rho D}{c} \frac{\partial c}{\partial y} \Delta x$

5. Calculation of the total mass flow with: $\dot{m} = \int_0^1 \rho u \, d\zeta$

6. Check if $\dot{m} = \dot{m}_{pre} + \dot{m}_{abs}$. If so, continue with the calculation (point 1, previous checking that we are not at the of the domain). If not, estimate δ again and go to point 2.

Figs. 3.2 and 3.2 show the flow chart for the algorithms applied in the calculation of the two hydrodynamic regions. In both regions, for each step calculation the coupling between equations of mass and momentum conservation is solved by means of the double-TDMA algorithm [4]. This algorithm solves directly the system of equations generated. To solve the energy and mass species equations the classic TDMA algorithm [8] is employed.
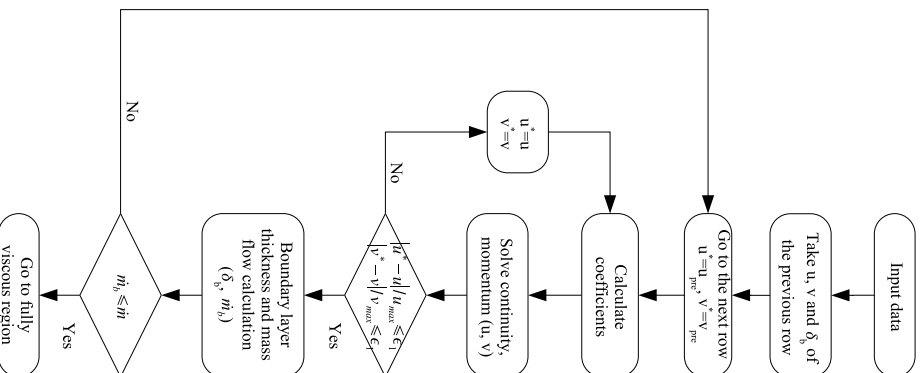
Figure 3.2: Flow chart for the algorithm used in the turned jet region
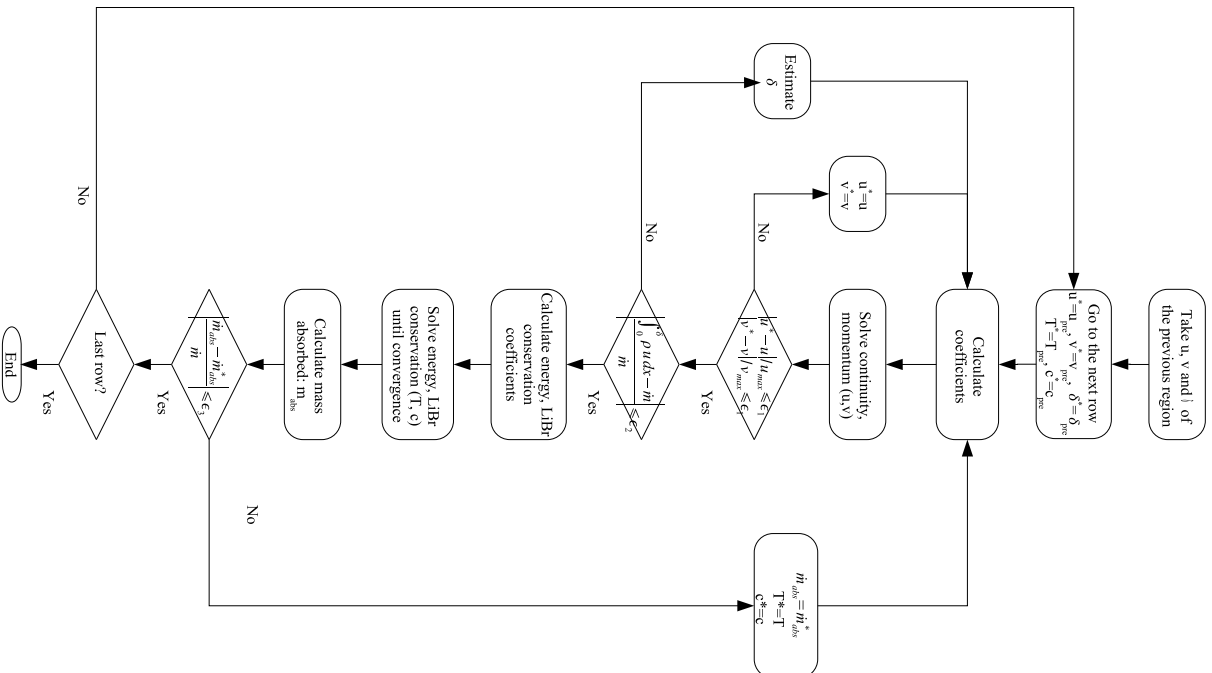
Figure 3.3: Flow chart for the algorithm used in the fully viscous region
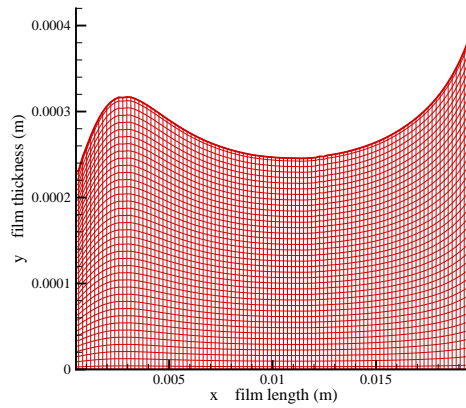
Figure 3.4: Typical curvilinean mesh for a falling film flowing down an horizontal tube
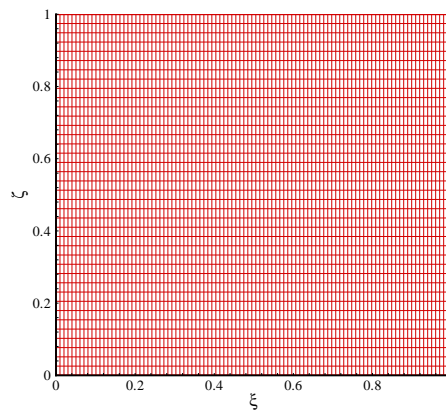
Figure 3.5: Mesh in the transformed equations (fully viscous region)

As an illustrative example, Fig. 3.4 shows a typical mesh produced in the calculation of a film over an horizontal tube, developed over the x-axis. On the

graphic, the film thickness and film length are not in the same scale. It can be observed that at the beginning, the thickness is very low, mainly due to the high value of the initial velocity (u_e). Then, the growth of the boundary layer implies an increment of the falling film thickness. After reaching a maximum value, the increment of the component of the gravity force parallel to flow lead to an increment of the velocity, therefore film thickness decreases again until reaching a minimum value near the point were the gravity is maximum ($\theta = 90$ °). In the last part, the film thickness increases again due to the decrement of the velocities, because the component of gravity parallel to the flow decreases. Figure 3.5 show the mesh in transformed coordinates.

3.2.4 Numerical verification

Before comparing the numerical results with the experimental data obtained from the prototypes developed (experimental validation), it is necessary to verificate the code in order to check the quality of the numerical solutions obtained of the partial differential equations. Numerical errors can be originated by programming errors, convergence errors, discretization errors, etc. It is supposed than all possible programming errors have been depurated. Therefore, a numerical study has been carried in order to verificate the influence of the convergence errors and another study to check performance of the different discretization meshes (discretization errors) used in the resolution of falling film absorption/desorption processes.

The benchmark case considered is the absorption over an horizontal tube. Table 3.1 shows the geometry and working conditions for the studied case.

Geometry	
Tube diameter	0.127 m
Working conditions	
Inlet solution mass flow	0.077 kg/s/m
Inlet temperature	40°C
Inlet LiBr concentration	0.60
Wall temperature	30°C

Table 3.1: Geometry and working conditions for the case studied

Convergence errors

There are four different iteration procedures depending on the two algorithms of the two hydrodynamic regions. Therefore, four correspondent different convergence criteria must be considered (all of them have been considered in a dimensionless form):

1. The change of velocity between two consecutive iterations, after solving momentum and continuity equations (ϵ_1).

2. Mass imbalance between the integration of the velocities profile and the input falling liquid film mass flow (ϵ_2).

3. The change of mass absorbed between two consecutive iterations at the interface (ϵ_3), or the coupling between energy and mass species conservation equations on the one hand, and mass and momentum conservation equations.

4. The heat inbalance at the interface (ϵ_4, see equation 2.45 of Chapter 2), in other words, the coupling between energy and LiBr conservation equations.

In the different studies the data computed are, by order: heat exchanged to the tube (one side), mass absorbed (one side), final temperature and final concentration. The dimensionless steps used for the turned jet region are 4e-6 and 0.1 for the ξ and η coordinates, respetively. For the fully viscous region the mesh used is 800 steps in flow direction and 80 steps in the orthogonal direction (both uniform).

Table 3.2 shows the results for the two convergence criteria related to the coupling of continuity and momentum, ϵ_1 and ϵ_2.

ϵ_1	ϵ_2	Q (W/m)	m_{abs} (kg/m)	T_{out} ($^\circ$C)	c_{out} (LiBr)
$1 \cdot 10^{-3}$	$1 \cdot 10^{-3}$	4519	$0.92 \cdot 10^{-4}$	38.01	0.5986
$1 \cdot 10^{-5}$	$1 \cdot 10^{-3}$	4540	$0.92 \cdot 10^{-4}$	38.01	0.5986
$1 \cdot 10^{-4}$	$1 \cdot 10^{-4}$	4423	$1.17 \cdot 10^{-4}$	38.10	0.5982
$1 \cdot 10^{-5}$	$1 \cdot 10^{-4}$	4421	$1.16 \cdot 10^{-4}$	38.09	0.5982
$1 \cdot 10^{-1}$	$1 \cdot 10^{-5}$	4386	$1.21 \cdot 10^{-4}$	38.05	0.5981
$1 \cdot 10^{-2}$	$1 \cdot 10^{-5}$	4413	$1.20 \cdot 10^{-4}$	38.11	0.5981
$1 \cdot 10^{-3}$	$1 \cdot 10^{-5}$	4413	$1.20 \cdot 10^{-4}$	38.11	0.5981
$1 \cdot 10^{-4}$	$1 \cdot 10^{-5}$	4414	$1.20 \cdot 10^{-4}$	38.11	0.5981
$1 \cdot 10^{-5}$	$1 \cdot 10^{-5}$	4414	$1.20 \cdot 10^{-4}$	38.11	0.5981
$1 \cdot 10^{-6}$	$1 \cdot 10^{-5}$	4413	$1.20 \cdot 10^{-4}$	38.11	0.5981
$1 \cdot 10^{-5}$	$1 \cdot 10^{-6}$	4412	$1.20 \cdot 10^{-4}$	38.12	0.5981
$1 \cdot 10^{-6}$	$1 \cdot 10^{-6}$	4411	$1.21 \cdot 10^{-4}$	38.11	0.5981

Table 3.2: Convergence study depending on ϵ_1 & ϵ_2

From the results, it is observed that the convergence criteria related to the estimation of falling film thickness δ (ϵ_2) has higher influence in the final results than the one related of the coupled resolution of momentum-continuity equations (ϵ_1). Almost asymptotical values are reached with residuals under 10^{-5}.

Table 3.3 shows the results for the two other convergence criteria, ϵ_3 and ϵ_4. In this case, it is observed than the two convergence criteria have almost the same influence to the numerical results. Asymptotical values are reached with residuals under 10^{-2}. Acceptable results are achieved with residuals under 10^{-2}.

ϵ_3	ϵ_4	Q (W/m)	m_{abs} (kg/m)	T_{out} (°C)	c_{out} (LiBr)
$1 \cdot 10^{0}$	$1 \cdot 10^{0}$	4348	$1.40 \cdot 10^{-4}$	37.93	0.5978
$1 \cdot 10^{-5}$	$1 \cdot 10^{0}$	4406	$1.21 \cdot 10^{-4}$	38.09	0.5981
$3 \cdot 10^{-1}$	$1 \cdot 10^{-1}$	4401	$1.19 \cdot 10^{-4}$	38.07	0.5981
$1 \cdot 10^{-5}$	$1 \cdot 10^{-1}$	4407	$1.19 \cdot 10^{-4}$	38.09	0.5981
$1 \cdot 10^{-1}$	$1 \cdot 10^{-1}$	4417	$1.20 \cdot 10^{-4}$	38.11	0.5981
$1 \cdot 10^{-5}$	$1 \cdot 10^{-1}$	4417	$1.20 \cdot 10^{-4}$	38.11	0.5981
$1 \cdot 10^{-2}$	$1 \cdot 10^{-2}$	4414	$1.20 \cdot 10^{-4}$	38.11	0.5981
$1 \cdot 10^{-5}$	$1 \cdot 10^{-2}$	4414	$1.20 \cdot 10^{-4}$	38.11	0.5981
$1 \cdot 10^{-3}$	$1 \cdot 10^{-3}$	4413	$1.20 \cdot 10^{-4}$	38.11	0.5981
$1 \cdot 10^{-5}$	$1 \cdot 10^{-3}$	4414	$1.20 \cdot 10^{-4}$	38.11	0.5981
$1 \cdot 10^{-4}$	$1 \cdot 10^{-4}$	4414	$1.20 \cdot 10^{-4}$	38.11	0.5981
$1 \cdot 10^{-5}$	$1 \cdot 10^{-4}$	4414	$1.20 \cdot 10^{-4}$	38.11	0.5981
$1 \cdot 10^{0}$	$1 \cdot 10^{-5}$	4366	$1.32 \cdot 10^{-4}$	37.96	0.5979
$3 \cdot 10^{-1}$	$1 \cdot 10^{-5}$	4407	$1.20 \cdot 10^{-4}$	38.09	0.5981
$1 \cdot 10^{-1}$	$1 \cdot 10^{-5}$	4414	$1.20 \cdot 10^{-4}$	38.11	0.5981
$1 \cdot 10^{-2}$	$1 \cdot 10^{-5}$	4415	$1.20 \cdot 10^{-4}$	38.11	0.5981
$1 \cdot 10^{-3}$	$1 \cdot 10^{-5}$	4414	$1.20 \cdot 10^{-4}$	38.11	0.5981
$1 \cdot 10^{-4}$	$1 \cdot 10^{-5}$	4414	$1.20 \cdot 10^{-4}$	38.11	0.5981
$1 \cdot 10^{-5}$	$1 \cdot 10^{-5}$	4414	$1.20 \cdot 10^{-4}$	38.11	0.5981

Table 3.3: Convergence study depending on ϵ_3 & ϵ_4

Discretization errors

A study of discretization errors has been carried out for each hydrodynamic region: turned jet and fully viscous film. Concerning to the turned jet region, Table 3.4 shows the results for different discretization meshes. $\Delta\eta$ and $\Delta\xi$ are the length of the calculation steps, in dimensionless coordinates, towards the flow direction and in the orthogonal direction, respectively. The data computed are, by order: position where the it located the change of region (X) and the falling liquid film thickness (δ) at this point.

From the results, it is observed than steps in η and ξ directions of 0.1 and 4e-6, respectively, are enough for assuring results quite close to the numerical asymptotic ones (0.8% of difference in X position where the change of region is located , and 1.1%

of δ value at this position).

$\Delta\xi$	$\Delta\eta$	X (m)	δ (m)
4e-6	0.20	$0.76{\cdot}10^{-5}$	$1.14{\cdot}10^{-4}$
4e-7	0.20	$0.77{\cdot}10^{-5}$	$1.15{\cdot}10^{-4}$
4e-3	0.10	$1.01{\cdot}10^{-5}$	$0.93{\cdot}10^{-4}$
4e-4	0.10	$1.52{\cdot}10^{-5}$	$1.15{\cdot}10^{-4}$
4e-5	0.10	$0.91{\cdot}10^{-5}$	$1.21{\cdot}10^{-4}$
4e-6	0.10	$0.87{\cdot}10^{-5}$	$1.20{\cdot}10^{-4}$
4e-7	0.10	$0.88{\cdot}10^{-5}$	$1.21{\cdot}10^{-4}$
4e-6	0.05	$0.87{\cdot}10^{-5}$	$1.20{\cdot}10^{-4}$
4e-7	0.05	$0.88{\cdot}10^{-5}$	$1.21{\cdot}10^{-4}$

Table 3.4: Results in the turned jet region for different discretizations

Table 3.5 shows the results for different discretization meshes for the fully viscous region. N and M are the number of steps in the flow direction and in the orthogonal direction (uniform mesh), respectively. As in the convergence studies, the data computed are, by order: heat exchanged to the tube (one side), mass absorbed (one side), final temperature and final concentration.

From the results it can be said that values of N=800 and M=80 could be considered as a good compromise between precision and CPU time (1,4% of difference for the heat exchanged and 2.6% for the mass absorbed).

N	M	Q (W/m)	m_{abs} (kg/m)	T_{out} (°C)	c_{out} (LiBr)
100	40	4315	$1.57 \cdot 10^{-4}$	38.18	0.5976
200	40	4435	$1.40 \cdot 10^{-4}$	38.22	0.5978
400	40	4446	$1.30 \cdot 10^{-4}$	38.19	0.5980
800	40	4458	$1.26 \cdot 10^{-4}$	38.19	0.5980
1600	40	4467	$1.27 \cdot 10^{-4}$	38.25	0.5980
3200	40	4461	$1.23 \cdot 10^{-4}$	38.21	0.5981
200	80	4246	$1.50 \cdot 10^{-4}$	38.10	0.5977
400	80	4395	$1.27 \cdot 10^{-4}$	38.11	0.5980
800	80	4414	$1.20 \cdot 10^{-4}$	38.11	0.5981
1600	80	4414	$1.20 \cdot 10^{-4}$	38.16	0.5981
3200	80	4418	$1.18 \cdot 10^{-4}$	38.16	0.5982
6400	80	4411	$1.18 \cdot 10^{-4}$	38.16	0.5982
400	160	4372	$1.40 \cdot 10^{-4}$	38.21	0.5978
800	160	4405	$1.28 \cdot 10^{-4}$	38.18	0.5980
1600	160	4423	$1.21 \cdot 10^{-4}$	38.11	0.5981
3200	160	4403	$1.24 \cdot 10^{-4}$	38.26	0.5981
6400	160	4356	$1.20 \cdot 10^{-4}$	38.23	0.5981
12800	160	4331	$1.10 \cdot 10^{-4}$	38.09	0.5983
25600	160	4352	$1.17 \cdot 10^{-4}$	38.14	0.5982

Table 3.5: Results in the fully viscous region for different discretizations

3.3 Navier-Stokes equations based model

In this model, the discretization of the equations has been performed according to the procedure of finite volumes suggested by Patankar at [8] using staggered grids for the velocity fields. The coupling between pressure and velocities is solved with a segregated SIMPLE-like algorithm [8] (SIMPLEC). The incompressibility condition is applied by means of a "volume continuity equation" [9] in order to apply the same equation for the whole domain. Concerning to the volume of fluid equation, the interface tracking algorithm based on the piecewise constant/stairstepped VOF method proposed by Hirt and Nichols [10] is used to reduce the numerical smearing of the variable F.

For the resolution of continuity correction equation, the MSIP solver, together with multigrid techniques, are used [11] in order to accelerate the convergence. For the rest of equations, momentum, energy and mass species, the same solver (MSIP) has been employed.

The physical properties (density, viscosity, thermal conductivity and heat

capacity) are ponderated according to the value of the volume of fluid function as the following expression (variable density method):

$$\phi = \phi_{liq}F + \phi_{vap}(1 - F) \tag{3.27}$$

The diffusion fluxes (heat conduction, viscous stresses) are computed by means of the harmonic mean method [8] that ensures the continuity of these fluxes across the interface.

For the calculation of surface tension forces, heat of absorption and mass absorbed, a continuum method is employed (CSF) [12]. This technique interprets a surface boundary condition as a continuous two-dimensional effect only active in the interface zone, where there are gradients of the volume of fluid function F. Therefore, the surface tension forces are converted into forces per unit volume (F_{sv})[13, 14], and the heat of absorption into a volumetric heat source (source term of equation (2.52)). Both are calculated from the normal vectors at the free surface. For the calculation of normal vectors, the ALE-like scheme [12] (Indirect Differentiation to the Unit Normal) has been adopted. Thus, according to the CSF model, the surface tension forces are:

$$\vec{F}_{svn}(\vec{x}) = 2F\sigma\kappa\vec{\nabla}F(\vec{r}) \tag{3.28}$$

for the normal direction and:

$$\vec{F}_{svs} = 2F\left[\hat{i}\left(\hat{s}_x^2\frac{\partial\sigma}{\partial x} + \hat{s}_x\hat{s}_y\frac{\partial\sigma}{\partial y}\right) + \hat{j}\left(\hat{s}_y^2\frac{\partial\sigma}{\partial y} + \hat{s}_x\hat{s}_y\frac{\partial\sigma}{\partial x}\right)\right]|\vec{\nabla}F(\vec{r})| \tag{3.29}$$

for the tangential direction.

Both forces are biased to liquid side in order to facilitate convergence. The boundary condition of the absorption process is implemented in a similar way that the surface tension forces. From the point of view of the mass species equation, the concentration is calculated from a mass balance over the volume of control. Respect to the energy equation, the boundary condition is the heat due to the phase change process. Both effects are introduced as a volumetric influence in the interface zone at the source term of the respective algebraic equation:

$$S_{sp} = -2FD\frac{\partial c}{\partial n}|\vec{\nabla}F(\vec{r})| \tag{3.30}$$

$$S_{en} = -2FH_a\frac{D\rho}{c_{eq}}\frac{\partial c}{\partial n}|\vec{\nabla}F(\vec{r})| \tag{3.31}$$

Where c_{eq} is the equilibrium LiBr concentration at the given conditions of temperature and pressure:
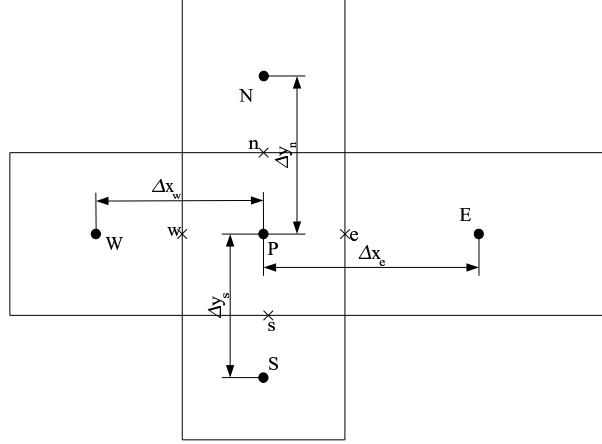
Figure 3.6: Geometry of a generic control volume

$$c_{eq} = c_{sat,sol}(p_a, T) \tag{3.32}$$

Finally, two aspects have to be highlighted: i) The partial derivative of concentration with respect to the normal direction to interface (n) is calculated by adding the finite difference approximation in each direction ponderated by the respective component of the normal vector to interface (equation 3.33); ii) as in the case of the surface tension forces, the phase change heat and liquid mass produced due to absorption process are biased to the liquid side.

$$
\begin{aligned}
\frac{\partial c}{\partial n} \approx \Bigg(& \left[\frac{(c_{eq,E} - c_{blk,P})}{\Delta x_e} n_{x,e} + \frac{(c_{eq,P} - c_{blk,W})}{\Delta x_w} n_{x,w} \right]^2 \hat{n}_{x,P}^2 \\
& + \left[\frac{(c_{eq,N} - c_{blk,P})}{\Delta y_n} n_{y,n} + \frac{(c_{eq,P} - c_{blk,S})}{\Delta y_s} n_{y,s} \right]^2 \hat{n}_{y,P}^2 \Bigg)^{1/2}
\end{aligned}
\tag{3.33}
$$

c_{blk} is the value of the correspondent concentration in the control volumes and c_{eq} is the equilibrium concentration calculated from the value of the respective temperature. For an easier understanding, Fig. 3.6 shows the geometry of a generic control volume, indicating the position of the adjacent faces and points.

3.4   Nomenclature

c	LiBr concentration (mass fraction)
D	mass diffusivity
F	volume of fluid
$\vec{F_{sv}}$	volumetric surface tension force
f'	dimensionless velocity in ξ coordinate
H	phase change heat
h	enthalpy
$\hat{i}$	unitary normal vector in x direction
$\hat{j}$	unitary normal vector in y direction
L	falling film length
$\dot{m}$	mass flow par unit length
n	normal direction to interface
$\hat{n}$	unitary normal vector to interface
p	pressure
R	tube radius
$\vec{r}$	position vector
S	source term
s	tangential direction to interface
$\hat{s}$	unitary tangential vector to interface
T	temperature
u	component of velocity in x direction
V	dimensionless velocity in η coordinate
v	component of velocity in y direction
X	x-position where it is located the change of region
x	coordinate parallel to wall
y	coordinate orthogonal to wall
Greek symbols	
α	thermal diffusivity
β	term of equations 3.23 and 3.24
δ	falling film thickness
ϵ	convergence tolerance
η	dimensionless coordinate
γ	term of equation 3.17
γ'	term of equation 3.24
κ	term of equation 3.24
ν	kinematic viscosity
ϕ	generic variable
ρ	density

θ	angle of falling film with respect to gravity
ε	term of equations 3.24 and 3.23
ξ	dimensionless coordinate
ζ	dimensionless coordinate

Subscripts and superscripts

a	absorption
abs	absorbed
b	referred to boundary layer
blk	bulk
e	entrance
en	energy
eq	equilibrium
i	inlet
liq	liquid
max	maximum
o	outlet
pot	referred to potential zone
pre	previous row
sp	species
vap	vapour
*	estimated value

References

[1] ASHRAE. *ASHRAE HANDBOOK Fundamentals*. 1997.

[2] M. Furukawa. Practical expressions for thermodynamic and transport properties of commonly used fluids. *Journal of Thermophysics and Heat Transfer*, 5(4):524–531, 1991.

[3] M.J.D. Powell. *Numerical methods for non-linear algebraic equations*, volume A hybrid method for non-linear equations. Gordon and Breach Science, London, 1970.

[4] J.W. Andberg. *Absorption of Vapours into Liquid Films Flowing over Cooled Horizontal Tubes*. PhD thesis, University of Texas, 1986.

[5] G. Grossman. Simultaneous heat and mass transfer in film absorption under laminar flow. *International Journal of Heat and Mass Transfer*, 26(3):357–371, 1983.

[6] R. Yang and B.D. Wood. A numerical modelling of an absorption process on a liquid falling film. *Solar Energy*, 48(3):195–198, 1992.

[7] C. Q. Wang, Z. Lu, D. Q. Li, B. Yu-Chi, and Y. G. Sun. Heat and mass transfer in falling film generator of Lithium Bromide absorption refrigerating machine. In *Proceedings of the 19th International Congress of Refrigeration*, pages 209–214, 1995.

[8] S. V. Patankar. *Numerical Heat Transfer and Fluid Flow*. Hemisphere Publishing Corporation, 1980.

[9] K. M. Kelkar and S. V. Patankar. Numerical Method for the Prediction of Free Surface Flows in Domains with Moving Boundaries. *Numerical Heat Transfer, Part B*, 31(1):387–399, 1997.

[10] B.D. Hirt, C.W.and Nichols. Volume of fluid (VOF) method for the dynamics of free boundaries. *Journal of Computational Physics*, 39(5):201–225, 1981.

[11] P. S. Sathyamurthy. *Development and evaluation of efficient solution procedures for fluid flow and heat transfer problems in complex geometries*. PhD thesis, University of Minnesota, 1991.

[12] A. Brandt and I. Yavneh. On multigrid solution of high-reynolds incompressible entering flows. *Journal of Computational Physics*, 101:151–164, 1992.

[13] R.C. Kothe, D.B.and Mjolsness. RIPPLE: a new model for incompressible flows with free surfaces. *AIAA Journal*, 30(11):2694–2700, 1992.

[14] G. P. Sasmal and J. I. Hochstein. Marangoni Convection with a Curved and Deforming Free Surface in a Cavity. *Journal of Fluids Engineering*, 116(3):577–582, 1994.

Chapter 4

Numerical study of absorption processes using surfactants

Abstract. The most detailed model described in chapter 2, that considers the Navier-Stokes equations is used to study the influence of surfactants, substances that improve heat and mass transfer in absorption machines due to Marangoni effect. Two common surfactants for LiBr aqueous solutions, 1-octanol and 2-ethyl-1-hexanol, are numerically tested and the absorption enhancement produced in a stagnant pool is compared with other researchers' results. For falling film absorption some other results are shown.

4.1 Introduction

There are mainly two passive methods of improving the absorption processes. A first method consists on the use of advanced surfaces for the heat and mass exchange, e.g. finned tubes [1]. These surfaces increase the exchange area as well as improve the mixing of refrigerant into the solution. A second method employed consists on the use of surfactants. These substances cause gradients of surface tension in the water-LiBr solution, and these gradients induce additional liquid movements at the interface called Marangoni convection [2]. These movements of the liquid falling film also decreases the resistance to heat and mass transfer between the liquid and vapour phases. In both cases the models based on the resolution of the governing equations under boundary layer hypotheses do not take into account the additional movements appeared. Therefore, a more complete model based on the resolution of the Navier-Stokes equations has to be used.

Mainly two mechanisms have been proposed for explaining the surface tension gradients: i) the existence of surfactant 'islands' not dissolved in the interface liquid-vapour [2]; ii) the presence of surfactant at the interface caused by the 'salting out' mechanism [3, 4]. This second mechanism is responsible of the absorption improvements with surfactant concentrations under the solubility limit, when the surfactant 'islands' cannot be formed. Daiguji et al. [4] employed the 'salting out' model for simulating the water vapour absorption in a stagnant pool of LiBr under the solubility limit of surfactant. Their results, that were reproduced in a previous work [5], indicate that in the case of the strongest enhancements of the absorption rates caused by interface movements, there has not been good agreement between the numerical results and the experimental data. Many reasons could explain the difference between theoretical and experimental values like limitations of the numerical model employed, interfacial phenomena related to the Marangoni instability not well explained by the 'salting out' effect, especially in cases where the departure from equilibrium is large or the concentration of surfactant exceeds the solubility limit [4].

Very few approaches have been carried out in solving the Navier-Stokes equations in absorption processes. Hozawa et al. [6] simulated the absorption process in a stagnant pool. In a later work, Daiguji et al. [4] made a comparison between numerical and experimental results of absorption also in a stagnant pool for 1-octanol and 2-ethyl-1-hexanol taking into account the surface tension derivative measurements with respect to temperature and LiBr concentration under static conditions. Koenig et al. [7] gave numerical results also for static absorption in a thin film for different Marangoni numbers. On the other hand, Min et al. [8] applied a numerical model for the resolution of absorption processes over horizontal tubes. In that work, surface tension effects were considered, but not the effects of surface tension derivatives as in the previous reported works.

A model based on the resolution of the Navier-Stokes equations for the liquid and vapour phases was applied [5] for the resolution of absorption enhancement cases in falling film solutions produced by surfactant due to the 'salting out' mechanism, where some data of surface tension gradients are known. The free surface flow was solved in a Eulerian mesh, thus the model implemented was based on a surface capturing method. The advection of the density is computed by means of a volume of fluid technique (VOF) [9] and the surface tension forces are modelised and implemented by means of a continuum method (CSF) [10]. The pressure-velocity coupling is solved by means of the SIMPLE-like procedure [11]. The results presented in [5] were not conclusive, due to problems of instability of the numerical algorithm employed when numerical ripples are produced. In a further work [12] some additional results indicated the importance of simulating the vapour phase in the absorption process in a stagnant pool. For falling film absorption processes some demonstrative results were showed, although the CPU time required for these calculations and problems on numerical stability in some free surface configurations did not allow many numerical studies. The stability of the code has been improved and the cases presented at [12] have been completed, reporting here some additional results.

4.2 Absorption in a stagnant pool

A situation of absorption in a stagnant pool improved by surfactants has been chosen as benchmark for the comparison between numerical results and experimental data. The situation reported by Daiguji et al. at [4] (depicted in Fig. 4.1) has been reproduced. The main difference between the numerical model in [4] is that the one presented here considers as well the movements of the vapour phase, therefore it gives more information about flow configuration. However, more CPU time for computing the vapour phase is needed, due mainly to its higher sensitivity to surface tension effects because of its lower density.

The equibrium pressure of the LiBr solution placed in an adiabatic pool is lower than the one existing in the vapour, therefore the absorption of it towards the liquid phase is produced. The boundary conditions considered for the simulation of the vapour phase are zero derivative for all variables: velocities, pressure and temperature. The equation of LiBr conservation is not considered in the vapour phase, because LiBr is not volatile. In this case, the vertical velocity at the interface is considered as zero (the water velocity value at the interface is negligible), therefore no movement of the interface is considered. The thermophysical properties, geometry and conditions of the simulation are detailed in Table 4.1. It has to be indicated that a variable time increment for the transient calculation has been used in order to optimise the CPU time. The difference between the case simulated here and the one carried out by Daiguji is that the vapour phase is also considered in this study together with the
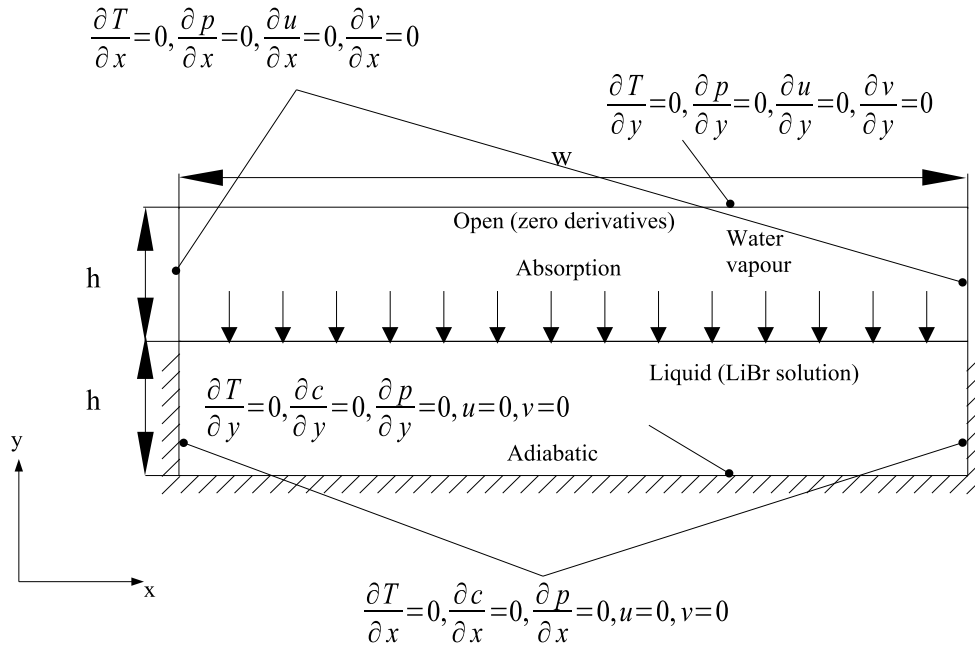
Figure 4.1: Physical domain of the pool and boundary conditions

liquid phase.

Geometric data		Thermophysical properties		
h	0.010 m	λ_1	$4.38\cdot10^{-1}$W/(m·K)	λ_2	$1.796\cdot10^{-2}$W/(m·K)
w	0.076 m	D_l	$1.43\cdot10^{-9}$m^2/s	D_v	0.0 m^2/s
Initial conditions		μ_l	$3.83\cdot10^{-3}$ Pa·s	μ_v	$9.735\cdot10^{-5}$ Pa·s
T_0	303 K	ρ_l	1624 kg/m^3	ρ_v	$1.7195\cdot10^{-2}$ kg/m^3
c_0	55.22 wt%	β_l	$3.645\cdot10^{-4}$ K^{-1}	β_v	$3.4112\cdot10^{-3}$ K^{-1}
p_0	2315 Pa	β_l^+	$-1.109\cdot10^{-1}$ wt%$^{-1}$	β_v^+	0.0 wt%$^{-1}$
		C_{pl}	2184 kJ/(kg·K)	C_{pv}	1865 kJ/(kg·K)
		σ	$6.0\cdot10^{-2}$ N/m	H_a	2568 kJ/kg
		$\partial\sigma/\partial$t	$-2.1\cdot10^{-4}$ N/(m·K)	$\partial\sigma/\partial$c	$-6.4\cdot10^{-4}$ N/(m·wt%)

Table 4.1: Thermophysical properties and initial conditions considered for the stagnant pool case

In order to generate the cellular convection, a local variation of LiBr concentration is forced at x=l/2, for τ=0.1 s. The data to be compared is the amount of water vapour absorbed as function of time. This amount of absorbed water increases until reaching a value of equilibrium. The surfactant used is n-octanol with a concentration of 25 ppm. The mesh used for the liquid phase by Daiguji is n=42 points in y-direction (concentrated towards the interface) and m=78 in x-direction (uniform). In the baseline case, the same mesh is used for the liquid and vapour phases (n_l=n_v=42, concentrated towards the interface, and m_l=m_v=78, uniform). More simulations with a coarse (n_l=n_v=21, m_l=m_v=39) and refined meshes (n_l=n_v=84, m_l=m_v=156 and n_l=n_v=168, m_l=m_v=312) have been carried out in order to find a solution closer to the numerical asymptotic one. The mesh is concentrated in y-direction towards the interface and uniform in x-direction, as in the baseline case. Fig. 4.2 shows numerical results carried out with different meshes compared with experimental data [4], and Fig. 4.3 shows the same comparison with the two most refined meshes.

The simulations carried out considering the vapour phase show better agreement with the experimental data reported by Daiguji at reference [4] than the one that only considers the liquid phase. These results reinforces the 'salting out' mechanism as explanation for the absorption enhancement when surfactant concentration is under its solubility limit and it also indicates the importance of the movements in the vapour phase in the absorption mechanism. In order to confirm that, a last simulation has been performed taking into account only the liquid, and the results obtained are quite similar to the calculated ones reported in [4], and even the mass absorbed calculated is slightly lower.

In the case of the most refined mesh (n_l=n_v=168, m_l=m_v=312) the calculation has not been completed in the whole time period because the result achieved is almost the same to the one obtained to the previous and coarse mesh (n_l=n_v=84, m_l=m_v=156) and therefore, near to the asymptotic one (Fig. 4.3). Due to its influence, the vapour phase is always considered for the calculations in falling film flow in the next section.
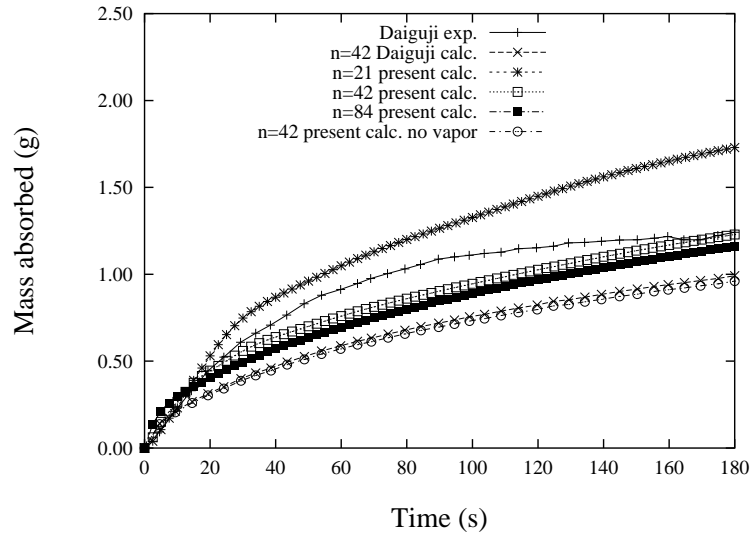
Figure 4.2: Comparison between numerical results and experimental data
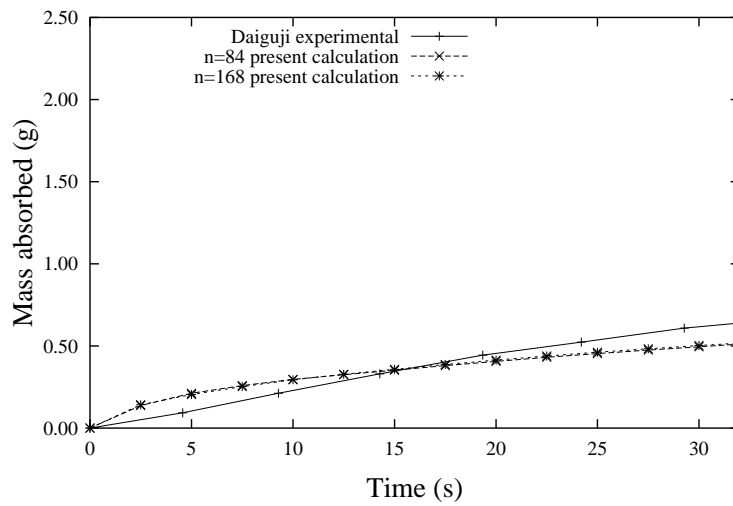
Figure 4.3: Comparison between the numerical results the two refined meshes and experimental data

Another comparison is presented between the numerical results obtained from the model and the ones reported by Daiguji at [4]. In this case, the baseline mesh (n=42) has been considered and the study has been performed for three different depths: 10, 7 and 4 mm, respectively. The results are showed in Figs. 4.4-4.6. In these cases the same conditions of calculation are maintained.

There are four results for each depth of the pool: the experimental data and numerical results reported by Daiguji [4] with 1-octanol 25 ppm, the experimental data also reported by Daiguji at [4] without surfactant and finally the numerical results obtained with vapour phase. From these, it can be observed that the results obtained by the numerical model with the vapour phase also agree better with the experiment than the results reported by Daiguji for the higher depths (10 and 7 mm). However, the agreement is lower at the lowest depth (4 mm). From a qualitative point of view, at lower values of depth the enhancement is less important. This result suggests that the mixing of water absorbed is improved when the Marangoni convection cells are more important, and those are more important when depth is higher.
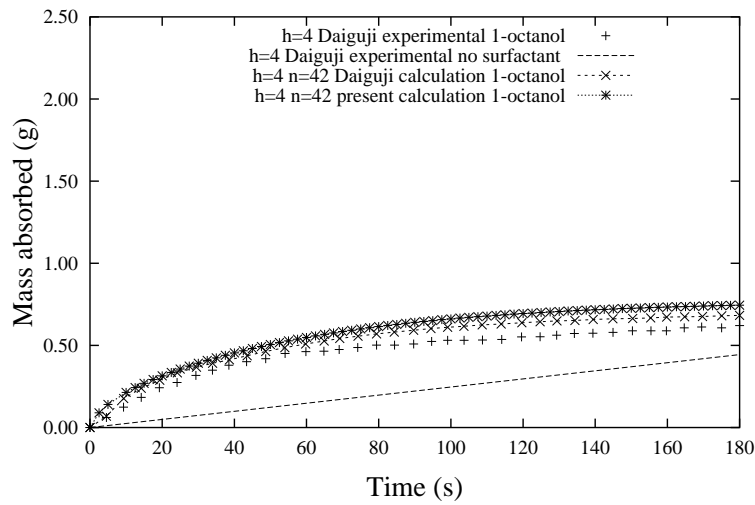
Figure 4.4: Comparison for depth h = 4 mm
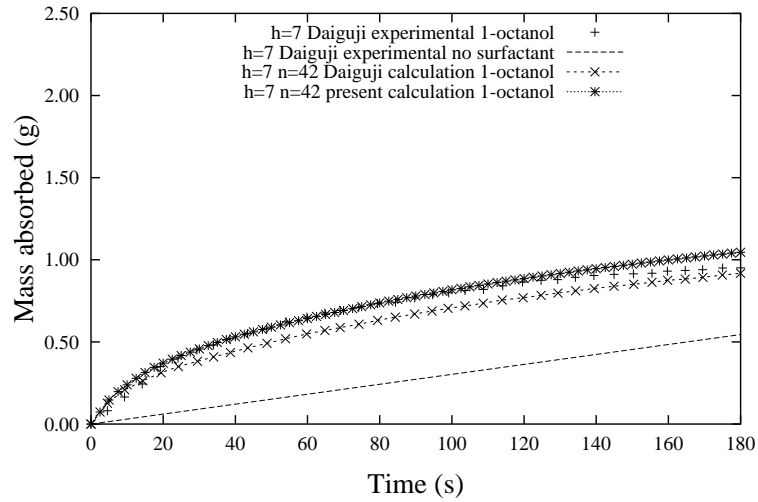
Figure 4.5: Comparison for depth h = 7 mm
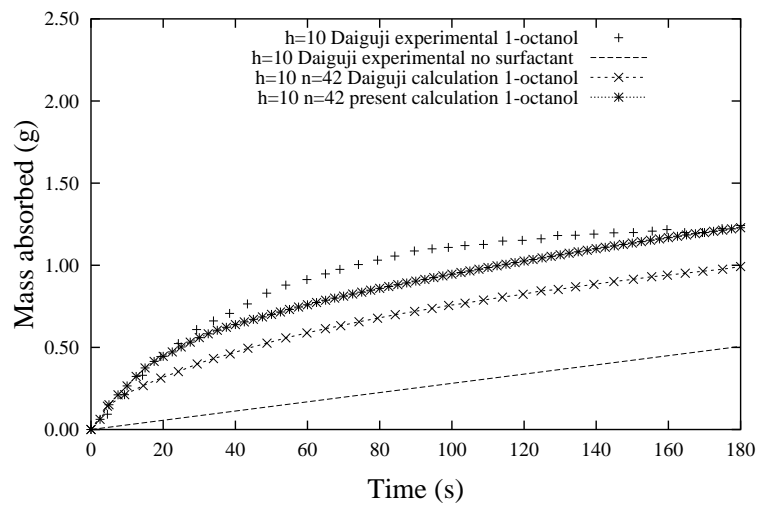
Figure 4.6: Comparison for depth h = 10 mm

A last comparison has been carried out with another well known surfactant, 2-ethyl-1-hexanol. In this case a concentration of 25 ppm has been considered. The values of $\partial\sigma/\partial T$ and $\partial\sigma/\partial c$ chosen for the calculations are respectively: -2.1·10^{-4} N/(m·K) and -1.5·10^{-3} N/(m·%w), the same than the ones reported at reference [4].

Fig. 4.7 shows a graphical comparison between the experimental and numerical values of Daiguji [4] and the present calculation. As in the previous cases, the results performed with the vapour phase agree better with the experimental data than the numerical results without vapour phase.
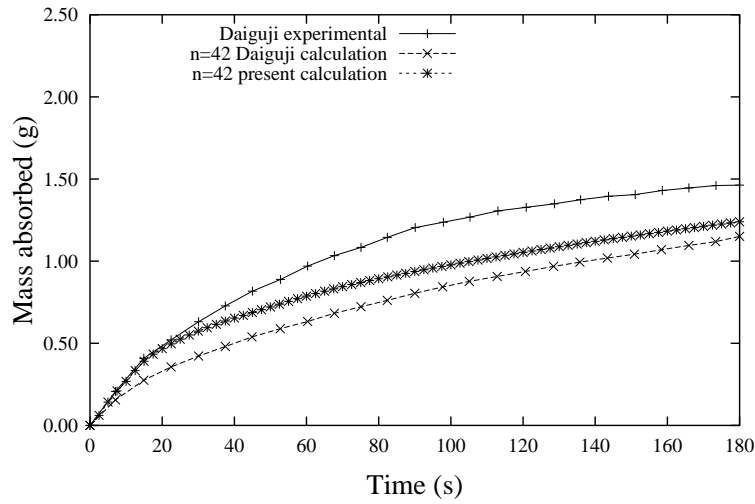
Figure 4.7: Comparison for 2-ethyl-1-hexanol (25 ppm)

Next Fig. 4.8 shows the evolution of the absorption process by means of different plots of temperatures, LiBr concentrations and streamlines, for the case of 1-octanol and 10 mm of depth (mesh used, n_l=n_v=42, concentrated towards the interface, and m_l=m_v=78, uniform). It can be observed in the streamlines that at the beginning, the movements start at the centre of the interface, where the perturbation is introduced. Then, the Marangoni cells are produced both in the liquid and vapour phase, being more pronounced in the vapour phase, due to its lower density. Finally, the last plots show the formation in the liquid phase of other cells due to gravity forces that become more important when the temperature and LiBr concentration gradients inside the liquid are significant. These movements are reflected in the plot of temperatures and concentrations: the lines are not parallel to the horizontal line, reflecting the formation of vortices in the liquid phase.
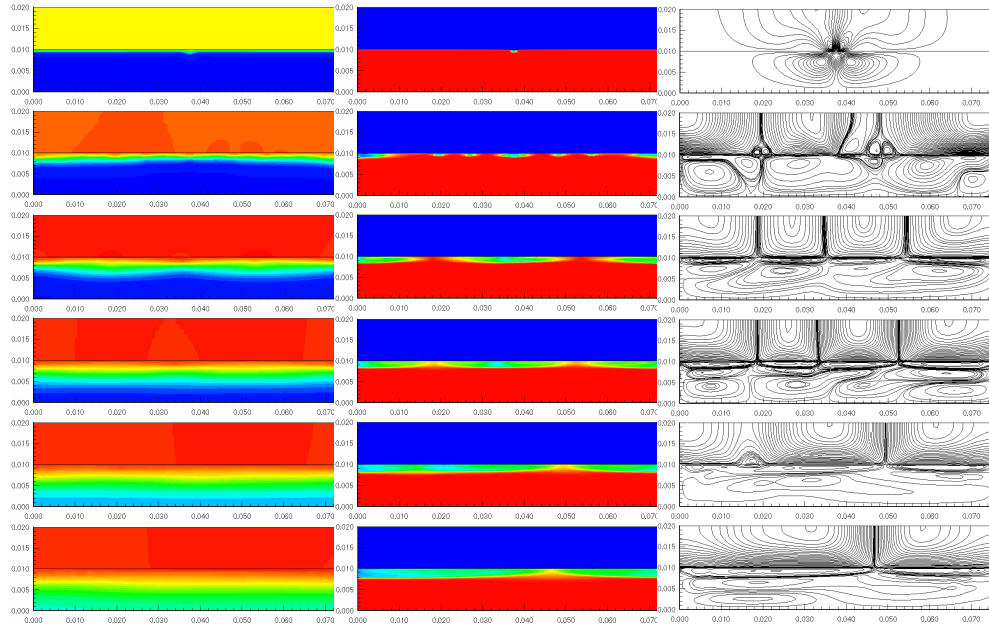
Figure 4.8: Temperatures, LiBr concentrations and streamlines at 1, 10, 30, 60, 120 and 180 seconds (from up to down)

4.3 Falling film absorption

In this section the model is employed to simulate a falling film case in a vertical wall. Although falling film absorption is a situation of industrial interest, the domain dimensions and time simulated have been limited due to the high CPU time needed for the calculations. However, if a comparison with experimental data was carried out, it has to be highlighted that it is necessary to achieve a total wetted area of the absorber surface in the experiment for all cases, in order to discard the improvements due to the enhancement of the wetted area of the heat and mass transfer surface. For this reason, not all the available information in the literature would be valid.

Fig. 4.9 shows the physical domain and the boundary conditions used for falling film absorption. The initial value of velocities corresponds to Nusselt's parabolic solution in the liquid phase. In the vapour phase a linear velocity profile is adopted. With respect to the temperature and LiBr concentration, the initial values are the same in all domain of calculation as the inlet values. At the wall, the temperature value is fixed at 38 °C. This value has been considered as realistic for air-cooled

absorbers. Although the movements in the transversal direction to the plane considered in the calculation can be important in the absorption enhancement, the simulations have been limited to two-dimensional calculation mainly to CPU time limitations. Without a comparison between two and three dimensional calculations it is difficult to evaluate the influence of these movements in transversal direction. However, the concentration and temperature gradients in the vertical direction are more important, due to the boundary conditions.
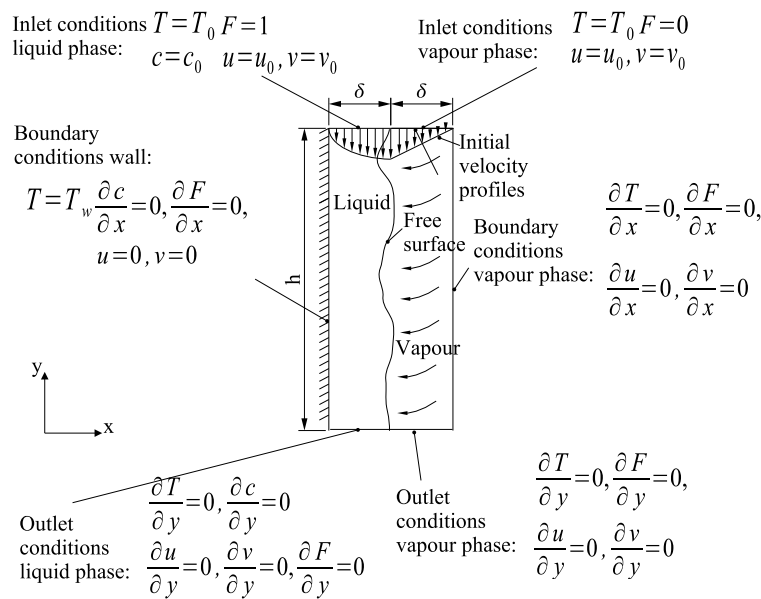
Figure 4.9: Physical domain of the falling film and boundary conditions

Table 4.2 shows the thermophysical properties, geometry employed and physical conditions of the case simulated. The value of δ corresponds to a value of mass flow about 103.5 kg/(m·h) (Re=4*Γ/μ=25), a typical value for absorption machines. The value of δ varies according to the Reynolds number.

Table 4.3 shows the values considered of surface tension and surface tension derivatives with respect to the temperature and LiBr concentration for two common surfactants used in the industry, 1-octanol (25 ppm) and 2-ethyl-1-hexanol (30 ppm). For the 1-octanol, the data considered for the calculation of the surface tension derivatives are the same as the ones used by Daiguji [4] and for the surface tension the data have been extracted from Hozawa [6]. Although in that work there are no data

Geometric data		Thermophysical properties			
h	2.0 mm	λ_l	0.438W/mK	λ_v	0.078W/mK
δ	0.24 mm	μ_l	$4.7 \cdot 10^{-3}$Pa s	μ_v	$1.0 \cdot 10^{-5}$Pa s
Conditions		D_l	$1.4 \cdot 10^{-9}$m^2/s	D_v	0
p	1138 Pa	ρ_l	1624kg/m^3	ρ_v	0.009kg/m^3
T_{in}	312.27 K	$C_{p,l}$	2200 kJ/kgK	$C_{p,v}$	1864kJ/kgK
T_w	311.15 K	β_l	$3.6 \cdot 10^{-4}$K^{-1}	β_v	$3.4 \cdot 10^{-3}$K^{-1}
c_{in}	57.00 wt%	β_l^+	-0.11wt%$^{-1}$	β_v^+	0

Table 4.2: Thermophysical properties and physical conditions considered for the falling film baseline case

shown for LiBr concentrations higher than 50%, it has been considered the minimum value of surface tension reported, due to the high LiBr concentration that favours the "salting out" effect for the 1-octanol. The data for 2-ethyl-1-hexanol have been extracted from Kim [13].

Surfactant	σ (N/m)	$\partial\sigma/\partial t$ (N/m K)	$\partial\sigma/\partial c$ (N/m w%)
no surfactant	0.080	$-1.0 \cdot 10^{-4}$	$3.8 \cdot 10^{-4}$
1-octanol (25 ppm)	0.026	$-2.1 \cdot 10^{-4}$	$-6.4 \cdot 10^{-4}$
2-ethyl-1-hexanol (30 ppm)	0.064	$7.3 \cdot 10^{-4}$	$-1.3 \cdot 10^{-3}$

Table 4.3: LiBr solution surface tension values for different surfactants

The first study presented is the comparison of the results with different meshes to see the dependence with respect to the mesh. Three different meshes have been used considering the number of cells in horizontal and vertical direction, respectively: 60x50, 120x100, 240x200 with constant mesh density in all cases. Table 4.4 contains the values of mass absorbed and heat rejected to the wall for the three different cases and the three different meshes.

There are different degrees of absorption enhancement according to the surfactant and mesh used, although the results for the two last meshes are quite similar. As a conclusion of this particular study, it results that an uniform mesh of 120x100 points is enough for assuring results roughly independent from the mesh. The heat rejected does not present significant differences between the different cases.

Fig. 4.10 shows the evolution of the mass absorbed rates during the time simulated for the different cases. The results are qualitatively similar for the three different curves compared: no surfactant, 1-octanol and 2-ethyl-1-hexanol, with a mesh of

	Mass absorbed (kg/(s·m)·10^5)			Rejected heat(W/m)		
Mesh ⟍ Surfactant	60x50	120·100	240x200	60x50	120x100	240x200
no surfactant	1.1766	1.3190	1.3020	12.201	12.233	12.329
1-octanol	1.2157	1.4529	1.4808	12.189	12.092	12.306
%enhancement	3.3	10.1	13.7	-0.1	-1.2	-0.2
2-ethyl-1-hexanol	1.2713	1.5048	1.5497	12.196	12.050	12.246
%enhancement	8.0	14.1	19.0	-0.0	-1.5	-0.7

Table 4.4: Comparison with three different meshes

120x100 points. The highest value of mass absorbed corresponds to the beginning, when the LiBr concentration, near the interface, is higher than the equilibrium one in these conditions. This fact leads to high concentration gradients that are proportional to mass absorbed rates. These absorption rates achieve a value of stability quite fast (in a period of time about $3 \cdot 10^{-2}$ s.). However, it can be observed that a completely stable value is not achieved in all cases, so the numerical results reported of mass absorbed and heat rejected are averaged values.

With respect to heat rejected (Fig. 4.11), there is not significant differences according to the surfactant used. It indicates that the interface thermal boundary layer due to the heat of absorption does not reach the wall in the distance simulated (2 mm).
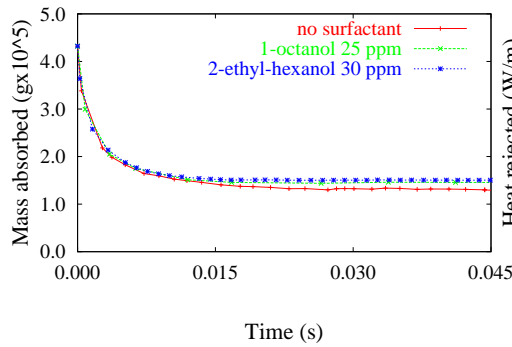
Figure 4.10: Mass absorbed vs. time
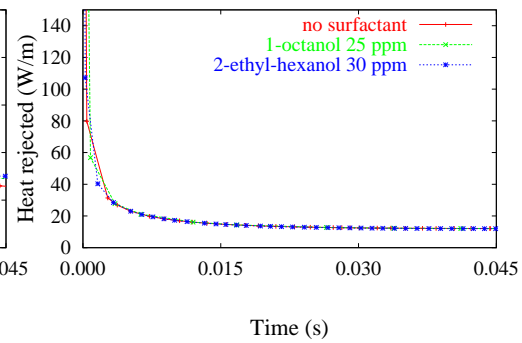
Figure 4.11: Heat rejected vs. time

In order to study the enhancement due to the action of the surfactants several parameters will be modified such as: falling film length, Reynolds number and absorption pressure (mass transfer potential).

Table 4.5 shows the comparison of the absorption improvement computed between two falling film lengths: 2 mm and 4 mm with Re = 25. It can be observed that there is a lower absorption enhancement for 4 mm than for 2 mm for the two surfactants. The boundary conditions for the temperature and LiBr concentration lead to higher gradients at the beginning of the falling film, therefore higher enhancements are expected for 2 mm than for 4 mm as the results show.

Surfactant	Length (mm)	mass absorbed $(kg/(s{\cdot}m)){\cdot}10^5$	
		2	4
no surfactant		1.3190	1.9709
1-octanol		1.4529	2.0788
%enhancement		10.1	5.5
2-ethyl-1-hexanol		1.5048	2.1202
%enhancement		14.1	7.6

Table 4.5: Enhancement according to falling film length and surfactant

Figs. 4.12 and 4.13 show the results in case of changing the Reynolds falling film number. On the left hand side, the mass of water absorbed, and on the right hand side the absorption ratio enhancement are reported for each case. The two graphics are in logarithmic scale with respect to the Reynolds number. At high Reynolds numbers, the gravity forces dominates the surface tension ones, therefore the absorption enhancement decreases with Re and finally is negligible. 2-ethyl-1-hexanol produces a significant improvement of the mass absorbed, with the maximum value of about 14 % at Re=25, the lowest Re number tested. For 1-octanol the maximum improvement of the mass absorbed is about 10% at the same Reynolds value.
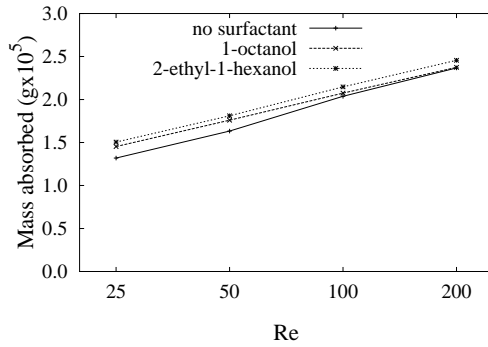
Figure 4.12: Mass absorbed vs. Re   **Figure 4.13:** Enhancement vs. Re
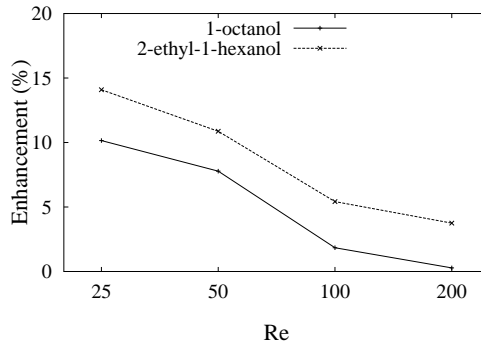
A last study has been done for comparing the enhancement produced by the two surfactants at different mass transfer driving potentials. It means that the mass absorbed has been compared at four different absorption pressures: 1051.7, 1138.7, 1225.6 and 1312.6 Pa, maintaining the rest of conditions constant with respect to previous calculations (Re=25 and 2 mm of falling film length). The vapour pressure at initial bulk temperatures (312.27 K and 57% of LiBr) was 964.8 Pa, therefore the water vapour pressure differences have been respectively: 86.9, 173.8, 260.7 and 347.6 Pa.

Figs. 4.14 and 4.15 show the numerical results obtained. On the left hand side is represented the mass of water absorbed, and on the right hand side, the absorption ratio enhancement. The computed results show that the enhancements produced are also dependent on the mass transfer driving potentials. Although in real value the absorption enhancements are increasing with the mass transfer potential, as shown in Fig. 4.14, at low pressure differences the relative absorption enhancement is more important due to the fact that the total mass absorbed rates are lower (see Fig. 4.15).
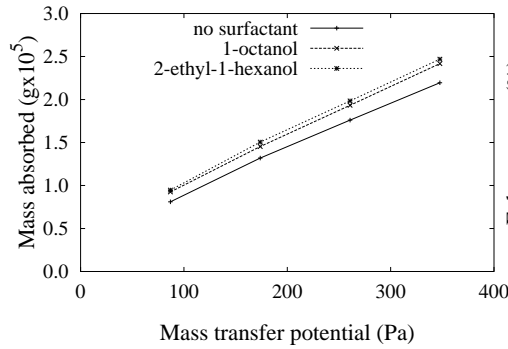
Figure 4.14: Mass absorbed vs. Mass transfer potential
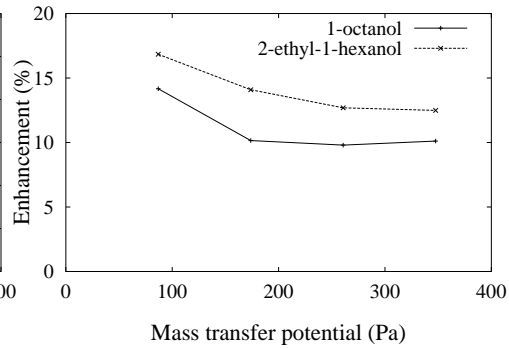
Figure 4.15: Enhancement vs. Mass transfer potential

In order to study qualitatively the influence of the two surfactants, some additional plots are shown (Figs. 4.16, 4.17 and 4.18). In these cases, the horizontal component of the velocity in the middle plane, close to the interface, is represented. This component of the velocity is a clear indicator of the movements at the interface. Three cases are plotted: no surfactant, 1-octanol (25 ppm) and 2-ethyl-1-hexanol (30 ppm). The mesh used is 120x100, with Re=25, 2 mm of falling film length and absorption pressure of 1138.7 Pa.

As expected, the case of the second surfactant, 2-ethyl-1-hexanol, presents the highest values of velocities when the mass absorbed is stabilised (t=0.045 s). However, at the beginning, the case without surfactant presents the highest values of velocities and, for 1-octanol, the movements are much lower than in the two other cases. In order to analyse the cause of the absorption enhancement for these cases, it is necessary to display the medium value of this component of the velocity (see Table 4.6) and the mass absorbed at that moment. This component of velocity favours the mass transfer at the interface, therefore the mass absorbed. The negative value of the average velocities indicates movement towards the liquid phase.

It can be observed a correlation between the absolute value of the mean velocity (towards the liquid phase) and the mass absorbed, especially for the case of 2-ethyl-1-hexanol. In this case, the movements remain almost constant for the time simulated. In the case without surfactant, the movements are much more unstable at the beginning than later, like the movements of a elastic spring (in this case the value of the surface tension is the highest). For 1-octanol, the flow is much more stable (the value of the surface tension is the lowest), and when the flow is stabilised (after 0.030 s) the mean value of the velocity always favours the absorption process.
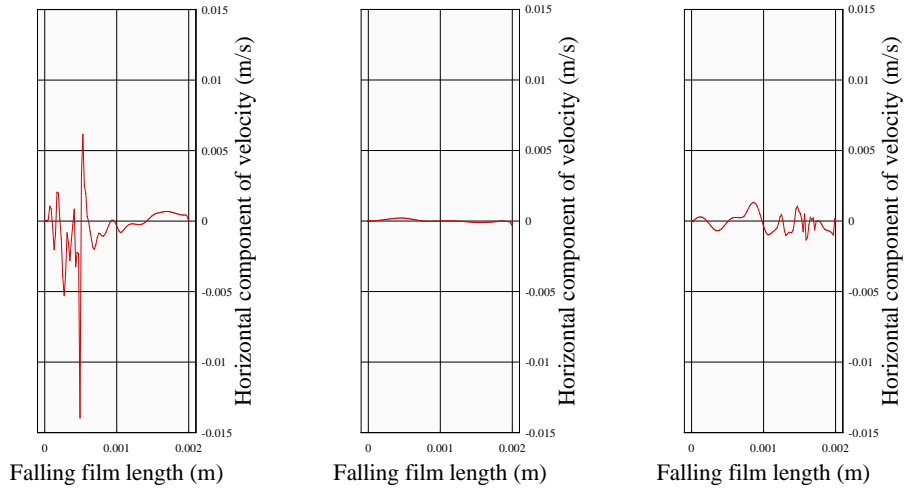
Figure 4.16: Horizontal velocities in the middle plane, corresponding to no surfactant, 1-octanol, 2-ethyl-1-hexanol (from left to right), at time 0.015
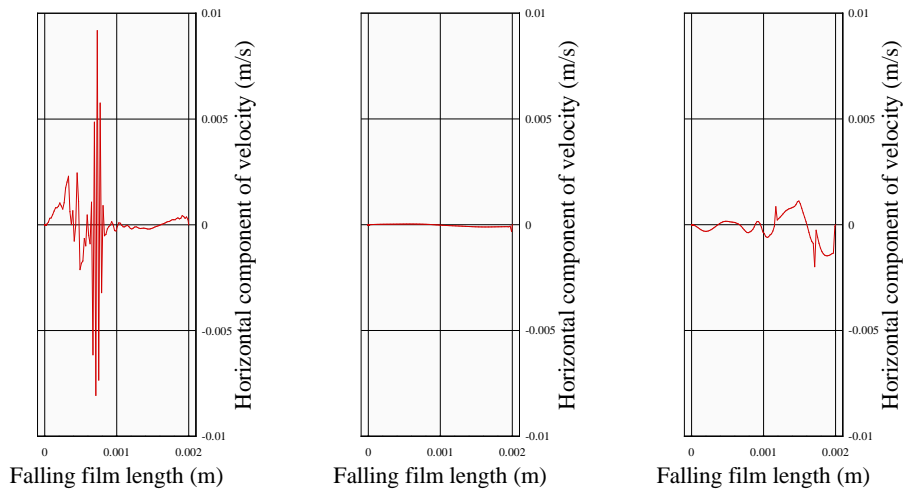
Figure 4.17: Horizontal velocities in the middle plane, corresponding to no surfactant, 1-octanol, 2-ethyl-1-hexanol (from left to right), at time 0.030
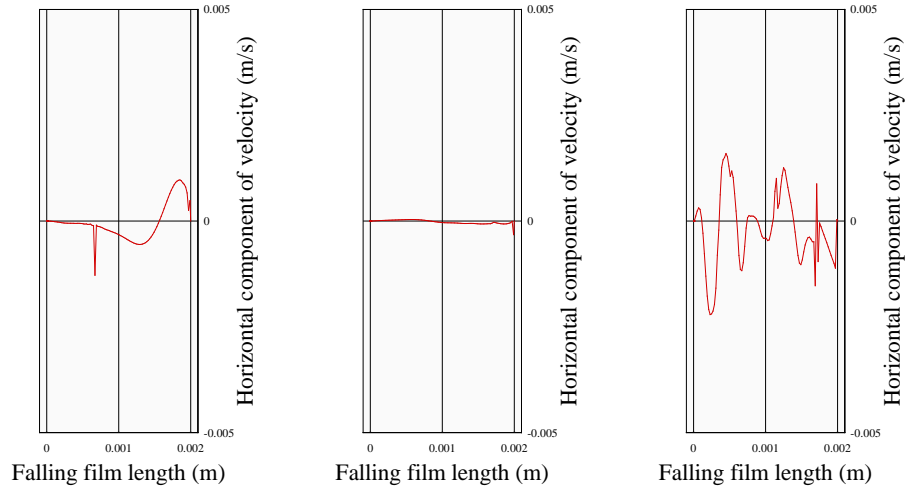
Figure 4.18: Horizontal velocities in the middle plane, corresponding to no surfactant, 1-octanol, 2-ethyl-1-hexanol (from left to right), at time 0.045

Surfactant	Result		0.015 s	0.030 s	0.045 s
no surfactant	mean velocity	$(m/s)\cdot 10^4$	-3.2850	0.6424	-0.4073
	standard deviation	$(m/s)\cdot 10^4$	19.3594	18.5918	4.2376
	mass absorbed	$(kg/(s\cdot m))\cdot 10^5$	1.4149	1.3237	1.2930
1-octanol	mean velocity	$(m/s)\cdot 10^4$	0.1496	-0.3241	-0.2180
	standard deviation	$(m/s)\cdot 10^4$	0.93050	0.60188	0.47642
	mass absorbed	$(kg/(s\cdot m))\cdot 10^5$	1.4656	1.4330	1.4534
2-ethyl-1-hexanol	mean velocity	$(m/s)\cdot 10^4$	-0.9389	-1.3151	-1.7361
	standard deviation	$(m/s)\cdot 10^4$	6.0366	6.1874	8.6013
	mass absorbed	$(kg/(s\cdot m))\cdot 10^5$	1.5215	1.5030	1.5044

Table 4.6: Average values and standard deviation of the horizontal velocity at the middle plane, and mass absorbed during three different moments: 0.015, 0.030, 0.045 s.

4.4 Conclusions

The numerical analysis of the absorption processes studied, has shown mass transfer enhancements due to the action of surface tension forces in all cases. These results are consistent with the theory of 'salting out', as Daiguji concluded at [4], that explains a mechanism of surface tension gradients with surfactant concentrations under the solubility limit. As a consequence, the absorption enhancement would be produced only for fluid (liquid and vapour) movements.

In all situations simulated 2-ethyl-1-hexanol results are slightly more efficient than 1-octanol. This fact is coherent with the general impression of the scientific community that 2-ethyl-1-hexanol is a better additive. However, it is important to highlight that it is necessary complete information about the values of surface tension of LiBr solution at different absorbent concentrations and temperatures, for different surfactant concentrations under dynamic conditions. Only with these complete data the numerical model will be able to be tested completely vs. experimental data, although it will be difficult to know if the conditions in which the surface tension is measured are equivalent to the ones produced in dynamic absorption processes. That is the reason why the results reported have to be considered as a preliminary approach.

To overcome these problems, a more detailed model would be necessary for taking into account the adsorption process of the surfactant from the liquid [14] and vapour phases [15] towards the interface and from that, computing the surface tension at each point.

The following points report the main conclusions to be highlighted from the study of the absorption in a stagnant pool and in a falling liquid film.

4.4.1 Absorption in a stagnant pool

An exhaustive comparison has been shown in a case of absorption in a stagnant pool between the results obtained with the numerical model presented in this work and the experimental and numerical results of Daiguji [4] in a previous one. From the results obtained, three main conclusions can be highlighted:

- From a quantitative point of view, the results obtained by the model, in terms of mass absorbed as function of time, present better agreement in almost all cases with the empirical results than the ones evaluated with the liquid phase only.

- From a qualitative point of view, the absorption enhancement is more important when the value of surface tension gradients are more important. This issue was observed in the study of the action of two different surfactants: 1-octanol and 2-ethyl-1-hexanol. The second surfactant (2-ethyl-1-hexanol) produces surface

tension gradients higher than 1-octanol and the pool absorbs faster the water vapour with this additive faster. Moreover, the mass absorption enhancements are improved when the depth of the pool is bigger. In those cases the Marangoni cells are more important, therefore the enhancement is higher.

- There are still significant discrepancies between empirical and numerical results. It could be explained by the fact that the simulation carried out is Cartesian 2-D, not cylindrical in three dimensions as the actual situation. Only a direct comparison with a three-dimensional simulation independent of the mesh could assure the total confidence of this model discarding other effects, like insufficient reposition of surfactant in the adsorption layer at the interface liquid- vapour that would modify the surface tension value measured under static conditions.

4.4.2 Falling film absorption

After a study of the sensitivity of results with respect to the mesh used to carry out the calculations, different simulations have been done in order to study the absorption enhancement in falling film flow under several conditions: falling film length, Reynolds number and mass transfer potential:

- Different absorption enhancement rates have been found for two different lengths of falling film. When the falling film length is increased from 2 mm to 4 mm, the rate of absorption enhancement is less important. It can be explained because at the beginning there are more important temperature and LiBr concentration gradients due to the initial boundary conditions.

- When Reynolds number increases, the gravity force dominates the falling film and the effect of the surfactants decreases. By contrary, at low Reynolds numbers, the surface tension forces are dominant and there are more important improvements of the mass absorbed. However, 2-ethyl-1-hexanol is less sensible than 1-octanol when falling film Reynolds number increases because it maintains significant enhancement ratios up to Reynolds values of 100, and 1-octanol only up to 50.

- Finally, for different values of mass transfer potential, the absorption enhancement rates are not constant. These are more important in relative terms at low mass transfer potentials, but in absolute value, the absorption enhancement increases with the mass transfer potential.

4.5   Nomenclature

c	LiBr concentration (mass fraction)
C_p	heat capacity at constant pressure
D	mass diffusivity
F	volume of fluid
h	height
H	phase change heat
p	pressure
Re	Reynolds number
T	temperature
u	velocity in x direction
v	velocity in y direction
w	width
x	coordinate
y	coordinate

Greek symbols

β	volumetric expansion coefficients due to change of temperature
β^+	volumetric expansion coefficient due to change of LiBr concentration
δ	film thickness
Γ	mass flowrate per unit length
λ	thermal conductivity
μ	dynamic viscosity
ρ	density
σ	surface tension
τ	time

Subscripts and superscripts

0	value at previous time period
a	absorption
l	liquid
v	vapour
w	wall

References

[1] W. A. Miller and H. Perez-Blanco. Vertical-tube aqueous LiBr falling film absorption using advanced surfaces. In *Proceedings of the International Absorption Heat Pump Conference*, pages 185–202, 1993.

[2] F. Ziegler and G. Grossman. Review paper: heat transfer enhancement by additives. *International Journal of Refrigeration*, 19(5):301–309, 1996.

[3] E. Hihara and T. Saito. Effect of surfactant on falling film absorption. *International Journal of Refrigeration*, 16(5):339–346, 1993.

[4] H. Daiguji, E. Hihara, and T. Saito. Mechanism of absorption enhancement by surfactant. *International Journal of Heat and Mass Transfer*, 40(8):1743–1752, 1997.

[5] J. Castro, C. Oliet, H. Schweiger, and A. Oliva. Application of a two-dimensional model for the study of water vapor absorption in fallling films of LiBr aqueous solutions with the action of a surfactant. In *Proceedings of the Fourth European Computational Fluid Dynamics Conference (ECCOMAS CFD)*, pages 286–291, 1998.

[6] M. Hozawa, M. Ionue, J. Sato, T. Tsukada, and N. Imaishi. Marangoni Convection During Steam Absorption into Aqueous LiBr Solution With Surfactant. *Journal of Chemical Engineering of Japan*, 24(2):209–214, 1991.

[7] M. S. Koenig, G. Grossman, and K. Gommed. Additive-induced enhancement of heat and mass transfer in a static absorber: a numerical study. In *Proceedings of the International Absorption Heat Pump Conference*, pages 359–366, 1999.

[8] J. K. Min and D. H. Choi. Analysis of the absorption process on a horizontal tube using Navier-Stokes equations with surface-tension effects. *International Journal of Heat and Mass Transfer*, 42(24):4567–4578, 1999.

[9] B.D. Hirt, C.W.and Nichols. Volume of fluid (VOF) method for the dynamics of free boundaries. *Journal of Computational Physics*, 39(5):201–225, 1981.

[10] A. Brandt and I. Yavneh. On multigrid solution of high-reynolds incompressible entering flows. *Journal of Computational Physics*, 101:151–164, 1992.

[11] S. V. Patankar. *Numerical Heat Transfer and Fluid Flow*. Hemisphere Publishing Corporation, 1980.

[12] J. Castro, L. Leal, M. Soria, and A. Oliva. Calculation of enhanced water vapor absorption in falling films of LiBr aqueous solutions using the domain decomposition method. In *Proceedings of the Third European Congress on Computational Methods in Applied Sciences and Engineering (ECCOMAS)*, pages 1–16, 2000.

[13] K. J. Kim, N. S. Berman, and B. D. Wood. Surface Tension of Aqueous Lithium Bromide + 2-Ethyl-1-Hexanol. *Journal of Chemical and Engineering Data*, 39(-):122–124, 1994.

[14] M. S. Koenig, G. Grossman, and K. Gommed. The Role of Surfactant Adsorption Rate in Heat and Mass Transfer Enhancement in Absorption Heat Pumps. *International Journal of Refrigeration*, 26(1):129–139, 2003.

[15] S. Kulankara and K. E. Herold. Surface Tension of Aqueous Lithium Bromide with Heat/Mass Transfer Enhancement Additives: the Effect of Additive Vapor Transport. *International Journal of Refrigeration*, 25(3):383–389, 2002.

Jesús Castro Gonzàlez, *Simulation of heat and mass transfer phenomena in the critical elements of H_2O-LiBr absorption cooling machines. Experimental validation and application to design.,* Doctoral Thesis, Universitat Politècnica de Catalunya, April 2005.

Chapter 5

Experimental validation of small air-cooled absorbers

Abstract. In order to experimentally validate the air-cooled absorber model, two different prototypes have been tested: i) the first one has a smooth surface on the solution side of the tube; ii) the second one is composed by a microfinned surface. Each heat exchanger has different tube arrangements. The different tests have been carried out under different conditions of LiBr solution mass flow, external cooling air mass flow and environmental temperature. Consequently, the tests consider different working conditions of LiBr concentration and absorption pressure. The experimental data are compared with the numerical results obtained from the model developed and implemented. The discrepancies present a reasonable quite good agreement, with most of the cases under 20% and only about 25% for few cases.

5.1　Experimental set-up description

An experimental test device has been built for testing small-scale absorbers. This device has been planned as a previous step before the construction of a complete absorption machine for its easier control and faster set-up. In this set-up several constructive solutions have been test, involving joints, fittings and liquid distributors for its later implementation in the whole absorption chiller. Fig. 5.1 shows the scheme of the experimental set-up for the small-scale air-cooled absorbers.
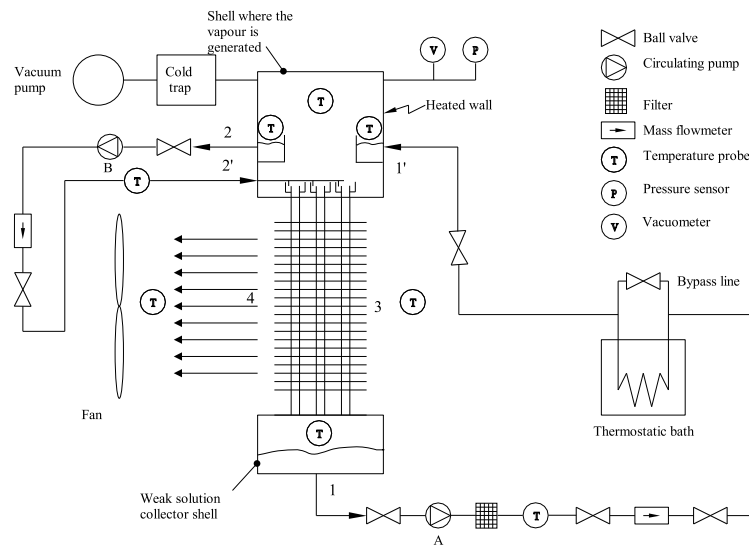
Figure 5.1: Experimental setup of the small scale air-cooled absorber scheme

The test device is composed by the following parts:

- Heat exchanger: the central part of the experimental test device is the tube-fin heat exchanger. This heat exchanger is placed in a wind tunnel where it is cooled by the action of the air moved by a variable speed fan. The upper part of the heat exchanger has special devices for the formation of falling film of LiBr aqueous solution. The weldings applied in the copper are of the phosphoric type.

- Shells: two concentric cylinders placed constitute the upper shell forming an annular pool. The part where the water vapour is produced has been separated

from the part where the vapour is absorbed. The water vapour is generated in the mentioned annular pool formed between the external cylinder, a metallic base and the internal cylinder. This configuration forces to pump the solution twice, the first time to generate the water vapour and the second time to introduce it into the absorber, thus two magnetically coupled pumps are needed. The shells are of stainless steel to avoid corrosion. Flexible heaters heat the wall of the upper shell, where the water vapour is generated. A plate made of metacrilat covers the upper shell to facilitate the observation of the falling film. The upper shell has an openning for the vacuum group and another for the pressure measurement. A seal of Viton ® connects the shells and the stainless steel plates joined to the heat exchanger. This seal has a double function: it assures no air leakages, making the absorber removable, and avoids the thermal bridge produced between the heated shell and the plates of the heat exchanger.

- Connections: the joints selected are precision fittings Gyrolok ® of the Hoke Company, in order to preserve the vacuum inside the shells.

Absorber test rig operation: starting at the lower shell, the solution is driven by a pump (A) towards the upper shell (1-1'). In this line, the mass flow, density, and temperature are measured. Before reaching the upper shell, the solution can be pre-heated or pre-cooled by a thermostatic bath. In the upper shell, the water vapour is produced by the contact of the aqueous solution with the heated walls, and consequently the solution is concentrated. This continuous production of water vapour maintains the pressure. The concentrated solution goes down to the second pump (B). This pump drives the solution again to the upper (2-2') shell and again the mass flow and density are measured. When the concentrated solution arrives to the upper shell, it is distributed between all the absorber tubes by means of a distributor. The mass flow is divided and the solution goes to a device for the falling film formation situated at the top of the tube. When the solution is diluted in the absorber, goes to the lower shell when the loop starts again.

There are additional temperature measurements: one for the water vapour in each one of the two shells, two for the liquid solution at the annular pool, and finally two for the air stream at the inlet and outlet cross section.

The measurement of the air flow is obtained by means of a hot wire anemometer taking measurements in several points of the air tunnel section (7x7 points). The measurement in each point is the result of the average of a whole of consecutive samples obtained during a period of time. Then, an spatial integration has been carried out. In order to check the results, a parallel measurement of air flow is obtained by a thermal insertion mass flow meter (FCI-ST95) with its flow homogeneizer (VORTAB). The calibration sheet performed in FCI-USA for the ST95 + VORTAB, taking into account the CTTC experimental configuration, showed an error of 0.71

% for flows from 1750 m³/h to 7000 m³/h. The discrepancies are lower than 1% is obtained between different measurements, from 0.1 to 0.8 kg/s.

If either extraction or introduction of solution is desired in the evacuated circuit (e.g. to introduce additives, to change the concentration range, to take samples) the solution is introduced into a tank. This tank is isolated from the evacuated circuit to avoid air penetrations in the shells. Fig. 5.2 shows the experimental device view. In this experiment, a rate of increment of the specific pressure of $4 \cdot 10^{-5}$ mbar·l/s has been achieved.
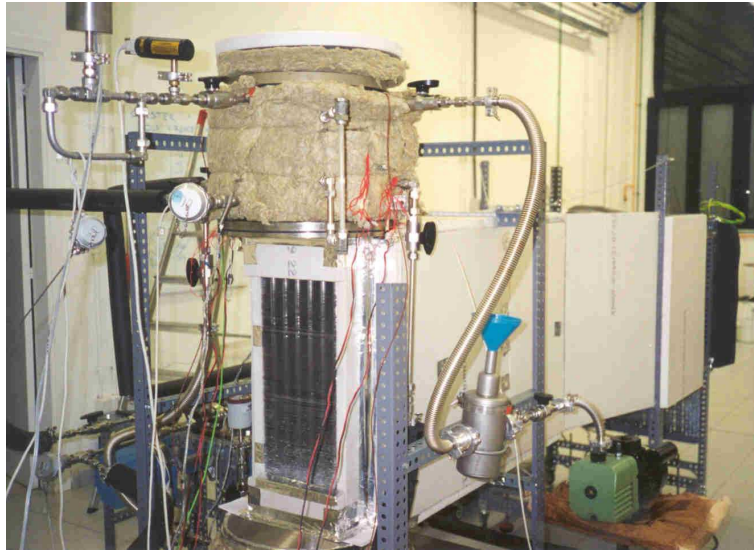
Figure 5.2: Small-scale air-cooled absorber experimental test device general view

The commercial elements of the experimental set-up are:

- 2 magnetically coupled gear pumps of variable velocity (Cole-Parmer E-74011-45), with the following characteristics:

    – Stainless steel.

    – 0.32-8.00 l/min of flow.

    – Connection to the process 1/4" NPT.

    – 230 VAC 50/60 Hz.

- Stainless steel tubes of 1/2" of outer diameter.

- Ball valves for isolating the circuit parts (Hoke rotorball 72), mostly of stainless steel.

- Precision fittings Hoke Gyrolok 1/2".

- Flexible tubes with connections iso-KF for the vacuum line.

- 1 variable speed fan (Sodeca, model HEP-56-4T/H).

- 1 turbomolecular pump (Alcatel model ATP 80 C), with the following characteristics:

  − Vacuum limit $5 \cdot 10^{-9}$ mbar.
  − Volume flow 80 l/s.

- 1 vacuum pump (Telstar model 2G-9), characteristics:

  − 9 m3/h of volume flow.
  − $8 \cdot 10^{-4}$ mbar of vacuum limit.

- 1 cold trap, Nor-cal.

- 1 line valve for vacuum line, Varian type Cv, characteristics:

  − Conductance 3.4 l/s.
  − Vacuum range: atmosphere to below 10^{-9} Torr.
  − Operating temperature: 26-150°C.

- 1 thermostatic bath Haake model N3, 3000 W of heating capacity.

The different measurement instruments employed are:

- 2 mass flow meters and densimeters (Micro Motion Elite) reference CMF025M300NB. Accuracy: ± 0.15% of reading in the mass flow and 0.0005 g/cm^3 in density with the transmitters Micro Motion Elite reference RFT9739E4EBB.

- 1 hot wire anemometer (Testo, reference 435) with an accuracy of ± 0.05 m/s for each instantaneous measurement.

- 2 absolute pressure sensors (MKS Baratron model 628B). Accuracy: ± 0.25% of reading.

- 4 temperature probes PT100, Desin Instruments. Calibrated in order to correct possible bias in the readings.

- 4 thermocouples K, Desin Instruments, also calibrated.

The temperature probes calibrationhas been carried in a thermostatic bath with refrigeration, in order to achieve a higher stability of the required temperature. A precision Platinum Resistance Thermometer (PTR) has been used as reference value, with its own data acquisition unit. The PTR system accuracy is $\pm 0.025°C$. The accuracy of the calibration system (PTR + thermostatic bath) is $\pm 0.08°C$. On the other hand, the Data Acquisition Switch Unit (DASU) used for the thermocouples has an accuracy of $\pm 0.2°C$. Therefore, the total precision of the measured temperature is less than $\pm 0.3°C$.

5.2 Experimental results and validation of the numerical model developed

The validation of the numerical model developed for the air-cooled absorber, described in Chapter 2, is explained in this section. Different tests have been carried out under different working conditions of environmental temperature, internal solution flow and external air flow.

In order to acquire confidence with the implemented model for the air-liquid heat exchangers, a battery of tests have been developed in the context of an European research project (reference CRAFT-1999-71024) in which the liquid side is single phase flow of water. The tube arrangement is the same than in one of the prototypes of air-cooled absorbed tested (the first one described in this section). In all these cases, the discrepancies between numerical and experimental results are less than 5%.

Two different air-cooled absorbers have been tested:

i) The first one consists of three rows with six expanded tubes of copper whose dimensions are: outer diameter of 16 mm, length of 700 mm (500 mm finned in the middle part), with a thickness of 0.4 mm. They are distributed in equilateral triangles of 34 mm, with the centres of the tubes located in the triangle vertexes (staggered distribution). The fin pinch is 3 mm. The inner surface of the tubes is smooth.

ii) The second one consists of four rows of nine tubes, outer diameter of 10 mm, length of 700 mm (600 mm finned in the middle part), with a thickness of 0.4 mm. They are also distributed in a staggered tube arrangement, forming equilateral triangles of 25 mm in this case. The fins are made of aluminium and also have a pinch of 3 mm. In both cases, they have a wavy geometry (herringbone wave), with a fin pattern depth of 0.8 mm, and a projected fin pattern length for one-half wave length of 8.65 mm. In this second case the inner surface of the tube is microfinned (reference Wieland, tube 95230/60/18/0.20).

5.2.1   Smooth surface absorber

Fig. 5.3 shows a general comparison between experimental data and numerical results obtained from the models developed corresponding to the heat dissipated by the first absorber (3x6 tubes of 5/8" O.D.). In the different graphics, the influence of the humidity in the results is reflected for each case. As can be observed, most of discrepancies are under 20 %. Next graphics show possible dependencies of these discrepancies to the internal solution flow or external air flow.
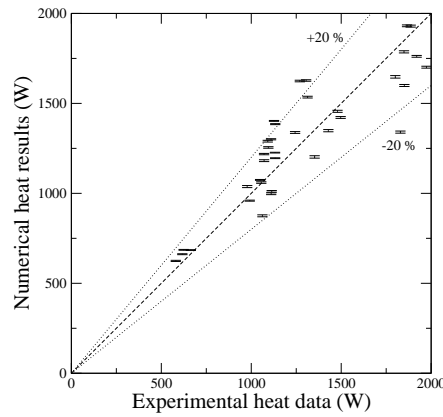
Figure 5.3: Comparison of the total heat dissipated between numerical and experimental results (smooth tube absorber)

Fig. 5.4 shows the relative discrepancy (numerical vs. experimental) depending on the external air flow. It can be observed that the experiments have been divided in four groups. The face velocities for each group are approximately 2.5, 4.0, 5.5 and 6.7 m/s, respectively. It is observed that at low air mass flows, the general trend is to slightly underestimate the experimental value of heat dissipated. By contrary, at high air mass flows the general trend is inverse.

In Fig. 5.5, these discrepancies are shown vs. the internal solution mass flow. The falling film Reynolds value varies from 25 to 80, approximately. Results show that at low values of mass flow, the numerical values of the heat dissipated are higher than the experimental ones. On the other hand, at high values of mass flow solution the discrepancy is inverse.
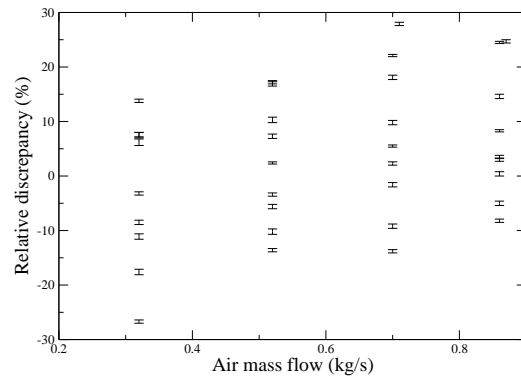
Figure 5.4: Discrepancies between numerical and experimental values for the total heat dissipated vs. air mass flow (smooth tube absorber)
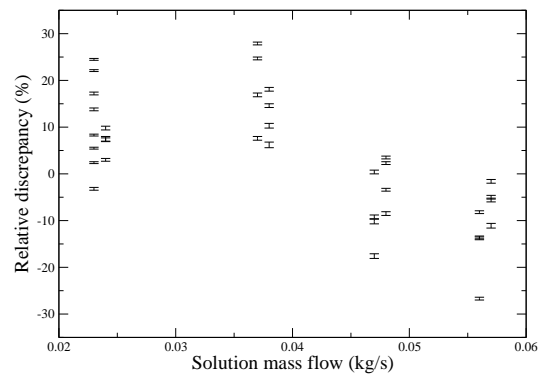
Figure 5.5: Discrepancies between numerical and experimental values for the total heat dissipated vs. solution mass flow (smooth tube absorber)

The numerical results of the heat dissipated underpredict the experimental data at high solution mass flow. This tendency can be explained due to the fact that the model used for simulating the absorption processes does not consider possible waves formed, that in general enhance the absorption process. This phenomenon is especially important at higher falling film Reynolds numbers. On the other hand, the situation is inverse at the lower falling film Reynolds numbers, as it has been commented. One possible reason could be that the model does not take into account any special velocity profile of the rivulets formed.

Fig. (5.6) show the comparison between numerical and experimental results for the fraction of latent heat due to the heat of absorption. This latent heat is calculated by the following equation:

$$Q_l = \dot{m}_{abs} \frac{(h_{v,i} - h_{s,o}) - (h_{v,o} - h_{s,i})}{ln\frac{(h_{v,i}-h_{s,o})}{(h_{v,o}-h_{s,i})}} \tag{5.1}$$
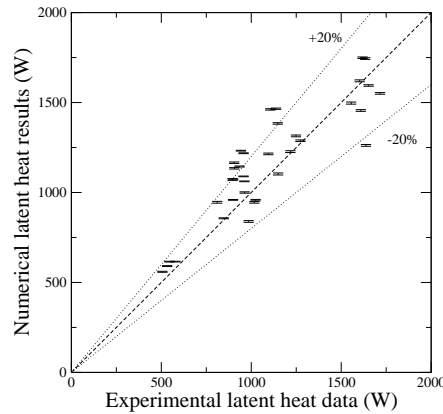
Figure 5.6: Comparison between numerical and experimental values for the latent heat (smooth tube absorber)

Equation 5.1 shows how is calculated the latent heat. It is the product between the mass absorbed of water and the enthalpy difference of the water in liquid (partial enthalpy of water at mean conditions of temperature and LiBr concentration) and vapour phases. This difference is integrated into the whole absorber using the mean

logarithmic difference. On the other hand, it has to be indicated that any change in the enthalpy of vapour has not been considered, therefore $h_{v,i} = h_{v,o}$.

As in the case of the total heat, the discrepancies of latent heat in most cases are under 20%. Another important aspect to be pointed out is that latent heat is the most important part of the total heat dissipated, around 80-90%.

As in case of the total heat dissipated, the relative discrepancy of the latent heat is shown vs. internal solution flow and external air one air (Figs. 5.7 and 5.8, respectively). The two graphics present a very similar performance compared to the previous ones which plot the total heat dissipated. In the case of the graphic of discrepancy vs. air mass flow, the numerical results also underestimates the experimental values of heat dissipated at low values of air mass flow. However, at high values the numerical reesults of the latent heat are higher than the experimental ones, although this effect is not very important. On the other hand, when the discrepancy is shown vs. the internal solution mass flow, it is observed, as in the case of the total heat dissipated, that at low values of solution mass flow, the numerical values are higher than the experimental for the latent heat and, on the contrary, the effect is inverse at high solution mass flows.
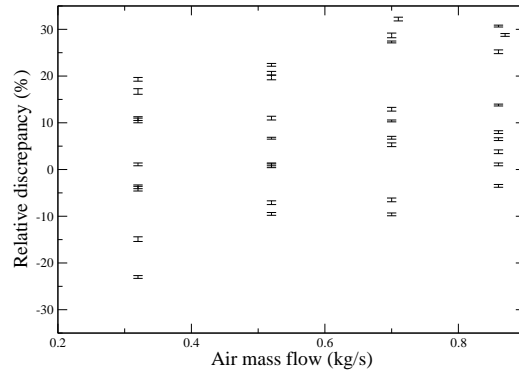
Figure 5.7: Discrepancies between numerical and experimental results for latent heat vs. air mass flow (smooth tube absorber)
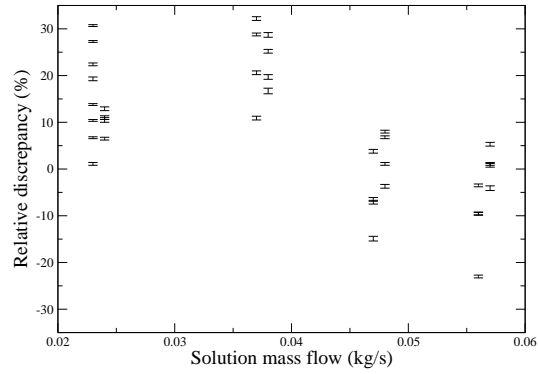
Figure 5.8: Discrepancies between numerical and experimental results for latent heat vs. solution mass flow (smooth tube absorber)

Fig. 5.9 shows the discrepancies between numerical and experimental results concerning to the sensible heat, which is calculated using the difference between the total heat dissipated and the latent heat (see equation 5.2). The values indicate that the sensible heat is much less important than the latent one. For this absorber of smooth surface tubes, the sensible heat is clearly underestimated, being the relative discrepancies very important in some cases (up to 50%).

$$Q_{se} = Q_{tot} - Q_l \tag{5.2}$$

As in the previous cases, the discrepancies between numerical and experimental values are shown vs. air mass flow (Fig. 5.10) and solution mass flow (Fig. 5.11). There is a similar dependence of the discrepancies with respect the mass flows. However, there is a bias in the values of the discrepancies. In general, it can be said that the numerical values are lower than the experimental ones for the sensible heat.

Figure 5.9: Comparison between numerical and experimental values for sensible heat (smooth tube absorber)
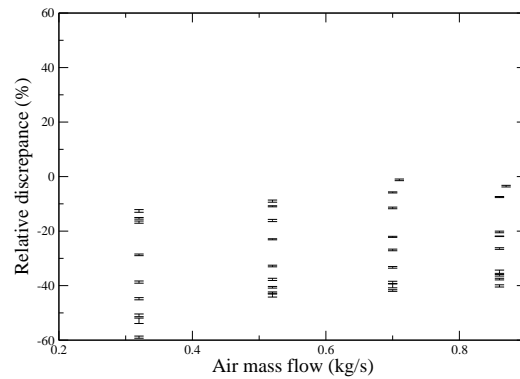
Figure 5.10: Discrepancies between numerical and experimental values for sensible heat vs. air mass flow (smooth tube absorber)
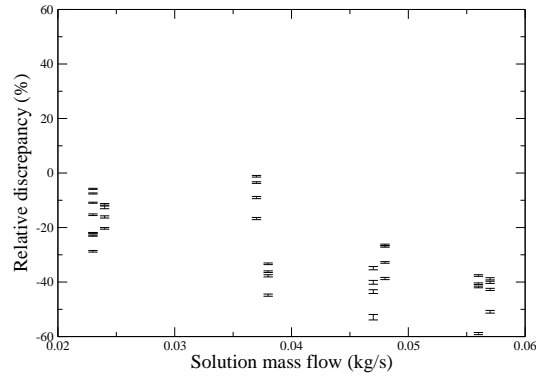
Figure 5.11: Discrepancies between numerical and experimental values for sensible heat vs. solution mass flow (smooth tube absorber)

5.2.2 Microfinned surface absorber

An analogous study has been carried out for the second absorber (4x9 tubes internally microfinned of 3/8" O.D.). Fig. 5.12 shows a general comparison between experimental measured values of the total heat dissipated and the numerical ones. In general, the level of accuracy is quite similar respect to the previous case and most discrepancies are under 20 % in all cases. The only difference is a minor general underprediction of the power dissipated. A possible reasoni is the influence of the enhanced surface, that favours heat and mass transfer, not reflected in the model based on the boundary layer hypotheses of the governing equations, that is applied in this case.

Next Fig. 5.13 shows the discrepancies between numerical and experimental results vs. air mass flow. In this case, no special dependencies are observed.

Fig. 5.14, as in the previous absorber, shows the discrepancies between numerical and experimental results vs. the internal solution mass flow. The falling film Reynolds value varies from 20 to 60 approximately. In this case, the numerical values of the heat dissipated are higher than the experimental ones at low mass flows. For high values, the discrepancy is inverse. However, this effect is much less evident.

Figure 5.12: Comparison between numerical and experimental results for the total heat dissipated (microfinned tube absorber)
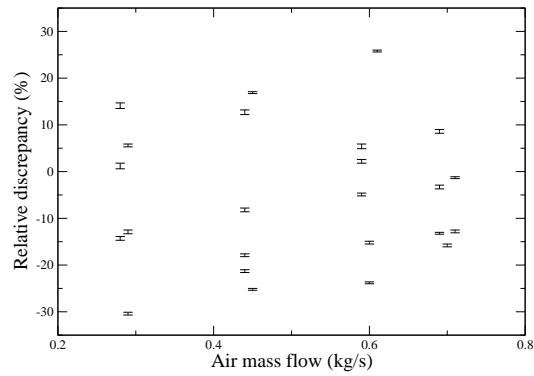
Figure 5.13: Discrepancies between numerical and experimental values for the total heat dissipated vs. air mass flow (microfinned tube absorber)
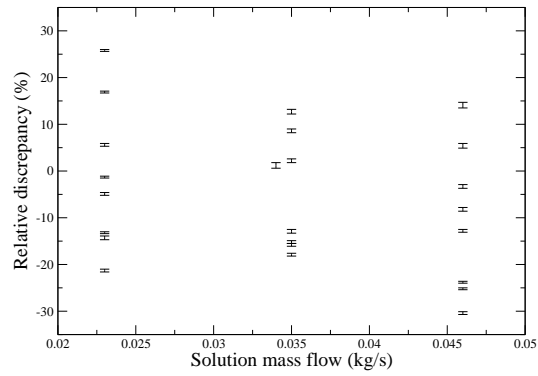
Figure 5.14: Discrepancies between numerical and experimental values for the total heat dissipated vs. solution mass flow (microfinned tube absorber)

Next Fig. 5.15 shows the numerical values of the latent heat dissipated vs. the experimental ones. As in the previous absorber, it represents the major contribution to the total heat. Analogously to the total heat dissipated, a minor underprediction of the latent heat dissipated is observed .

Figs. 5.16 and 5.17 show the discrepancies for the latent heat dissipated between numerical and experimental values plotted vs. air mass flow and solution mass flow, respectively. Apart from the already commented general observation that the numerical values are, in general, lower than the experimental ones, no special trend is observed.
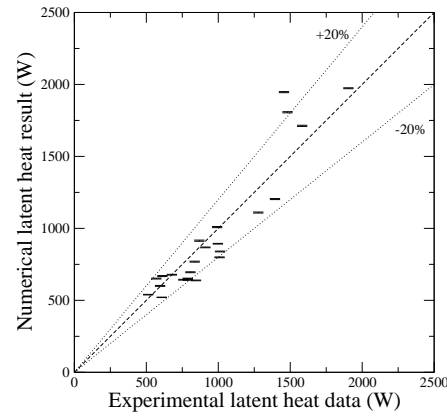
Figure 5.15: Comparison between numerical and experimental values for latent heat (microfinned tube absorber)
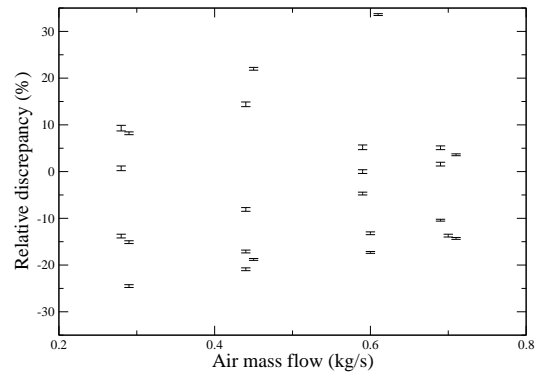
Figure 5.16: Discrepancies between numerical and experimental values for latent heat vs. air mass flow (microfinned tube absorber)
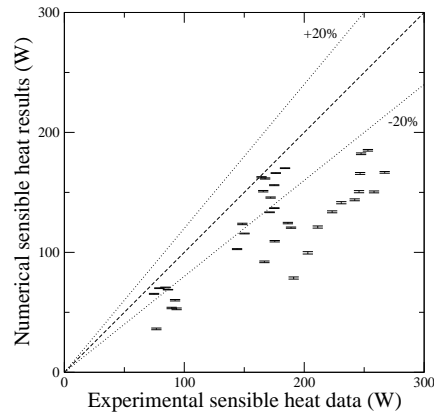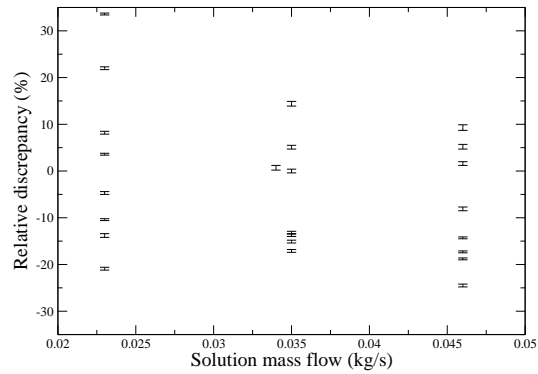
Figure 5.17: Discrepancies between numerical and experimental values for latent heat vs. solution mass flow (microfinned tube absorber)

The following Fig. 5.18 shows the comparison between numerical and experimental values depending on sensible heat dissipated. Although there is no special trend observed, it can be considered that for the lowest values the prediction is not satisfactory in general.

Finally, as in the previous cases, the discrepancies between the numerical and experimental values of the sensible heat vs. air and solution mass flow (Figs. 5.19 and 5.20). The only aspect to be pointed out is the higher dispersion of the results at higher values of solution mass flow.
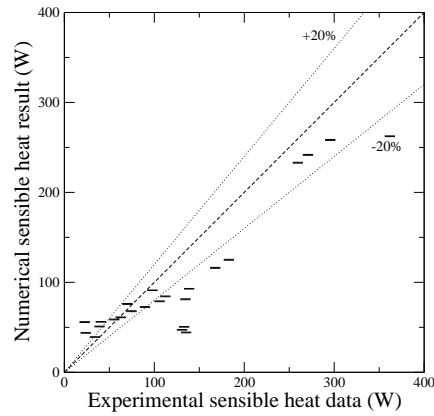
Figure 5.18: Comparison between numerical and experimental values for sensible heat (microfinned tube absorber)
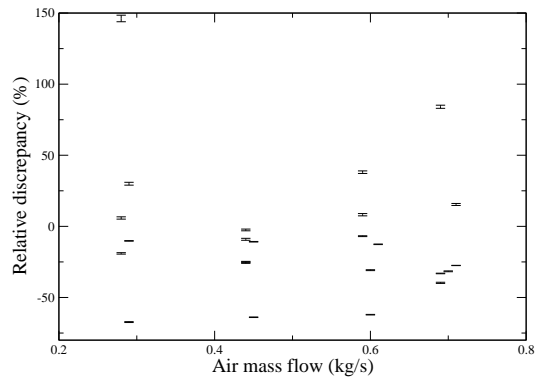
Figure 5.19: Discrepancies between numerical and experimental values for sensible heat vs. air mass flow (microfinned tube absorber)
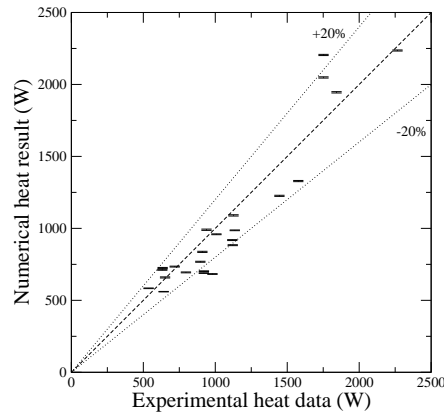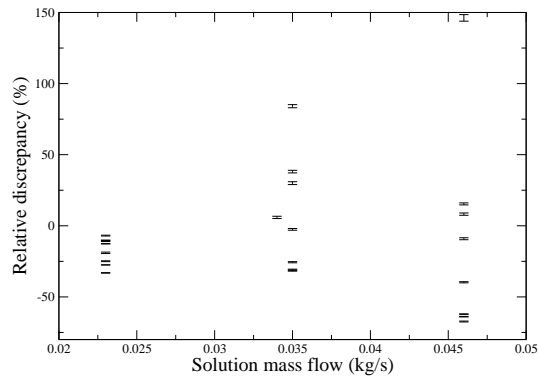
Figure 5.20: Discrepancies between numerical and experimental values for sensible heat vs. solution mass flow (microfinned tube absorber)

5.3 Tables of results

Tables 5.1 and 5.2 show the different input data and results of the different tests for the first absorber and 5.3 for the second one already show in the previous figures. It has to be highlighted that in the numerical results a relative humidity of 50 % has been considered. The input data are, by order: number of test, absorption pressure, solution mass flow, inlet solution temperature, inlet solution LiBr concentration. The results are, by order: experimental measured value of the output solution temperature, numerical result of the output solution temperature, relative discrepancy (numerical vs. experimental) of solution temperature difference respect to its experimental value, experimental data of the outlet solution LiBr concentration, numerical result of the outlet solution LiBr concentration, relative discrepancy (numerical vs. experimental) of solution LiBr concentration difference respect to its experimental value, experimental heat dissipated data, numerical heat dissipated result, relative discrepancy (numerical vs. experimental) of heat dissipated respect to experimental value.

	Solution input cond.				Air input cond.		T_1			c_1			$\dot{Q}$		
test	p	$\dot{m}_{2'}$	$T_{2'}$	$c_{2'}$	$\dot{m}_3$	T_3	exp.	calc.	%diff.	exp.	calc.	%diff.	exp.	calc.	%diff.
n^O	(Pa)	(kg/s)	($^\circ C$)	(LiBr)	(kg/s)	($^\circ C$)	($^\circ C$)	($^\circ C$)	ΔT	(LiBr)	(LiBr)	Δc	(W)	(W)	ΔQ
1	1104	0.037	43.24	0.5533	0.32	28.33	36.26	37.18	-13.2	0.5488	0.5483	10.9	1244	1338	7.6
2	1094	0.037	42.83	0.5535	0.52	28.66	35.94	36.73	-11.5	0.5485	0.5474	22.6	1313	1535	16.9
3	1075	0.037	42.42	0.5533	0.71	28.72	35.60	36.25	-9.6	0.5485	0.5467	38.2	1270	1624	27.9
4	1067	0.037	42.41	0.5533	0.87	29.16	35.45	36.14	-9.9	0.5484	0.5468	33.4	1305	1627	24.7
5	1102	0.056	46.26	0.5521	0.32	28.78	36.05	37.56	-14.8	0.5490	0.5506	-52.9	1829	1340	-26.7
6	1120	0.056	44.96	0.5521	0.52	29.16	35.96	37.42	-16.2	0.5485	0.5493	-20.4	1851	1600	-13.6
7	1108	0.056	45.26	0.5522	0.70	29.44	35.64	37.15	-15.7	0.5484	0.5492	-21.3	1974	1701	-13.8
8	1104	0.056	44.69	0.5520	0.86	29.60	35.46	36.95	-16.1	0.5482	0.5486	-10.3	1919	1762	-8.2
9	1179	0.057	47.45	0.5655	0.32	33.37	39.73	41.22	-19.3	0.5633	0.5635	-7.8	1352	1202	-11.1
10	1150	0.057	47.10	0.5655	0.52	33.64	39.25	40.60	-17.1	0.5631	0.5631	0.9	1429	1348	-5.6
11	1156	0.057	46.98	0.5655	0.70	33.95	39.20	40.54	-17.3	0.5629	0.5627	8.6	1480	1456	-1.6
12	1151	0.057	46.99	0.5654	0.86	34.57	39.18	40.51	-17.0	0.5628	0.5627	0.7	1497	1422	-5.0
13	1182	0.038	46.13	0.5653	0.32	34.16	39.45	41.04	-23.7	0.5623	0.5616	25.3	977	1038	6.2
14	1160	0.038	45.98	0.5655	0.52	34.29	39.10	40.52	-20.7	0.5621	0.5611	27.2	1071	1182	10.3
15	1156	0.038	45.80	0.5655	0.70	34.28	38.90	40.28	-20.0	0.5619	0.5605	39.4	1092	1290	18.2
16	1150	0.038	45.63	0.5655	0.86	34.84	38.77	40.24	-21.4	0.5619	0.5606	34.0	1095	1255	14.6
17	1005	0.023	42.79	0.5678	0.32	27.90	36.12	37.01	-13.4	0.5602	0.5590	16.0	1071	1218	13.8
18	970	0.023	42.26	0.5679	0.52	28.20	35.48	36.20	-10.6	0.5599	0.5584	19.0	1110	1300	17.2
19	939	0.023	41.85	0.5678	0.70	27.76	34.91	35.43	-7.5	0.5598	0.5578	24.1	1134	1385	22.2
20	932	0.023	41.43	0.5677	0.86	27.94	34.58	35.22	-9.3	0.5597	0.5574	27.6	1127	1403	24.5
21	1084	0.048	46.54	0.5664	0.32	28.49	37.93	39.23	-15.1	0.5614	0.5619	-10.4	1801	1648	-8.5
22	1026	0.048	45.91	0.5662	0.52	28.86	36.93	38.07	-12.7	0.5611	0.5613	-3.8	1849	1786	-3.4
23	988	0.048	45.35	0.5661	0.70	28.48	36.21	37.22	-11.0	0.5609	0.5607	4.1	1886	1930	2.3
24	950	0.048	44.89	0.5658	0.86	28.46	35.53	36.52	-10.6	0.5608	0.5605	6.2	1866	1931	3.5

Table 5.1: Results for the 5/8" tube absorber with smooth surface tube

	Solution input cond.				Air input cond.		T_1			c_1			$\dot{Q}$		
test	p	$\dot{m}_{2'}$	$T_{2'}$	$c_{2'}$	$\dot{m}_3$	T_3	exp.	calc.	%diff.	exp.	calc.	%diff.	exp.	calc.	%diff.
nᴼ	(Pa)	(kg/s)	($^\circ C$)	(LiBr)	(kg/s)	($^\circ C$)	($^\circ C$)	($^\circ C$)	ΔT	(LiBr)	(LiBr)	Δc	(W)	(W)	ΔQ
25	1188	0.047	47.67	0.5629	0.32	35.62	40.38	41.30	-12.6	0.5609	0.5616	-33.6	1062	875	-17.6
26	1175	0.047	47.42	0.5626	0.52	35.76	39.95	40.88	-12.4	0.5604	0.5608	-16.0	1111	998	-10.2
27	1165	0.047	47.28	0.5623	0.70	36.12	39.80	40.67	-11.7	0.5602	0.5605	-15.0	1114	1011	-9.2
28	1182	0.047	47.42	0.5619	0.86	36.37	39.89	40.76	-11.6	0.5600	0.5598	9.2	1056	1060	0.4
29	1206	0.024	44.44	0.5627	0.32	36.29	40.06	40.87	-18.4	0.5590	0.5585	12.6	581	625	7.6
30	1206	0.024	44.37	0.5630	0.52	36.84	39.93	40.81	-19.9	0.5589	0.5584	12.2	617	662	7.3
31	1188	0.024	44.57	0.5629	0.70	36.79	39.74	40.50	-15.7	0.5589	0.5583	15.0	624	686	9.9
32	1199	0.024	44.89	0.5631	0.86	37.25	39.81	40.72	-17.9	0.5589	0.5586	6.3	664	685	3.1
33	864	0.023	41.00	0.5648	0.32	27.52	33.42	34.69	-16.8	0.5584	0.5586	-3.8	991	959	-3.2
34	852	0.023	41.12	0.5651	0.52	27.62	33.14	34.22	-13.6	0.5583	0.5581	2.5	1049	1075	2.4
35	860	0.023	41.11	0.5657	0.70	27.52	33.01	34.14	-13.9	0.5581	0.5576	6.4	1133	1196	5.5
36	846	0.023	40.92	0.5656	0.86	27.41	32.62	33.78	-13.9	0.5581	0.5573	10.4	1132	1226	8.3

Table 5.2: Results for the 5/8" tube absorber with smooth surface tube (continued)

test	p	$\dot{m}_{2'}$	$T_{2'}$	$c_{2'}$	$\dot{m}_3$	T_3	exp.	calc.	%diff.	exp.	calc.	%diff.	exp.	calc.	%diff.
								T_1			c_1			$\dot{Q}$	
n^O	(Pa)	(kg/s)	($^\circ C$)	(LiBr)	(kg/s)	($^\circ C$)	($^\circ C$)	($^\circ C$)	ΔT	(LiBr)	(LiBr)	Δc	(W)	(W)	ΔQ
1	1150	0.023	41.80	0.5465	0.29	20.57	33.09	33.41	-3.7	0.5351	0.5324	23.5	1843	1945	5.6
2	1150	0.023	41.66	0.5450	0.45	22.18	32.52	32.96	-4.8	0.5346	0.5303	41.5	1752	2048	16.9
3	1146	0.023	41.50	0.5442	0.61	22.54	31.95	32.57	-6.5	0.5344	0.5288	56.9	1752	2205	25.8
4	1107	0.023	40.89	0.5434	0.71	22.16	30.07	31.72	-15.3	0.5301	0.5278	17.2	2266	2236	-1.3
5	1200	0.023	41.63	0.5370	0.28	30.70	35.53	35.76	-3.8	0.5324	0.5327	-5.7	896	768	-14.3
6	1178	0.023	41.63	0.5367	0.44	30.49	34.92	35.11	-2.9	0.5305	0.5316	-17.2	1122	883	-21.2
7	1164	0.023	41.46	0.5351	0.59	30.12	34.57	34.49	1.2	0.5300	0.5296	7.4	1008	959	-4.8
8	1183	0.023	41.60	0.5336	0.69	30.24	33.87	34.45	-7.4	0.5278	0.5279	-2.1	1136	986	-13.1
9	1203	0.034	38.99	0.5300	0.28	31.31	34.92	35.37	-11.0	0.5283	0.5277	33.3	652	659	1.2
10	1201	0.035	39.08	0.5286	0.44	31.65	34.51	35.04	-11.6	0.5272	0.5262	72.5	632	712	12.8
11	1187	0.035	39.64	0.5281	0.59	31.78	34.53	34.78	-4.8	0.5265	0.5259	35.0	718	734	2.2
12	1167	0.035	38.48	0.5272	0.69	32.34	34.22	34.54	-7.5	0.5261	0.5255	66.1	537	583	8.7
13	1101	0.046	38.56	0.5333	0.28	30.32	34.39	34.65	-6.2	0.5325	0.5317	98.3	634	724	14.2
14	1104	0.046	38.79	0.5335	0.44	30.77	34.09	34.59	-10.6	0.5318	0.5315	15.8	910	837	-8.1
15	1204	0.046	40.67	0.5320	0.59	31.82	35.28	35.65	-6.8	0.5305	0.5297	51.6	939	990	5.5
16	1202	0.046	41.15	0.5316	0.69	31.59	34.61	35.47	-13.2	0.5299	0.5292	38.1	1127	1090	-3.3
17	937	0.035	37.42	0.5333	0.29	27.46	27.28	28.58	-12.8	0.5279	0.5283	-7.1	980	683	-30.4
18	980	0.035	38.15	0.5331	0.44	27.67	26.42	27.67	-10.7	0.5276	0.5277	-2.5	921	689	-25.1
19	1077	0.035	39.68	0.5339	0.60	28.27	26.08	27.32	-9.1	0.5274	0.5274	-1.3	921	703	-23.7
20	1134	0.035	40.45	0.5327	0.70	28.79	26.73	27.25	-3.8	0.5271	0.5270	1.8	642	560	-12.7
21	937	0.035	37.42	0.5333	0.29	27.46	31.59	31.76	-2.9	0.5315	0.5316	-5.3	796	694	-12.8
22	980	0.035	38.15	0.5331	0.44	27.67	31.64	32.08	-6.8	0.5299	0.5303	-11.7	1118	918	-17.9
23	1077	0.035	39.68	0.5339	0.60	28.27	32.76	33.28	-7.6	0.5291	0.5294	-5.6	1446	1226	-15.2
24	1134	0.035	40.45	0.5327	0.70	28.79	33.28	33.81	-7.5	0.5274	0.5278	-6.7	1577	1329	-15.7

Table 5.3: Results for the 3/8" tube absorber with microfinned surface tube

5.4 Conclusions

Two H$_2$O-LiBr air-cooled absorber prototypes have been tested to validate the numerical model implemented. From the numerical and experimental results obtained, the following conclusions are highlighted:

- A mathematical model has been developed to simulate air-cooled absorbers, with discrepancies in the calculation of the heat dissipated under 20% in most cases with less accurate predictions of the changes in temperature and concentration in the solution stream, due to the difference between the two-dimensional velocity field considered in the falling film calculation, and the real three-dimensional one of the rivulets produced in the incomplete wetted area of the tube.

- The presence of a microfinned surface, only produces a minor enhancement of the performance of the absorber.

- For all the tested cases the latent heat of absorption has been much more important than the sensible one (about 80-90% of the total).

- The value of the latent heat dissipated is much better predicted that the value of sensible heat.

- There is no clear dependence of the discrepancies between numerical and experimental values vs. the external and internal mass flows. The only common aspect is that at the highest values of solution mass flow, the model underpredicts the value of the heat dissipated. It can be explained that the falling liquid film model does not consider possible waves formed, waves that in general enhance the absorption process.

- Problems have been detected in the solution distributors due to an irregular distribution of the flow. This incorrect distribution is the responsible in part of the discrepancies between the actual behaviour of the air-cooled absorbers and the predicted results of the mathematical model.

5.5 Nomenclature

c	LiBr concentration
$\dot{Q}$	heat power
$\dot{m}$	mass flow
p	pressure
T	temperature

Subscripts and superscripts

a	absorption
ab	absorber
air	air (secondary stream)
cl	calculation
ex	experimental
i	input
l	latent
o	output
s	solution
se	sensible

Chapter 6

Air-cooled H$_2$O-LiBr absorption machine

Abstract. The experimental device that constitutes the absorption chiller is described. The different elements are shown, its geometry reported, and the general performing is explained. Before the construction of the whole absorption machine, the falling film distribution system for the serpentine heat exchangers has been tested to study the wetted area achieved. A minimum mass flow to assure a total wetted area has been found experimentally. Finally, the procedure of construction and the general protocol of set-up are also described.

123

6.1   Description

Fig. 6.1 shows the experimental prototype scheme with its different circuits, while Fig. 6.2 depicts a general view. The device consists of: two shells (one situated at the top and the other at the bottom) and two air-cooled heat exchangers in the middle (the absorber and condenser). These elements are in series. Thus, inlet air conditions at the condenser correspond to the outlet air conditions at the absorber (point 17 = point 16). The two shells are divided in two parts, according to both pressure levels of the absorption cycle. To deal with a wide range of working conditions, this prototype has two extra pumps with respect to the standard single effect cycle. The first pump is added to the circuit in order to work under a wide range of mass flow refrigerant depending on pump conditons (see points 10'-11 in Fig. 6.1). The second extra pump is situated to circulate solution from the generator to the absorber (points 23-24). This pump would not be necessary in case of absence of measuring elements, i.e. mass flow meters which produce additional pressure drops in the line. Therefore, the solution expansion valve is not necessary (5'=6).

There are also extra lines to be used in de-crystallisation mode. On the one hand, a valve (v1) is opened and activates the bypass line between the generator and absorber in case the normal line between them through the solution heat exchanger is obstructed due to crystallisation. On the other hand, a second valve (v2) is also opened, and the connection line between the refrigerant circuit and the strong solution is activated to dilute the crystals.

The machine performs as follows (see Fig. 6.1): starting from the absorber, the strong solution absorbs water vapour in the air-cooled tubes of the absorber. Then, the weak solution is collected in the lower shell (point 1), where its temperature is measured and pumped to the generator (1'-2). On its way to the generator, the solution passes through a filter and a mass flow meter where the mass flow and density are measured (considering the measurement of density and temperature, the LiBr concentration is then deduced) by a Coriolis mass flow meter. Before reaching the generator, the weak solution is preheated in the solution heat exchanger (2'-3). The temperature is also measured before it reaches the solution heat exchanger (2') and the generator (3'), where the solution goes through the generator distributor and wets the horizontal tube generator. The strong solution is collected in a plate inside the upper shell (4) and then the temperature is measured before being pre-cooled in the solution heat exchanger (4'). The water vapour generated goes through a drop separator in order to avoid presence of LiBr in the refrigerant circuit. The temperature of the strong solution is also measured after passing across the solution heat exchanger (5). After that, the solution is pumped by an additional pump (23-24) and again the mass flow and density are measured. Finally, the strong solution reaches the absorber distributor (6') where it is equally distributed between the vertical tubes. On the other hand, the water vapour obtained in the generator (7') condenses in the

condenser being collected at the other side of the lower shell (8). The condensed water is expanded in the expansion valve (8'-9) and goes to a liquid separator (9'). Then, it is pumped to the evaporator distributor (11- 11') and wets the falling film evaporator. The vapour generated (13-13') is absorbed in the air-cooled absorber and the rest of the liquid returns to the liquid separator (12-12'). There is also an extra line for taking samples to a mass spectrometer to measure the presence of incondensables and other undesirable species during the performing of the unit.

Under working conditions, the machine is placed in a wind tunnel where the measurement of the air-flow is carried out by means of a hot wire anemometer. A matrix of measurement points has been taken (7 in horizontal direction, 11 in vertical direction) uniformly distributed. Each measurement has been averaged in time.

Figure 6.1: Absorption machine experimental device scheme
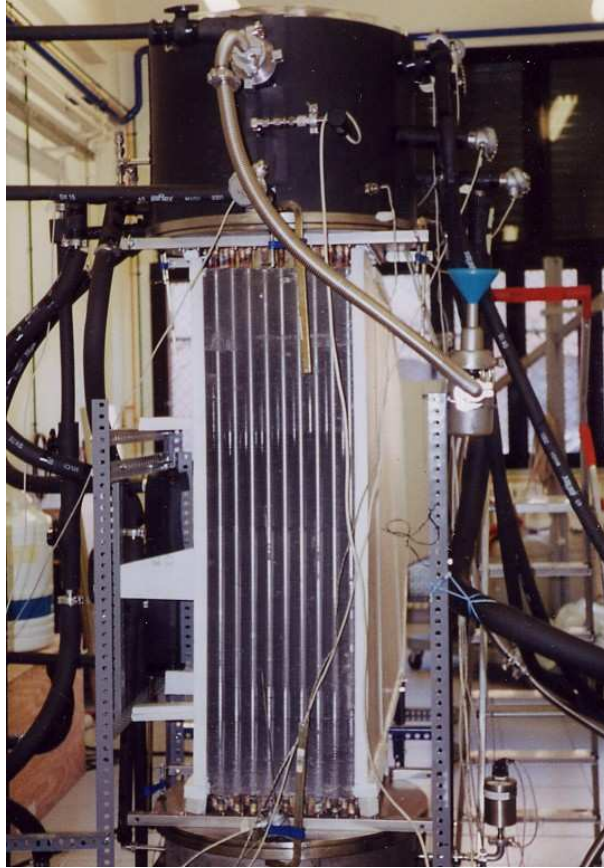
Figure 6.2: Air-cooled absorption machine general view

Details of the different heat exchangers are presented in this chapter. All the heat exchange surfaces are smooth. The copper tubes that compose the absorber and condenser have the following dimensions: external diameter of 16 mm, length of 1300 mm (1200 mm finned in the middle part), with a thickness of 0.4 mm. Their arrangement is staggered, with a tube distance in the air flow direction (y) of 33 mm, and a tube spacing in the normal direction to the air flow (z) of 38 mm (see Fig. 6.7). The fins are of aluminium and have a thickness of 0.12 mm, with a length in y and z direction, respectively, of 136 mm and 341 mm. A herringbone fin wave, with a semi-longitude of fin wave of 8.65 mm and a fin angle of 8 degrees has been used. Fig.

6.7 shows the air-cooled condenser and the absorber. These air-cooled components are joined to the stainless steel plates by means of o-ring joints. Both heat exchangers consist of 36 tubes (four tubes in y direction and nine tubes in z direction). The only difference is the fin pitch, with 2 mm for the absorber and 3 mm for the condenser.

The generator and the evaporator are batteries of horizontal smooth tubes made of stainless steel of 12.7 mm of external diameter, 0.89 mm thick, and 300 mm of useful length. Their arrangement is inline, and the tube distance in horizontal and vertical direction is 25.4 mm and 15.7 mm, respectively. Fig. 6.3 shows the evaporator and generator inside one shell of the chiller. The generator consists of 96 tubes (sixteen tubes in vertical direction and six tubes in horizontal direction), and the evaporator of 48 tubes (twelve tubes in vertical direction and four tubes in horizontal direction).

Figure 6.3: Upper shell with the serpentine heat exchangers: evaporator and generator

In order to achieve a high flexibility, different o-ring joints and fittings have been used. Special care has been taken into account to purge incondensables (once before each one-day test). Their concentration is measured by means of a quadrupole mass spectrometer. The chiller has been tested under different environmental conditions. In order to achieve repeatability of results, each stream is regulated by variable flow
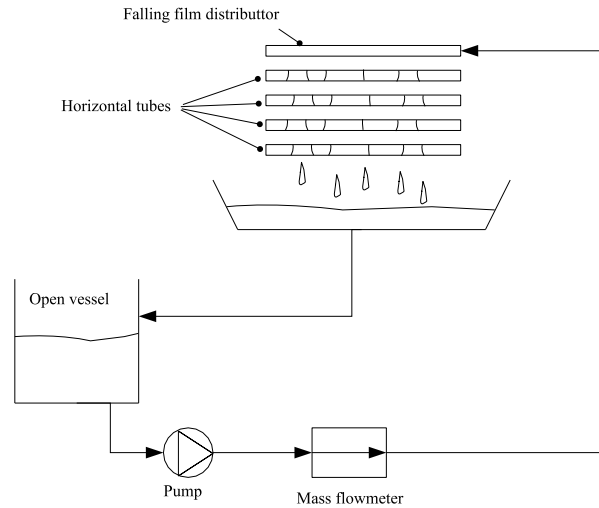
Figure 6.4: Scheme of the testing system serpentine heat exchangers falling film distributors

pumps. In the first tests, it was detected presence of LiBr in the refrigerant circuit, with the consequent reduction of the evaporator performance. The reason was the inefficient performance of the drop separator at the generator. This issue has been completely solved in the present set-up.

Under working conditions, the machine is placed in a wind tunnel to achieve an uniform distribution of the air mass flow, which is measured by means of a hot wire anemometer. The temperature of the hot water and chilled water streams are controlled by means of thermostatic baths.

6.2 Tests of falling film distributors of the serpentine heat exchangers

For an adequate design of the falling film distributors of serpentine generator and evaporator, the falling film formation in these heat exchangers has been studied . The system is based on a distributor of the liquid mass flow for every column of horizontal tubes (see Fig. 6.4, scheme and Fig. 6.5, view). This liquid is introduced to a falling film formation device. Several conclusions have been extracted from tests performed:
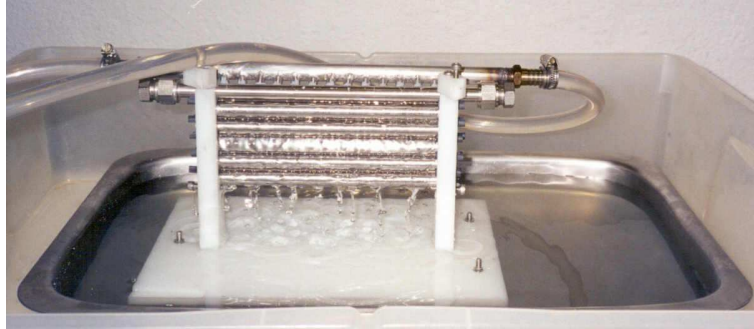
Figure 6.5: Study of the falling film distribution system of serpentine heat exchangers

- In order to achieve an acceptable wetted area a falling film formation device based on a slotted tube to form a plane jet has performed better than several discrete points of distribution.

- The wetted area is maintained even for columns of several horizontal tubes considering a short distance between them (about 3 mm for the geometry studied of 1/2 " tube of outer diameter).

- However, without any surfactant or any special device to increase the wetted area, a total wettability of the tubes with a mass flow of 500 kg/(m·h) of water over each side of the stainless steel tubes has been observed. It corresponds to a dimensionless falling film thickness of about 0.83. The Hobler criterion [1], equation (2.47), establishes a minimum value of 0.817 (with the correction for round tubes suggested in [2]). This value results too high for being maintained by the solution pump at the generator and the refrigerant pump at the evaporator. In order to maintain a similar area wetted between tubes a thread bar between tubes had to be introduced.

6.3   Construction of the absorption chiller

The process of construction of the absorption chiller has been divided in several steps according to the parts of the machine:

- Construction of the shells (Figs. 6.3 and 6.6). These shells are made of a folded plate of stainless steel, that was welded to form the cylinders. Then, the stainless

steel rings that allocate the joints that connect the shell with the plates of the heat exchangers were welded. Finally, several holes were made for the probes and tube connections.

Figure 6.6: Lower shell

- Construction of the air-cooled heat exchangers (absorber and condenser, Fig. 6.7). The first step was the construction of the batteries of finned tubes. After that, the construction of the stainless steel plates, brass connections between plates and batteries, and falling film distributors. The brass connections were welded to the finned tubes batteries, and finally, they were connected to the plates. This type of constructive solution was already proved with the small air-cooled absorbers (see Chapter 5).

Figure 6.7: Tube-fin heat exchangers (absorber and condenser

- Construction of the internal stainless steel plates (Fig. 6.8).
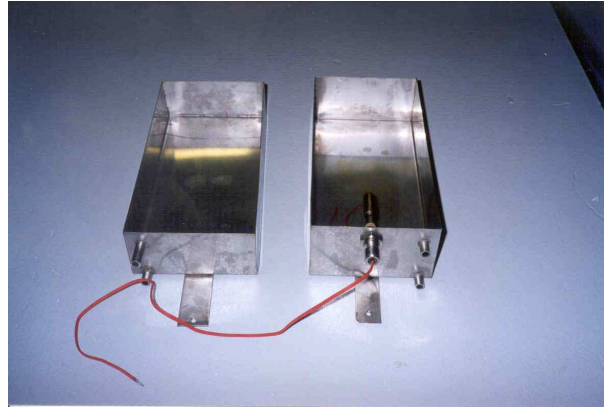
Figure 6.8: Internal plates

- Construction of the serpentine heat exchangers (generator and evaporator): cutting of the stainless steel pieces (tubes, bars ...) and welding (thread bars, liquid collectors) to form the whole heat exchangers (see Fig. 6.9).
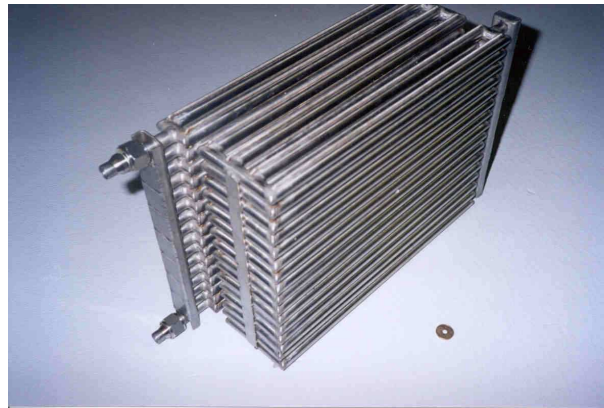
Figure 6.9: Horizontal tube heat exchangers: generator

- Construction of the distributors for the generator, evaporator and absorber: cutting of the stainless steel pieces and welding.

- Selection of commercial elements:

  - 2 plate heat exchangers in series that constitute the solution heat exchanger, model: Alfa-Laval CB14-14 with plates AISI 316.

  - 2 magnetically coupled gear pumps of variable velocity model: Cole-Parmer E-74011-45 (also used in experimental test device of the small absorbers). Characteristics:

    * Stainless steel.
    * 0.32-8.00 l/min of flow.
    * Connection to the process 1/4" NPT.
    * 230 VAC 50/60 Hz.

  - 1 magnetically coupled gear pump model: Isochem model GMC2KCBKLKB (refrigerant pump). Characteristics:

    * Stainless steel.
    * 1-8.3 l/min of flow, variable speed engine.
    * Connection to the process 1/4" NPT.
    * 230 VAC 50 Hz.

  - Stainless steel tubes of 1/2" of outer diameter (also used in experimental test device of the small absorbers).

  - Ball valves for isolating the circuit parts: Hoke rotorball 72. Material: mostly stainless steel (also used in experimental test device of the small absorbers).

  - Precision fittings Hoke Gyrolok 1/2" (also used in experimental test device of the small absorbers).

  - Flexible tubes with connections iso-KF for the vacuum line (also used in experimental test device of the small absorbers).

  - 1 variable speed fan, Sodeca, model HEP-56-4T/H (the same used in experimental test device of the small absorbers).

  - 1 turbomolecular pump, Alcatel model ATP 80 C (the same used in experimental test device of the small absorbers). Characteristics:

    * Vacuum limit $5 \cdot 10^{-9}$ mbar.
    * Volume flow 80 l/s.

  - 1 vacuum pump, Telstar model 2G-9 (same used in experimental test device of the small absorbers). Characteristics:

- * 9 m3/h of volume flow.
- * $8 \cdot 10^{-4}$ mbar of vacuum limit.

  - 1 cold trap, Nor-cal (same used in experimental test device of the small absorbers).

  - 1 line valve (vacuum line), Varian type Cv (same used in experimental test device of the small absorbers). Characteristics:

    - * Conductance 3.4 l/s.
    - * Vacuum range: atmosphere to below 10^{-9} Torr.
    - * Operating temperature: 26-150°C.

  - 2 thermostatic bath Haake model N3, 3000 W of heating capacity (one of them used in experimental test device of the small absorbers).

- • Selection of the measurement instruments: flow meters, pressure transducers and temperature probes.

  - 2 mass flow meters and densimeters model Micro Motion Elite reference CMF025M300NB (also used in experimental test device of the small absorbers). Accuracy: ± 0.15% of reading in the mass flow and 0.0005 g/cm^3 in density with the transmitters Micro Motion Elite reference RFT9739E4EBB (also used in experimental test device of the small absorbers).

  - 1 mass flow meter Micro Motion reference R050SI116M. Accuracy: ± 0.50% of reading with transmitter model Micro Motion IFT9703IC6D3M.

  - 1 mass flow meter Micro Motion reference CMF050M300NM. Accuracy: ± 0.10% of reading with transmitter model Micro Motion reference IFT9701R3N1M.

  - 1 hot wire anemometer Testo, reference 435. Accuracy: ± 0.05 m/s for each instantaneous measurement.

  - 2 absolute pressure sensors, MKS Baratron model 628B (one of them used in experimental test device of the small absorbers). Accuracy: ± 0.25% of reading.

  - 11 temperature probes PT100, Desin Instruments (the same type used in experimental test device of the small absorbers). Calibrated according to the procedure described in the next section, in order to correct possible bias in the readings.

  - 4 thermocouples K, Desin Instruments (the same type used in experimental test device of the small absorbers). Calibrated according to the procedure described in the next section.

6.4   Set-up of the absorption chiller and procedure of operation

Every set-up of the absorption chiller consists on several steps, mainly focused in assuring the maximum sealing of the system in order to prevent air leakages, harmful for a correct performing of the machine. In the following points, the different steps of the set-up are described:

1. Cleaning the parts of the absorption chiller.

2. Drying the cleaned parts with dry nitrogen.

3. Application of vacuum grease of the o-ring joints, without exceeding a specified quantity in order to avoid damage the turbomolecular pump.

4. Checking every part of the machine separately with the help of a mass spectrometer helium leak detector in order to assure the absence of possible air leakages: upper and lower shell, heat exchangers, tubes.

5. Assembly of the components.

6. Re-checking of the whole machine with the mass spectrometer helium leak detector.

7. Calibration of the temperature probes. The calibration has been carried out in a thermostatic bath with refrigeration, in order to achieve a higher stability of the required temperature. A precision Platinum Resistance Thermometer (PTR) has been used as reference value, with its own data acquisition unit. The PTR system accuracy is $\pm 0.025°C$. The accuracy of the calibration system (PTR + thermostatic bath) is $\pm 0.08°C$. On the other hand, the Data Acquisition Switch Unit (DASU) used for the thermocouples has an accuracy of $\pm 0.2°C$. Therefore, the total precision of the measured temperature is less than $\pm 0.3°C$.

8. Verification of the pressure transducers and mass flow meters.

9. Preparation of the LiBr solution.

10. Introduction of the LiBr solution.

11. Purge of the whole system.

The warm-up of the chiller consists of the connection of the different pumps and the fan, in the following order:

1. Warming of the water of the generator circuit with the thermostatic bath.

2. When the hot water reaches the desired temperature (usually 80 °C), connection of the solution pumps.

3. Connection of the hot water pump, in order to warm the internal LiBr solution.

4. When the solution reaches a desired temperature (typically 70°C), connection of the rest devices: refrigerant pump, chilled water pump, fan.

5. Adjust the expansion valve.

References

[1] J. Mikielewicz and J. R. Moszynski. Minimum thickness of a liquid film flowing vertically down a solid surface. *International Journal of Heat and Mass Transfer*, 19(-):771–776, 1976.

[2] J. Tang, B. Yu-chi, and Z. Lu. Minimum wetting rate of film flow on solid surface. In *Proceedings of the XVIIIth International Congress of Refrigeration*, pages 519–523, 1991.

Jesús Castro Gonzàlez, *Simulation of heat and mass transfer phenomena in the critical elements of H_2O-LiBr absorption cooling machines. Experimental validation and application to design.*, Doctoral Thesis, Universitat Politècnica de Catalunya, April 2005.

Chapter 7

Absorption chiller results

Abstract. Several tests have been carried out on the absorption machine under different conditions. The experimental data have been compared with the numerical results obtained from the model of the whole absorption cycle. From the results obtained, the conclusions reported will lead the future revisions of design and improvements to be implemented in order to achieve a better performance and reliability.

The heat exchangers of the prototype have been analysed and the absorption machine has been used as a test bank to validate the results obtained from the models developed. The discrepancies between numerical results and experimental data are under 15% in most cases for all components except the condenser, where the discrepancies are about 30%. The conclusions reported will lead to future revisions of design to achieve a reduction of the heat and mass transfer exchange area of the machine.

7.1 Absorption cycle

The evaluation of the machine has been performed comparing the experimental data with numerical results obtained by means of the whole cycle simulation. The coefficient of performance (COP) of the cycle, defined as in equation (7.1), and the cooling capacity are numerically compared taking into account the overall heat transfer coefficients multiplied by the heat exchanger areas (UA) obtained from the more detailed models developed for the heat exchangers (see Chapter 2). In all the simulated cases dry air has been considered. In order to assure a similar quality of the points measured, before starting each test, the machine is purged until the air concentration measured at the absorber with the mass spectrometer is lower than 2% in volume. The coefficient of performance (COP) of the system is defined as:

$$COP = \frac{\dot{Q}_{ev}}{\dot{Q}_{gn}} \tag{7.1}$$

Figs. 7.1-7.6 show some illustrative results of the behaviour of the machine at the following external working conditions: input hot water temperature, $T_{19} = 85°C$, outlet chilled water temperature $T_{22} = 9°C$, and environmental temperature $T_{15} = 35°C$. Temperature vs. entropy and pressure vs. enthalpy diagrams are also presented. The experimental results (solid lines) are compared with the theoretical ones (dotted lines) obtained from the model described using estimated UAs.

Table 7.1 also shows the comparison between experimental and numerical results for the different points of the cycle. It can be observed that the condensation pressure is higher in the calculations than in real performance. However, the evaporation pressure is lower in the calculation than in the experiment. Moreover, the calculated concentrations are lower than the measured ones.
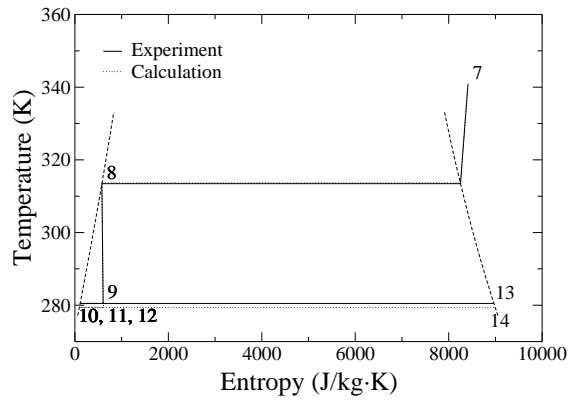
Figure 7.1: T-s diagram for the pure refrigerant (H₂O)
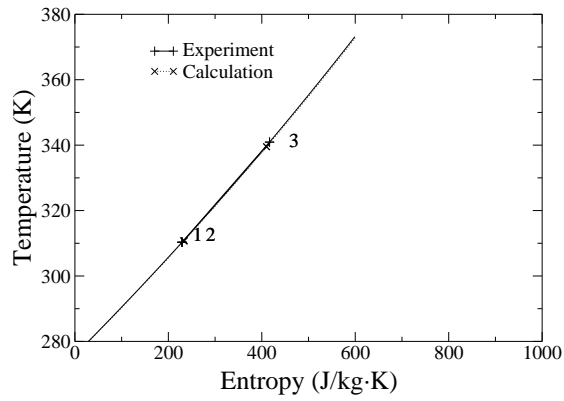
Figure 7.2: T-s diagram for the weak solution (H₂O-LiBr)
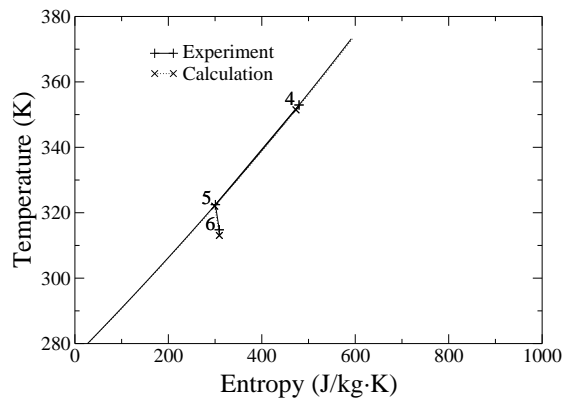
Figure 7.3: T-s diagram for the strong solution (H_2O-LiBr)
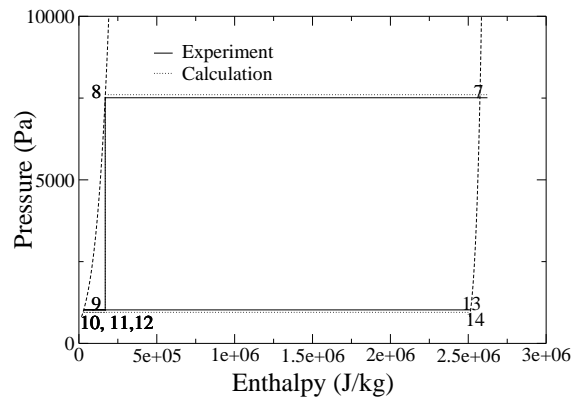
Figure 7.4: p-h diagram for the pure refrigerant (H_2O)
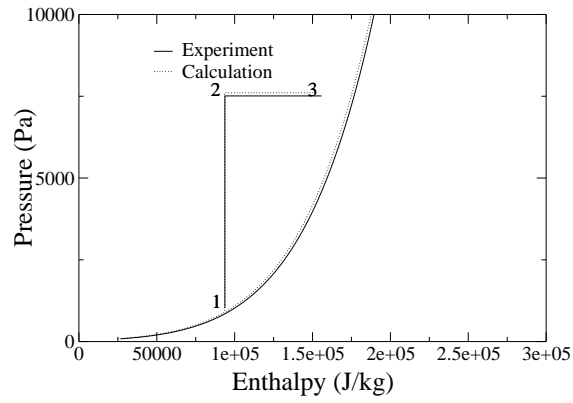
Figure 7.5: p-h diagram for the weak solution (H$_2$O-LiBr)
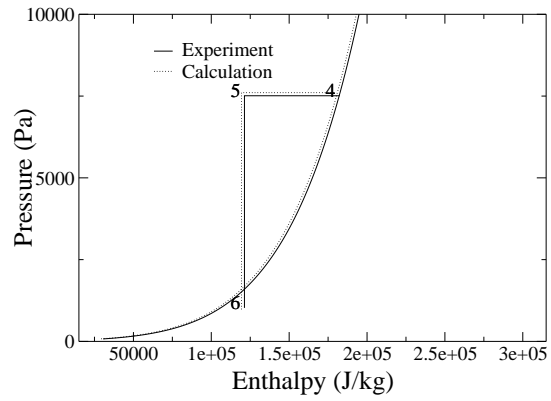
Figure 7.6: p-h diagram for the strong solution (H$_2$O-LiBr)

point	T	p	c	h	s
	(°C)	(Pa)	(LiBr)	(J/kg)	(J/kg·K)
1, exp	37.17	1024	0.56569	$9.376473\cdot10^4$	$2.293372\cdot10^2$
1, num	37.60	948	0.56309	$9.357568\cdot10^4$	$2.334889\cdot10^2$
2, exp	37.17	7510	0.56569	$9.376473\cdot10^4$	$2.293372\cdot10^2$
2, num	37.60	7605	0.56309	$9.357589\cdot10^4$	$2.334872\cdot10^2$
3, exp	67.78	7510	0.56569	$1.557927\cdot10^5$	$4.165840\cdot10^2$
3, num	66.35	7605	0.56309	$1.520524\cdot10^5$	$4.102434\cdot10^2$
4, exp	79.80	7510	0.57307	$1.824592\cdot10^5$	$4.797246\cdot10^2$
4, num	78.29	7605	0.57073	$1.786768\cdot10^5$	$4.732144\cdot10^2$
5, exp	49.32	7510	0.57307	$1.212865\cdot10^5$	$3.006721\cdot10^2$
5, num	48.86	7605	0.57073	$1.194118\cdot10^5$	$2.993345\cdot10^2$
6, exp	41.64	1024	0.57307	$1.212865\cdot10^5$	$3.090238\cdot10^2$
6, num	39.91	948	0.57073	$1.194150\cdot10^5$	$3.091560\cdot10^2$
7, exp	79.80	7510	0	$2.623249\cdot10^6$	$8.413807\cdot10^3$
7, num	78.29	7605	0	$2.620799\cdot10^6$	$8.399851\cdot10^3$
8, exp	40.29	7510	0	$1.688855\cdot10^5$	$5.772455\cdot10^2$
8, num	40.53	7605	0	$1.698739\cdot10^5$	$5.804045\cdot10^2$
9, exp	7.35	1024	0	$1.688855\cdot10^5$	$6.035688\cdot10^2$
9, num	6.23	948	0	$1.698739\cdot10^5$	$6.091114\cdot10^2$
10, exp	7.35	1024	0	$3.086195\cdot10^4$	$1.113884\cdot10^2$
10, num	6.23	948	0	$2.618968\cdot10^4$	$9.482154\cdot10^1$
11, exp	7.35	1024	0	$3.086195\cdot10^4$	$1.113884\cdot10^2$
11, num	6.23	948	0	$2.618968\cdot10^4$	$9.482154\cdot10^1$
12, exp	7.35	1024	0	$3.086195\cdot10^4$	$1.113884\cdot10^2$
12, num	6.23	948	0	$2.618968\cdot10^4$	$9.482154\cdot10^1$
13, exp	7.35	1024	0	$2.515141\cdot10^6$	$9.184149\cdot10^3$
13, num	6.23	948	0	$2.513117\cdot10^6$	$8.996278\cdot10^3$
14, exp	7.35	1024	0	$2.515141\cdot10^6$	$9.184149\cdot10^3$
14, num	6.23	948	0	$2.513117\cdot10^6$	$8.996278\cdot10^3$

Table 7.1: Main experimental data of the cycle compared with the numerical results

The absorption chiller unit has been tested under several external conditions: input hot water temperature, input chilled water temperature, and environment temperature (air-cooling temperature). Table 7.2 shows all measured data of interest for each working condition of the machine. The data showed are: number of test, input hot water temperature, environmental temperature, output chilled water temperature, hot water mass flow, mass flow of air, chilled water mass flow, heat rejected at the absorber, heat introduced at the generator, heat absorbed at the evaporator, heat rejected at the condenser, heat exchanged at the SHX, condensation pressure, evaporation pressure, low LiBr concentration level, high LiBr concentration level, solution flow pumped from the absorber to the generator and finally, COP. It can be observed that the concentrations measured are quite far from crystallisation, even at 95 °C of input hot water temperature. From these results, it can be concluded that these values are room enough to reduce the size of the absorber.

test	T_{19} (°C)	T_{15} (°C)	T_{21} (°C)	$\dot{m}_{19}$ (kg/s)	$\dot{m}_{15}$ (kg/s)	$\dot{m}_{21}$ (kg/s)	$\dot{Q}_{ab}$ (W)	$\dot{Q}_{gn}$ (W)	$\dot{Q}_{ev}$ (W)	$\dot{Q}_{cn}$ (W)	$\dot{Q}_{SHX}$ (W)	P8 (Pa)	P13 (Pa)	$c_{3'}$ (LiBr)	$c_{6'}$ (LiBr)	$\dot{m}_1$ (kg/s)	COP
1	75.0	30.2	8.5	0.13	0.94	0.07	2749	2689	1522	1618	2589	5743	921	0.5480	0.5557	0.046	0.57
2	80.0	30.5	8.6	0.13	0.93	0.07	3503	3464	2127	2265	2790	6082	907	0.5566	0.5675	0.047	0.61
3	85.0	30.1	8.5	0.11	0.93	0.07	3809	3784	2207	2357	2790	6243	858	0.5661	0.5775	0.047	0.58
4	90.0	30.0	8.6	0.09	0.93	0.07	4190	4192	2597	2780	3018	6508	847	0.5707	0.5842	0.048	0.62
5	95.0	30.0	8.5	0.10	0.93	0.07	5191	5220	3361	3607	3385	7165	845	0.5799	0.5972	0.049	0.64
6	80.0	34.9	8.5	0.11	0.93	0.07	2039	1967	827	880	2723	7326	1046	0.5561	0.5603	0.047	0.42
7	85.0	35.2	8.5	0.10	0.92	0.07	2777	2738	1432	1529	2890	7510	1024	0.5657	0.5731	0.047	0.52
8	90.0	35.1	8.6	0.11	0.92	0.07	3329	3296	1829	1960	3134	7699	946	0.5768	0.5863	0.048	0.56
9	95.0	35.2	8.5	0.11	0.92	0.07	4051	4030	2342	2520	3331	8611	973	0.5820	0.5941	0.049	0.58
10	75.0	30.5	11.7	0.12	0.93	0.07	3138	3090	1979	2093	2437	6261	1221	0.5300	0.5399	0.046	0.64
11	80.0	30.2	11.7	0.14	0.93	0.07	3888	3874	2580	2738	2655	6731	1190	0.5408	0.5538	0.046	0.67
12	85.0	30.4	11.7	0.14	0.93	0.07	4556	4572	3094	3291	2854	7321	1206	0.5475	0.5632	0.047	0.68
13	90.0	30.3	11.7	0.14	0.92	0.07	5234	5259	3567	3808	3096	7782	1151	0.5588	0.5769	0.048	0.68
14	95.0	30.5	11.6	0.11	0.92	0.07	5596	5641	3810	4076	3260	8254	1128	0.5667	0.5862	0.049	0.68
15	75.0	35.1	11.7	0.13	0.93	0.07	1631	1537	565	598	2520	7493	1241	0.5379	0.5407	0.045	0.37
16	80.0	35.2	11.7	0.12	0.92	0.07	2365	2288	1135	1209	2763	7820	1210	0.5488	0.5545	0.046	0.59
17	85.0	35.0	11.7	0.12	0.92	0.07	3210	3151	1780	1899	3027	8031	1178	0.5591	0.5682	0.047	0.56
18	90.0	35.2	11.7	0.11	0.92	0.07	3675	3645	2174	2321	3106	8360	1167	0.5621	0.5732	0.048	0.60
19	95.0	35.2	11.6	0.11	0.92	0.07	4469	4455	2743	2941	3389	8762	1136	0.5742	0.5883	0.049	0.62

Table 7.2: Main experimental parameters of the cycle at different working conditions (primary circuits)

Figs. 7.7 and 7.8 show the COP evolution of the machine vs. the input hot water temperature, considering output chilled water temperature of 9°C and 12°C, respectively. Two families of curves are represented, at each Fig., one at an environmental temperature of 30°C, and the other one at 35°C. Each family of curves represent: i) experimental COP obtained from the data measured in the primary circuits, ii) experimental COP obtained from the data measured in the secondary circuits, iii) numerically calculated COP using calculated UAs.

There is an acceptable agreement between the experimental COP and the theoretical one, especially with the primary fluid data, and under conditions far from the minimum driving temperature at the generator. The evolution in the COP indicates an important decrease in the performance of the machine between an environmental temperature of 30°C and 35°C. The maximum value of the COP is about 0.65. For all the tested cases, its measured efficiency has been about 0.7.
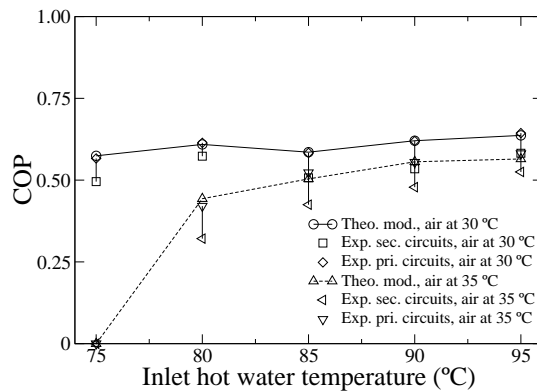
Figure 7.7: Calculated vs. experimental COP for output chilled water at 9°C
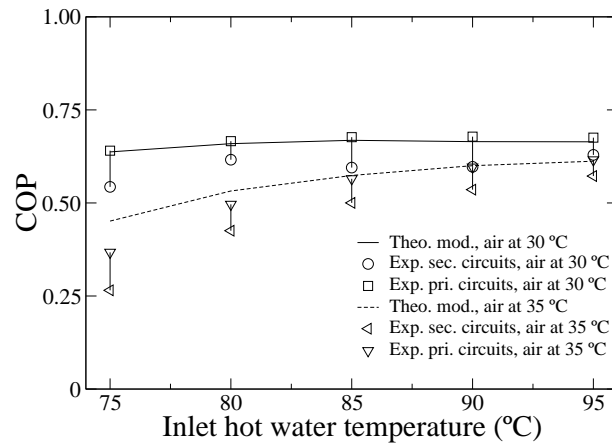
Figure 7.8: Calculated vs. experimental COP for output chilled water at $12°$C

Figs. 7.9 and 7.10 show the evolution of the cooling capacity of the machine. The first one indicates the cooling capacity for an output chilled water temperature of approximately $9°$C, while the second one depicts the cooling capacity for a temperature of approximately $12°$C. There are also two families of curves in each plot, one at an environmental temperature of $30°$C, and the other at $35°$C. Each family of curves describes: i) experimental cooling capacity obtained from the data measured in the primary circuits, ii) experimental cooling capacity obtained from the data measured in the secondary circuits, iii) numerically calculated cooling capacity using calculated UAs.

The calculated cooling capacity is in general lower than the one measured from the primary circuits. This is due to the general underestimation about 10-20% of the UA value by the model developed related to the generator. The Figures show an almost linear dependency between the capacity of the machine and the input hot water temperature. As it was observed in Figs. 7.7 and 7.8, there is an important decrease of the capacity of the machine when the environmental temperature increases from $30°$C to $35°$C (between 1000-1500 W). On the contrary, there is an increase of the capacity at $12°$C of output chilled water (about 500 W). Although this temperature could not be suitable for fan-coil applications, these working conditions can be adequate for chilled ceiling or wall panels.
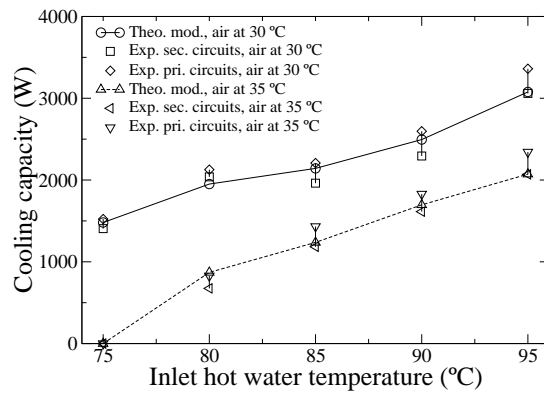
Figure 7.9: Calculated capacity vs. measured for output chilled water at 9°C
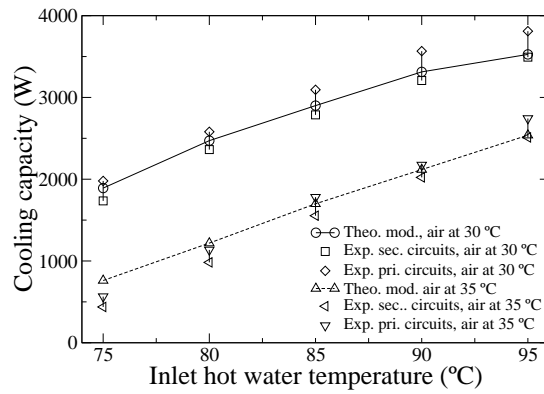
Figure 7.10: Calculated capacity vs. measured for output chilled water at 12°C

7.2   Heat and mass exchange components

The performance of the calculated components with the numerical detailed models (absorber, condenser, generator and evaporator) is evaluated in every experimental point under the input conditions provided by the experimentation. The contact angle data between water and stainless steel has been extracted from [1] (36.3°) and between water-LiBr solution and stainless steel and copper from [2] (13.6° and 13.0°, respectively).

For the case of the absorber (see Fig. 7.11), the agreement in the heat dissipated between numerical and experimental results is very acceptable, with differences under 10% in most cases. The influence of humidity for each case has been indicated. However, as can be seen in Table 7.3 the prediction of the changes in concentration and temperature differences are less accurate than in the case of the heat dissipated. The predicted values are in general higher for the changes in concentration and lower for the changes in temperature with respect to the experimentation.
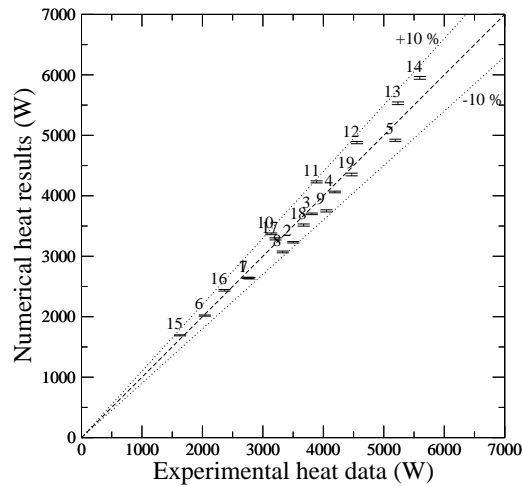
Figure 7.11: Absorber: comparison of the heat exchanged

Fig. 7.12 represents the comparison between the numerical results of the model of the generator and the experimental ones. It can be observed that in most of the cases,

the calculated heat underpredicts the experimental one, although the discrepancies are lower than 20%. Table 7.3 shows the predictions for the change of temperature and change of concentration are less accurate. In general, the predicted values are higher for both changes in concentration and changes in temperature, with respect to the experimentation.
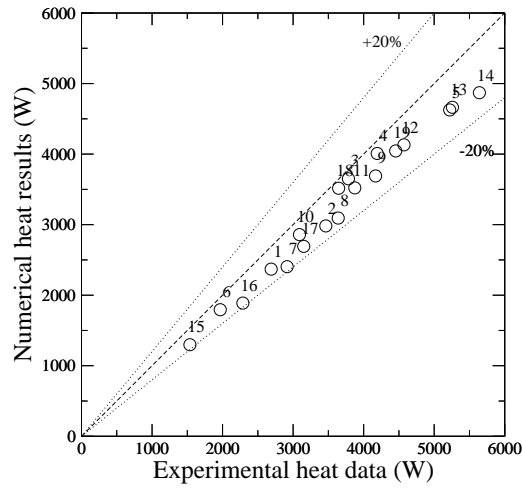
Figure 7.12: Generator: comparison of the heat exchanged

Fig. 7.13 show the comparative of the results for the condenser. Most of the cases are under 30% of difference. In general, it can be said that the numerical model underpredicts the heat dissipated, except in three cases (that correspond to the three results with lowest heat measured), where the discrepancies are important. The air outlet temperature for the absorber has been considered as inlet the temperature of the condenser. An uniform profile has been assumed, that can be one of the main reasons of this general underprediction of the heat dissipated. As in the case of the absorber, it has been indicated the influence of the air humidity.
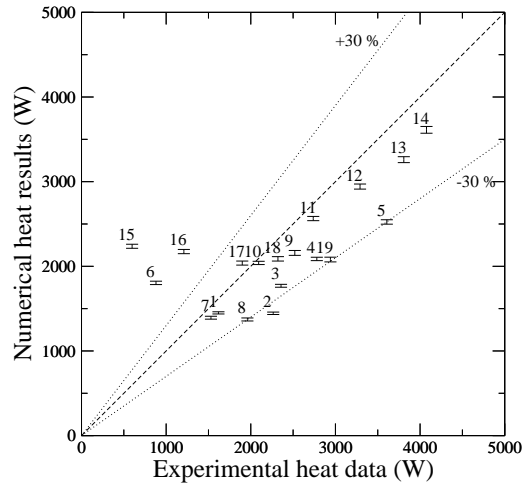
Figure 7.13: Condenser: comparison of the heat exchanged

Finally, in Fig. 7.14 the same comparison is shown between the results of the model of the evaporator and the experimental ones. In all cases, the mass flow of water recirculated has been estimated in 108 kg/h. For this element, in most of the cases the differences between the heat calculated and the one measured are under 15 %, although in general the numerical results overpredict the empirical ones.
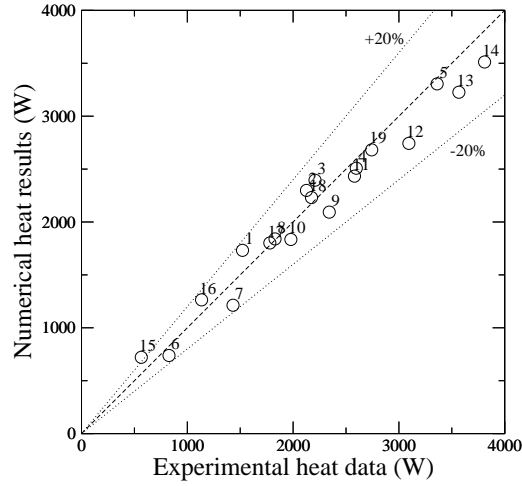
Figure 7.14: Evaporator: comparison of the heat exchanged

7.3 Tables of results

Next Tables show the comparative data between numerical and experimental results. The air stream in the absorber and condenser goes through the absorber first, and after, through the condenser. The inlet air humidity at the absorber is 50%. The experimental values of heat exchanged have been obtained from the primary fluids.

	Solution input cond.				Air input cond.		T_1			c_1			$\dot{Q}$		
test	p	$\dot{m}_{6'}$	$T_{6'}$	$c_{6'}$	$\dot{m}_{15}$	T_{15}	exp.	calc.	%diff.	exp.	calc.	%diff.	exp.	calc.	%diff.
n$^{\text{o}}$	(Pa)	(kg/s)	($^\circ C$)	(LiBr)	(kg/s)	($^\circ C$)	($^\circ C$)	($^\circ C$)	ΔT	(LiBr)	(LiBr)	Δc	(W)	(W)	ΔQ
1	921	0.046	43.20	0.5557	0.94	30.2	32.09	33.94	-16.7	0.5480	0.5475	+ 6.5	2749	2642	- 3.9
2	907	0.047	44.61	0.5675	0.93	30.5	32.84	35.03	-18.6	0.5566	0.5566	+ 0.0	3503	3231	- 7.8
3	858	0.048	47.47	0.5775	0.93	30.1	33.62	35.40	-12.9	0.5661	0.5653	+ 7.0	3809	3702	- 2.8
4	847	0.048	47.04	0.5842	0.93	30.0	33.94	35.81	-14.3	0.5707	0.5699	+ 5.9	4190	4064	- 3.0
5	845	0.049	48.48	0.5972	0.93	30.0	34.59	37.09	-18.0	0.5798	0.5791	+ 4.0	5191	4918	- 5.3
6	1046	0.047	47.86	0.5604	0.93	34.9	36.21	37.73	-13.0	0.5561	0.5552	+20.9	2039	2020	- 0.9
7	1024	0.047	49.32	0.5731	0.92	35.2	37.17	38.93	-14.5	0.5657	0.5652	+ 6.7	2777	2638	- 5.0
8	946	0.048	50.47	0.5863	0.92	35.1	37.47	39.48	-15.5	0.5768	0.5765	+ 3.2	3329	3071	- 7.8
9	973	0.049	52.31	0.5941	0.92	35.2	38.16	40.58	-17.1	0.5820	0.5815	+ 4.1	4051	3750	- 7.4
10	1221	0.046	43.39	0.5399	0.93	30.5	33.47	35.17	-17.1	0.5300	0.5282	+18.2	3138	3371	+ 7.4
11	1190	0.046	45.34	0.5538	0.93	30.2	34.55	36.15	-14.8	0.5408	0.5384	+18.5	3888	4230	+ 8.8
12	1206	0.047	47.06	0.5632	0.93	30.4	35.57	37.32	-15.2	0.5475	0.5450	+15.9	4556	4880	+ 7.1
13	1151	0.048	48.83	0.5769	0.92	30.3	36.31	38.20	-15.1	0.5587	0.5561	+14.3	5234	5530	+ 5.7
14	1128	0.049	50.28	0.5862	0.92	30.5	37.20	39.01	-13.8	0.5667	0.5636	+15.9	5596	5950	+ 6.3
15	1241	0.046	46.26	0.5407	0.93	35.1	35.75	37.47	-16.4	0.5379	0.5367	+42.9	1631	1693	+ 3.8
16	1210	0.046	47.57	0.5545	0.92	35.2	36.13	38.62	-21.8	0.5488	0.5471	+29.8	2365	2437	+ 3.0
17	1178	0.047	48.43	0.5682	0.92	35.0	35.92	39.61	-29.5	0.5591	0.5568	+25.3	3210	3287	+ 2.4
18	1167	0.048	49.75	0.5732	0.92	35.2	37.12	40.12	-23.8	0.5621	0.5610	+ 9.9	3675	3516	- 4.3
19	1136	0.049	50.83	0.5883	0.92	35.2	37.00	41.37	-31.6	0.5742	0.5721	+14.9	4469	4352	- 2.6

Table 7.3: Comparison between experimental and numerical results for the absorber

test	Solution input cond.				Wat. input cond.		T_4			c_4			$\dot{Q}$		
	p	$\dot{m}_{3'}$	$T_{3'}$	$c_{3'}$	$\dot{m}_{19}$	T_{19}	exp.	calc.	%diff.	exp.	calc.	%diff.	exp.	calc.	%diff.
n^O	(Pa)	(kg/s)	($^\circ C$)	(LiBr)	(kg/s)	($^\circ C$)	($^\circ C$)	($^\circ C$)	ΔT	(LiBr)	(LiBr)	Δc	(W)	(W)	ΔQ
1	5743	0.046	59.87	0.5480	0.13	75.00	70.57	72.29	+16.0	0.5557	0.5545	-15.6	2689	2369	-11.9
2	6082	0.047	62.69	0.5566	0.13	80.00	74.31	76.32	+17.2	0.5675	0.5654	-19.3	3464	2982	-13.9
3	6243	0.048	63.22	0.5661	0.11	85.00	77.19	80.04	+20.4	0.5775	0.5765	- 8.7	3784	3650	- 3.5
4	6508	0.048	65.81	0.5707	0.09	90.00	79.44	83.06	+26.5	0.5842	0.5826	-11.9	4192	4009	- 4.4
5	7165	0.049	69.56	0.5798	0.10	95.00	84.57	87.82	+21.7	0.5972	0.5938	-19.5	5220	4626	-11.4
6	7326	0.047	65.37	0.5561	0.11	80.00	76.43	79.99	+32.2	0.5604	0.5597	-16.3	1967	1794	- 8.8
7	7510	0.047	67.68	0.5657	0.10	85.00	79.80	81.65	+15.3	0.5731	0.5716	-20.3	2915	2404	-17.5
8	7699	0.048	70.55	0.5768	0.11	89.99	83.61	85.79	+16.7	0.5863	0.5853	-10.5	3639	3093	-15.0
9	8611	0.049	73.04	0.5820	0.11	95.00	87.52	90.32	+19.3	0.5941	0.5922	-15.7	4169	3690	-11.5
10	6261	0.046	59.36	0.5300	0.12	75.00	69.19	71.47	+23.2	0.5399	0.5387	-12.1	3090	2859	- 7.5
11	6731	0.046	62.51	0.5408	0.14	80.00	73.50	76.02	+22.9	0.5538	0.5520	-13.8	3874	3521	- 9.1
12	7321	0.047	65.18	0.5475	0.14	85.00	77.34	80.11	+22.8	0.5632	0.5607	-15.9	4572	4131	- 9.6
13	7782	0.048	68.20	0.5587	0.14	90.00	81.68	84.61	+21.7	0.5769	0.5736	-18.1	5259	4664	-11.6
14	8254	0.049	70.60	0.5667	0.11	95.00	85.00	88.27	+22.7	0.5862	0.5819	-22.0	5641	4870	-13.7
15	7493	0.046	62.90	0.5379	0.13	75.00	72.55	73.91	+14.9	0.5407	0.5400	-28.5	1537	1304	-15.2
16	7820	0.046	65.63	0.5488	0.12	80.00	76.48	77.93	+13.4	0.5545	0.5529	-28.1	2288	1888	-17.5
17	8031	0.047	67.94	0.5591	0.12	85.00	80.20	82.00	+14.6	0.5682	0.5661	-23.1	3151	2692	-17.1
18	8360	0.048	69.62	0.5621	0.11	90.00	82.40	85.11	+21.2	0.5732	0.5722	- 9.0	3645	3516	- 3.5
19	8762	0.049	72.36	0.5742	0.11	95.00	86.73	89.57	+19.8	0.5883	0.5860	-16.3	4455	4045	- 9.2

Table 7.4: Comparison between experimental and numerical results for the **generator**

point	p	$\dot{m}_{7'}$	$T_{7'}$	$\dot{m}_{17}$	T_{17}	exp.	calc.	%diff.
n^o	(Pa)	(kg/s)	($^\circ C$)	(kg/s)	($^\circ C$)	(W)	(W)	ΔQ
1	5743	$6.4 \cdot 10^{-4}$	35.34	0.94	33.14	1618	1450	-10.3
2	6082	$9.0 \cdot 10^{-4}$	36.38	0.93	34.18	2265	1445	-36.2
3	6243	$9.4 \cdot 10^{-4}$	36.86	0.93	34.16	2357	1770	-24.9
4	6508	$11.0 \cdot 10^{-4}$	37.62	0.93	34.44	2780	2087	-24.9
5	7165	$14.3 \cdot 10^{-4}$	39.41	0.93	35.56	3607	2524	-30.0
6	7326	$3.5 \cdot 10^{-4}$	39.82	0.93	37.07	880	1804	+205.0
7	7510	$6.1 \cdot 10^{-4}$	40.29	0.92	38.16	1529	1393	- 8.9
8	7699	$7.8 \cdot 10^{-4}$	40.76	0.92	38.66	1960	1372	-22.4
9	8611	$10.0 \cdot 10^{-4}$	42.89	0.92	38.92	2520	2158	-30.0
10	6261	$8.4 \cdot 10^{-4}$	36.91	0.93	39.58	2093	2040	- 2.5
11	6731	$10.9 \cdot 10^{-4}$	38.25	0.93	33.80	2738	2564	- 6.3
12	7321	$13.2 \cdot 10^{-4}$	39.81	0.93	34.33	3291	2942	-10.6
13	7782	$15.2 \cdot 10^{-4}$	40.96	0.92	35.31	3808	3260	-14.4
14	8254	$16.3 \cdot 10^{-4}$	42.08	0.92	35.97	4076	3612	-11.4
15	7493	$2.4 \cdot 10^{-4}$	40.25	0.93	36.85	598	2237	+374.1
16	7820	$4.8 \cdot 10^{-4}$	41.05	0.92	37.73	1209	2174	+79.8
17	8031	$7.6 \cdot 10^{-4}$	41.56	0.92	38.44	1899	2038	+ 7.3
18	8360	$9.3 \cdot 10^{-4}$	42.32	0.92	39.12	2321	2088	-10.0
19	8762	$11.7 \cdot 10^{-4}$	43.22	0.92	40.03	2941	2080	-29.3

Table 7.5: Comparison between experimental and numerical results for the **condenser**

Refrigerant input cond.				Air input cond.		$\dot{Q}$		
point	p	$\dot{m}_{11'}$	$T_{11'}$	$\dot{m}_{21}$	T_{21}	exp.	calc.	%diff.
n^o	(Pa)	(kg/s)	($^\circ C$)	(kg/s)	($^\circ C$)	(W)	(W)	ΔQ
1	921	0.030	5.81	0.070	13.27	1522	1732	+13.8
2	907	0.030	5.59	0.070	15.49	2126	2298	+ 8.1
3	858	0.030	4.81	0.070	15.18	2207	2395	+ 8.5
4	847	0.030	4.62	0.070	15.49	2597	2508	- 3.4
5	845	0.030	4.58	0.070	18.86	3361	3305	- 1.7
6	1046	0.030	7.65	0.070	10.80	827	738	-10.8
7	1024	0.030	7.35	0.069	12.53	1432	1213	-15.3
8	946	0.030	6.21	0.070	14.11	1829	1840	+ 0.6
9	973	0.030	6.60	0.070	15.54	2342	2093	-10.6
10	1221	0.030	9.93	0.070	17.57	1979	1835	- 5.3
11	1190	0.030	9.55	0.070	19.65	2580	2433	- 5.8
12	1206	0.030	9.75	0.071	21.12	3094	2743	-11.3
13	1151	0.030	9.06	0.070	22.51	3567	3226	- 9.6
14	1128	0.030	8.76	0.070	23.44	3810	3512	- 7.8
15	1241	0.030	10.17	0.070	13.21	565	721	+27.6
16	1210	0.030	9.80	0.070	15.07	1135	1264	+11.4
17	1178	0.030	9.40	0.070	16.95	1780	1802	+ 1.2
18	1167	0.030	9.26	0.070	18.58	2174	2231	+ 2.6
19	1136	0.030	8.86	0.070	20.09	2743	2682	- 2.2

Table 7.6: Comparison between experimental and numerical results for the **evaporator**

7.4   Conclusions

A laboratory prototype of an air-cooled absorption chiller of H_2O-LiBr has been designed, modelised and tested. From the numerical and experimental results obtained, the following conclusions are highlighted:

- Reasonable agreement has been found between the predicted values and the experimental ones.

- The maximum COP of the machine has been approximately 0.65, with a measured efficiency of the solution heat exchanger approximately 0.7.

- An important decrease of the COP and capacity of the machine between environmental temperature of 30°C to 35°C is observed.

- An important increase of the capacity of the machine between output chilled water temperature 9°C and 12°C is also found.

- Almost linear dependency of the capacity of the machine with the hot water temperature is observed.

- For all cases, the machine is far from crystallization (maximum concentration measured 60% LiBr). The only problem of crystallisation has been originated from inadequate shutdowns of the machine.

- Due to the single effect cycle configuration, the temperature lifts between evaporator and condenser are limited if the hot water temperature is limited to a value of up to 95°C. Consequently, at environmental temperatures higher than 35°C, it is necessary hot water at temperatures higher than 95°C. In this way, evaporation temperatures of approximately 5-6°C can be reached. The only alternative would be an advanced structure of the cycle. However, at higher evaporator temperatures (8-12 °C), other applications different from fan-coils can be applied (chilled ceiling or wall panels). A single effect cycle can be used in these cases.

- Models for an accurate design of the main components (absorber, generator, evaporator, condenser) of an air-cooled absorption machine, with an acceptable agreement. In most cases, the discrepancies in the calculation of the heat disipated are under 15% for all components except the condenser where the accuracy is lower (under 30%). However, the prediction for the absorber and generator of the changes in temperature and concentration in the solution stream are less accurate. One of the reasons could be the difference between the two-dimensional velocity field considered in the falling film calculation, and the real

three-dimensional one of the rivulets produced due to the incomplete wettability of the tube.

- The model implemented for calculating the wetted area of the absorber, generator and evaporator, predicts low values of internal mass flow that does not assure a complete wetted area of the tubes (only about 30-50%). Therefore the heat and mass transfer coefficients decreases drastically. This results are in agreement with the observation of the falling film flow patterns. The only component not affected by this incomplete wetted area is the condenser, because all the area is valid for condensation.

- In order to reduce the final size of the heat and mass exchange components (especially absorber, generator and evaporator, by this order), it will be necessary to improve its wetted area. If no additive is added, special tubes must be used (i.e. microfinned). In such case, new studies about wetted area would be necessary, together with more complex models of calculation of heat and mass transfer as the more detailed one described in chapter 2 for taking into account non-smooth surfaces.

7.5   Nomenclature

A	heat exchange area
c	LiBr mass fraction
$\dot{Q}$	heat power
$\dot{m}$	mass flow
p	pressure
T	temperature
U	overall heat transfer coefficient

Subscripts and superscripts

ab	absorber
air	air (secondary stream)
cl	calculation
cn	condenser
ev	evaporator
ex	experimental
gn	generator
shx	solution heat exchanger
w	water (secondary stream)

References

[1] J. Mikielewicz and J. R. Moszynski. Minimum thickness of a liquid film flowing vertically down a solid surface. *International Journal of Heat and Mass Transfer*, 19(-):771–776, 1976.

[2] K. E. Herold, R. Radermacher, and S. A. Klein. *Absorption Chillers and Heat Pumps*. CRC Press, 1996.

Chapter 8

General conclusions

Abstract. The conclusions of the thesis developed are summarised in this chapter. Several numerical models to study the critical aspects in the design of absorption chillers have been proposed. Special attention has been paid to the most detailed model implemented in order to make a numerical study of vapour absorption processes with and without surfactants. The results produced by the numerical implementation of the other models (complete absorption system, and heat and mass exchange components) have been compared with the experimental results obtained with several prototypes carried out. The first step of prototypes (small air-cooled absorbers) have been tested in order to check absorber modeling. The second group of prototypes, (complete air-cooled absorption chiller) has allowed to compare the whole absorption system model and each one of its components. Finally, the recommended future actions to continue this work are also reported, both from the point of view of improvement of the research developed and further development in absorption technology for the type of machine studied.

Jesús Castro Gonzàlez, Simulation of heat and mass transfer phenomena in the critical elements of H₂O-LiBr absorption cooling machines. Experimental validation and application to design., Doctoral Thesis, Universitat Politècnica de Catalunya, April 2005.

8.1 Conclusions

The main final objective of this work has been the development of numerical simulation tools for the general design of absorption chillers, its improvement and optimization. This general objective has been splitted under different thematic units which has compound each one of the thesis chapters. An important part of the effort in this thesis has been focused on the development of air-cooled absorption machines. This objective can be viewed from two different academic and technological perspectives:

- Academic research. The different models to be used for the design and prediction of absorption chillers have been studied. These models have been numerically implemented. Three levels/stages have been considered: i) absorption processes (with the possibility of evaluating the influence of additives), ii) whole absorption system, and iii) heat and mass exchange components.

- Technological transfer. A particular type of machine with an increasing market: hot water driven, low capacity, air-cooled absorption machine has been identified. Up to now, this type of machine has not been commercialised yet. A first prototype machine with these characteristics has been constructed and tested.

8.1.1 Academic highlights

Special effort has been focused on the application of a model for a detailed simulation of absorption processes with presence of surfactants. As can be seen from the results, the simulated cases are still far for being directly useful for industrial applications, due to hardware CPU time limitations. However, the results obtained are profitable for further research using more complex models (adsorption of surfactants to the interface, 3-D effects, etc.). After many numerical studies and some comparisons with available experimental results [1], the main conclusions to be highlighted are:

- In all simulated cases, there has been observed mass transfer enhancements due to the action of extra surface tension forces. As Daiguji concluded at [1] these results are consistent with the theory of 'salting out', that explains a mechanism of surface tension gradients with surfactant concentrations under the solubility limit. Consequently, the absorption enhancement would be produced only for fluid (liquid and vapour) movements.

- In all simulated situations, 2-ethyl-1-hexanol results in general more efficient than 1-octanol. This fact is coherent with the general impression of the scientific community that 2-ethyl-1-hexanol is a better additive.

- In the case of absorption simulation in a stagnant pool, the numerical results in terms of mass absorbed as function of time, agree better in almost all cases with the empirical results than the ones evaluated computing the liquid phase only, although there are still significant discrepancies. It could be explained by the fact that the simulation carried out is Cartesian 2-D, not cylindrical in three dimensions as the actual situation. Only a direct comparison with a three-dimensional simulation independent of the mesh could assure the total confidence of this model discarding other effects.

- In falling film absorption, the absorption enhancement is more important when the conditions favours the action of surface tension gradients: i) at the beginning of the falling film, where the gradients of temperature and concentration are more important, ii) at low falling film Reynolds numbers, when gravity forces are less important, and iii) and high mass transfer potentials.

The following steps in the work carried out have been focused on the development and validation of numerical simulation tools for the design and development of an absorption machine using the pair H_2O-LiBr. As has been indicated in the previous chapters, this machine must be suitable for solar applications, and it will be used in the domestic sector. Consequently, it will have three main characteristics: i) hot water driven, ii) low capacity, iii) air-cooled. The research has been planned in two stages. In the first step, an experimental device for testing small capacity, air-cooled absorbers has been developed . In the second step, the whole absorption chiller has been constructed and tested. This strategy has been followed in order to have an easier control and better practice, with the absorber test before to the whole absorption chiller. Moreover, the air-cooled absorber as the critical element for this type of machine has been studied.

After testing two small air-cooled absorbers, and the whole absorption chiller, different conclusions must be pointed out:

- A model has been developed for designing the air-cooled absorber, with a reasonably degree of agreement. However, prediction of the changes in temperature and concentration of the solution stream are less accurate.

- The presence of a microfinned surface only produces a minor enhancement of the performance of the absorber.

- For all the tested cases the latent heat of absorption has been more important than the sensible one (about 80-90% of the total).

- The value of the latent heat dissipated in the small-scale absorbers is much better predicted that the value of sensible heat.

- The maximum COP of the machine has been approximately 0.65, with a measured efficiency of the solution heat exchanger approximately 0.7.

- An important decrease of both the COP and capacity of the machine between environmental temperature of 30°C to 35 °C has been observed. Furthermore, an important increase of the capacity of the machine between output chilled water temperature 9°C and 12°C has been obtained.

- An almost linear dependency of the machine cooling capacity with the hot water temperature is observed.

- Models for an accurate design of the main components (absorber, generator, evaporator, condenser) of an air-cooled absorption machine have been developed, with an acceptable agreement. However, as in the case of the absorber, the generator agreement between the prediction of the changes both in temperature and concentration and the experimental results are less accurate.

- The model implemented for calculating the wetted area of the absorber, generator and evaporator, predicts low values of internal mass flow which do not assure a complete wetted area of the tubes (only about 30-50 %). Therefore, the heat and mass transfer coefficients drastically decrease. These results are in agreement with the observation of the falling film flow patterns.

8.1.2 Technological highlights

The main technological objective of this work has been the development of a first prototype of absorption machine with the characteristics already reported (hot water driven, low capacity, air-cooled). This machine has been constructed with a minimum capacity for being useful to the study of different technological aspects, although as small as a laboratory prototype in order to work with advantages.

The different technological solutions for the air-cooled absorber have been tested in the small prototypes. Taking advantage of the experience acquired, other solutions for the rest of elements in the complete absorption chiller have been tested. From the experience gained in the different tests, different conclusions can be reported:

- For all cases, the machine is far from crystallisation (maximum concentration measured 60% LiBr). The only problem of crystallisation has been originated from inadequate shutdowns of the machine.

- Due to the single effect cycle configuration, the temperature lifts between evaporator and condenser are limited if the hot water temperature is limited to a value of up to 95°C. Consequently, at environmental temperatures higher than 35°C, it is necessary to use hot water temperatures higher than 95°C. Thus,

evaporation temperatures of approximately 5-6°C can be reached. However, at higher evaporator temperatures (8-12°C), other applications different from fan-coils can be applied (chilled ceiling or wall panels). Single effect cycle can be used in these cases.

- In order to reduce the final size of the heat and mass exchange components (especially absorber, generator and evaporator, by this order), it will be necessary to improve its wetted area. If no additive is added, special tubes must be used (i.e. microfinned). In such case, new studies about wetted area would be necessary, together with more complex models of calculation of heat and mass transfer as the more detailed one described in Chapter 2 to take into account non-smooth surfaces.

8.2 Future actions

8.2.1 Academic aspects

Although the models used have given quite acceptable agreement with the experimental data, many different aspects must be considered to improve the different modelings:

- Concerning with the detailed simulation of absorption processes for the model used, it is necessary to completely know the values of surface tension gradients respect to temperature and LiBr concentration for each mean concentration of each surfactant. At the present, this knowledge is very limited. To overcome these problems, a more detailed model would be necessary to take into account the adsorption process of the surfactant from the liquid [2] and vapour phases [3] towards the interface and thus, computing the surface tension at each point. This is the main reason because the results reported have to be considered as a preliminary approach.

- In the simulation of absorption systems, it will be necessary in the future to modify the existent software to facilitate the interaction with the more detailed simulation of the heat and mass exchange components.

- Consideration of the three-dimensional velocity field in the falling rivulets of liquid in the simulation of absorption / desorption processes [4, 5] will be important to improve the accuracy of results, especially respect to temperature and concentration changes. This improvement will affect in the simulation of the absorber and the generator, in the case that no complete wetted area is achieved.

- An implementation of a wave modeling in the liquid falling films will be needed in order to improve the results at high Reynolds numbers. This improvement will both affect the modeling of the absorber and the generator.

- The consideration of advanced structure cycles to achieve higher temperature lifts [**?**] and the development more efficient cycles (from an energetic point of view) will make the use of absorption machine under more extreme working conditions possible.

- Development of a model for design / prediction of thermal driven pumps and an experimental testing devices. This element will avoid the mechanical solution pump.

8.2.2   Technological aspects

A first prototype of absorption cooling machine has been developed. One of main premises of this prototype has been the possibility of removing its components in case of deficient performing. However, this clear advantage implies the existence of a large amount of joints that implied the possibility of air leakages in many points of the machine. This has made the set-up and maintenance of the machine quite expensive in terms of time and effort. After the experience of the research carried out, the following aspects will be considered:

- Development of a second prototype taking advantage of the first one: drastic decrease of the number of joints, design closer to the final commercial one.

- Modification of the design of the distribution systems in order to decrease manufacturing costs.

- Thermal driven pump: study of the changes in the design configuration of the rest of the elements. Study of the behaviour of the machine [6, 7, 8].

- Study of the implementation of pool boiling evaporators, in order to avoid the refrigerant pump in more developed prototypes.

References

[1] H. Daiguji, E. Hihara, and T. Saito. Mechanism of absorption enhancement by surfactant. *International Journal of Heat and Mass Transfer*, 40(8):1743–1752, 1997.

[2] M. S. Koenig, G. Grossman, and K. Gommed. The Role of Surfactant Adsorption Rate in Heat and Mass Transfer Enhancement in Absorption Heat Pumps. *International Journal of Refrigeration*, 26(1):129–139, 2003.

[3] S. Kulankara and K. E. Herold. Surface Tension of Aqueous Lithium Bromide with Heat/Mass Transfer Enhancement Additives: the Effect of Additive Vapor Transport. *International Journal of Refrigeration*, 25(3):383–389, 2002.

[4] M. S. Genk and H. H. Saber. Minimum thickness of a flowing down liquid film on a vertical surface. *International Journal of Heat and Mass Transfer*, 44(15):2809–2825, 2001.

[5] M. S. Genk and H. H. Saber. An Investigation of the Breakup of an Evaporating Liquid Film, Falling Down a Vertical, Uniformly Heated Wall. *Journal of Heat Transfer*, 124(1):39–49, 2002.

[6] Yazaki Ltd. *Manual de instalación de grupos refrigerantes por absorción de agua caliente WFC 10*, 1996.

[7] M. Pfaff, R. Saravanan, M. Prakash Maiya, and S. Srinivasa Murthy. Studies of bubble pump for a water-lithium bromide vapour absorption refrigerator. *International Journal of Refrigeration*, 21(6):452–462, 1998.

[8] R. Saravanan and M. Prakash Maiya. Experimental Analysis of a Bubble Pump Operated H_2O-LiBr Vapour Absorption Cooler. *Applied Thermal Engineering*, 23(18):2383–2397, 2003.